Iowa State University
Digital Repository

2015

Accelerating materials discovery and design: computational study of the structure and properties of materials

Xin Zhao
Iowa State University

Follow this and additional works at: http://lib.dr.iastate.edu/etd

Part of the Condensed Matter Physics Commons

Accelerating materials discovery and design: Computational study of the structure and properties of materials

by

Xin Zhao

A dissertation submitted to the graduate faculty

in partial fulfillment of the requirements for the degree of

DOCTOR OF PHILOSOPHY

Major: Condensed Matter Physics

Program of Study Committee:
Kai-Ming Ho, Major Professor
James Evans
Michael Tringides
Kerry Whisnant
Matthew Kramer

Iowa State University

Ames, Iowa

2015

DEDICATION

I would like to dedicate this thesis to my parents, whose support sustained me throughout my graduate studies.

TABLE OF CONTENTS

LIST OF TABLES

LIST OF FIGURES

ACKNOWLEDGMENTS

ABSTRACT

This thesis summarizes our efforts to study the structure and properties of materials computationally. The adaptive genetic algorithm (AGA) developed by us to predict crystal/surface/interface structures is presented. Applications of AGA to a variety of systems, such as non-rare earth magnetic materials, ultra-hard transition metal borides and $SrTiO_3$ grain boundaries, are discussed. We demonstrated by AGA the capability of solving crystal structures with more than 100 atoms per unit cell and rapidly accessing the structures and phase stabilities of different compositions in multicomponent systems. We also introduced a motif-network scheme to study the complex crystal structures in silicate cathodes. In addition, we explored different computational methods for atomistic simulations of materials behavior, such as Monte Carlo modeling of the alnico magnets.

CHAPTER 1.   INTRODUCTION

It is a fascinating idea to achieve materials discovery and design in computer.

The history of technology, similar in many ways to other sides of the history of humanity, is often defined by the material of choice of a given era. The invention of new materials and tools, from the usage of stone, bronze and iron in prehistoric technologies, to semiconductors, nanomaterials and biomaterials in modern world, has been continuously re-shaping the world and greatly improving our lives.

It is worth noting that the time period for the invention and application of a new material becomes shorter and shorter thanks to the accumulation of knowledge and understanding of nature. However, rapid increase of the energy consumption due to booming population and rising standards of living, as well as growing concerns about global warming and air quality start to accelerate the global search for alternative energy sources and more efficient utilization of energy. Thus, the pressure on the development of new materials is becoming formidable.

At present, most useful materials are still discovered by trial and error, guided by the researchers' knowledge, experience, and educated guesses [NSF overview]. Such an old-fashioned way is bound by high costs and time-consuming procedures of synthesis, whereas computational materials discovery and design point out an alternative yet compatible way to confront the emergent energy issues.

Central to the materials design approach is the logical structure connecting the four principle elements [Olson, 1997]: processing, structure, properties and performance, as illustrated in Fig. 1.1. These elements are strongly related and changes in one are inseparably linked to changes in the others. With the development of modern computers and advanced

algorithms over the last several decades, modeling and simulation have been playing more and more significant roles in all aspects.
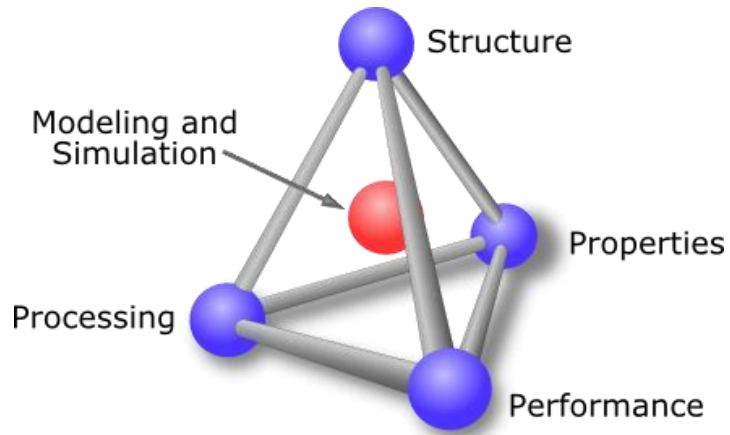
Figure 1.1   The materials paradigm represented in the form of a tetrahedron.

The basis of above materials paradigm involves studying the structure of materials, and relating them to their properties. With the knowledge of this structure-property correlation, the performance of materials in a certain application can then be studied. Therefore, in order to achieve discovery and design of new materials in computer, we must have the capability of accurately predicting the structure of materials and calculating their properties.

We first note that there have been considerable efforts devoted and remarkable accomplishment achieved on the subject of computational materials discovery and design [Sato and Katayamo-Yoshida, 2002; Hafner *et al.*, 2006; Woodley and Catlow, 2008; Meng and Dompablo, 2009; Norskov *et al.*, 2009; Curtarolo *et al.*, 2013]. This thesis summarizes our efforts to develop advanced geometry optimization algorithms and apply them to solve emergent problems. It is organized as following: First, some background is provided in the rest of Chapter 1. Chapter 2 introduces the adaptive genetic algorithm developed by us [Wu *et al.*, 2014] to predict atomic structures. Chapter 3 focuses on the applications of our method to the study of

non-rare earth magnets, including the Co_xZr polymorphs [Zhao *et al.*, 2014a] and boron-doped Co_xZr alloys [Zhao *et al.*, 2015a]. Meanwhile, the lattice Monte Carlo simulation of the alnico magnet [Nguyen *et al.*, 2015] is also discussed in Chapter 3. In Chapter 4, predictions of new stable Re-B phases for ultra-hard materials are presented in the form of the published paper [Zhao *et al.*, 2014c]. In Chapter 5, extension of the adaptive genetic algorithm to predict interface structure is discussed [Zhao *et al.*, 2014b]. Chapter 6 introduces a motif-network scheme for fast explorations of the family of A_2MSiO_4 silicates with A = Li, Na; M = Mn, Fe, Co as cathode materials in Li/Na-ion batteries [Zhao *et al.*, 2015b]. Finally in Chapter 7, I briefly discuss the ongoing work on Gutzwiller density functional theory for studying strongly correlated electron systems and conclude the thesis.

1.1   Structure of materials

Structure of materials ranges from the atomic scale all the way to the macro scale. People have found that different scales of materials structure lead to very interesting and unique properties. For instance, nanomaterials, with a size of usually 1-100 nm, have been one of most intense subjects of research due to the fascinating properties that they exhibit. Here in this thesis, the atomic structure, with a length scale of angstroms, will be the subject of discussion. Many of the electrical, magnetic and chemical properties of materials arise from their atomic structures.

Based on the ordering of atomic structure, materials can generally be divided into two classes: crystalline and non-crystalline, as illustrated in Fig. 1.2. In crystalline solid, atoms are arranged in a highly ordered microscopic structure, while non-crystalline sold, or amorphous solid, lacks the long-range order characteristic of a crystal. Although people have been able to detect and track the existence of short-range and medium-range orders in amorphous solids

[Sheng *et al.*, 2006], it makes no sense to assign a specific atomic structure to any of them. Therefore, the discussion will be focused on the structure of crystals.
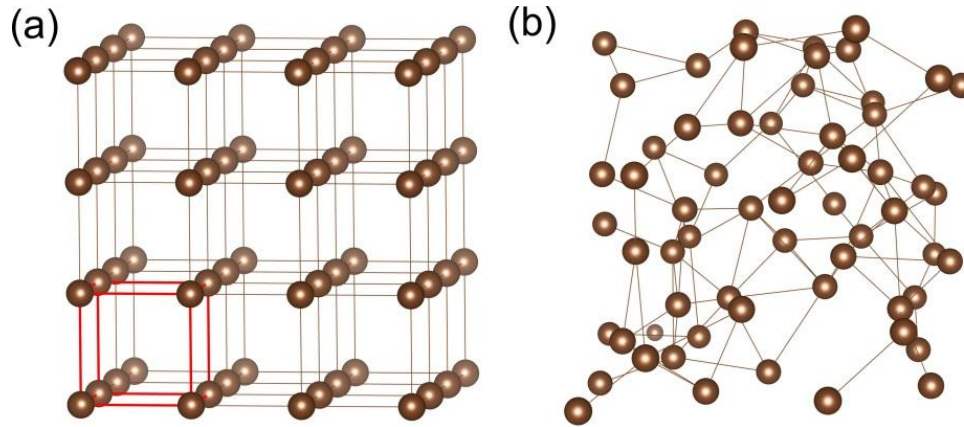
Figure 1.2   Crystalline (a) vs. non-crystalline (b) solids. The red box in (a) represents the unit cell of the structure.

A crystal structure is a unique arrangement of atoms, ions or molecules in a crystalline solid. Crystals possess long-range order, i.e. the arrangement of the atoms at one point in a crystal is identical to that in any other remote part. The subject of crystallography, especially with the modern development on symmetry and mathematical description, has become a standard topic in solid state physics textbooks, where systematic introduction to the structure of crystals can be found [Ashcroft and Mermin, 1976; Kittel, 2005; Tilley, 2006]. Here, only the following most relevant concepts are explained.

Symmetry: describes the periodic repetition of structural features. There are two general types of symmetry, translational symmetry and point symmetry. Translational symmetry describes the periodic repetition of a motif across a length or through an area or volume. Point symmetry describes the periodic repetition of a motif around a point, including reflection, rotation, inversion and rotoinversion.

Lattice: is an array of points repeating periodically throughout space. It is directly related to the idea of translational symmetry.

Unit Cell: is the smallest unit which can be repeated in order to construct the lattice, as illustrated by the red box in Fig. 1.2(a).

Bravais lattices: are the fourteen different lattice structures that are possible in three-dimensional space, named after the French crystallographer Auguste Bravais.

Crystal systems: The point symmetry operations may be combined in different ways. There are 32 possible unique combinations, corresponding to 32 **crystal classes** (or **point groups**). Each crystal class is grouped as one of the six different crystal systems according to which characteristic symmetry operation it possesses. There systems include: Triclinic, Monoclinic, Orthorhombic, Tetragonal, Hexagonal and Cubic. The hexagonal crystal system is further broken down into hexagonal and rhombohedral divisions.

Space group: In addition to the operations of the point group, the space group of the crystal structure contains translational symmetry operations, including pure translations, screw axes and glide planes. There are total 230 distinct space groups.

Above concepts are to describe ideal crystals. All real crystalline solids have finite size and often feature defects and impurities. The resulted surfaces and interfaces in some cases induce new properties in the materials, which will be discussed in greater detail in Chapter 5. Defects also critically determine many of the electrical and mechanical properties of real materials, but will not be the main topic in this thesis.

In experiments, the study of the crystal structures used to rely for a long time on optical techniques, especially optical microscopy, which cannot provide the absolute arrangement of the atoms in a crystal. This limitation was overcome by the development of X-ray diffraction in

1910s [Ewald, 1962]. Nowadays, the determination of the crystal structures mainly bases on analysis of the diffraction patterns of a sample targeted by a beam of some type, such as X-ray, neutrons or electrons, corresponding to techniques as X-ray diffraction, neutron diffraction and electron diffraction.

1.2   Crystal structure predictions

Crystal structure prediction starting from the chemical composition alone has been one of the long standing challenges in theoretical solid state physics, chemistry and materials science [Maddox, 1988; Woodley, 2008]. The major determinants of the structure of a material are its constituent chemical elements and the way in which it has been processed into its final form, governed by the laws of quantum mechanics, thermodynamics and kinetics. Under equilibrium, the lower energy state is usually favored by nature, which makes the task of crystal structure prediction a search for minimum energy arrangement of atoms in the material. Therefore, two necessary pieces of solving the puzzle are an accurate method to calculate the energy and an efficient minimization algorithm.

In the viewpoint of quantum mechanics, energy of a structure, as well as its electronic structure, is obtained by solving the Schrodinger equation. However, the Schrodinger equation for the complex many-atom, many-electron system is not analytically solvable. A breakthrough that makes computational materials discovery and design possible was realized in 1964 when Walter Kohn and co-workers developed the density functional theory (DFT) [Hohenberg and Kohn, 1964; Kohn and Sham, 1965]. DFT, along with various well-developed empirical potential models, have provided us the first piece to solve the puzzle, i.e. tools to calculate energies.

In the past two decades, several computational algorithms have been applied to predict crystal structures, such as simulated annealing [Kirkpatrick *et al.*, 1983; Doll *et al.*, 2007], genetic algorithm (GA) [Deaven and Ho, 1995; Harris *et al.*, 1998; Woodley *et al.*, 1999; Oganov and Glass, 2008; Wu *et al.*, 2014], topological modelling method [Freidrichs *et al.*, 1999; Treacy *et al.*, 2004; Deem and Newsam, 1989], minima hopping [Goedecker, 2004], particle swarm optimization [Wang *et al.*, 2010], and *ab initio* random structure search [Pickard and Needs, 2011]. Each method has been successfully used to solve crystal structures and predict the formation of possible new compounds. In the following (1.2.4), genetic algorithm will be briefly introduced as an example of those structure prediction methods/tools, as it is also the base of our method discussed in Chapter 2.

1.2.1 Energy of a structure

In a broad sense, the energy of a structure refers to the Gibbs free energy G:

$$G = E + PV - TS \tag{1.1}$$

where E is the internal energy, P is pressure, V is volume, T is temperature and S is entropy. The calculation of the internal energy is discussed in the following two sections. Among all three terms, the calculation of PV is rather straight forward, while the calculation of TS by first principles has been a long standing issue and remains controversial [van de Walle and Ceder, 2002b; Prodan, 2010]. In this thesis, temperature effect was not considered unless noted otherwise.

1.2.2 Density functional theory

In a solid state system, a stationary electronic state of an N-electron system is described by wavefunction Ψ satisfying the many-electron time-independent Schrodinger equation:

$$\hat{H}\Psi = E\Psi \tag{1.2}$$

$$\hat{H} = \hat{T} + \hat{V} + \hat{U} = \sum_{i}^{N}\left(-\frac{\hbar^2}{2m_i}\nabla_i^2\right) + \sum_{i}^{N}V(r_i) + \sum_{i<j}^{N}U(r_i, r_j) \tag{1.3}$$

where

$$V(\boldsymbol{r_i}) = \sum_{l}\left(-\frac{e^2}{4\pi\epsilon_0}\frac{Z_l}{|\boldsymbol{r_i} - \boldsymbol{R_l}|}\right) \text{ and } U(r_i, r_j) = \frac{e^2}{4\pi\epsilon_0}\frac{1}{|\boldsymbol{r_i} - \boldsymbol{r_j}|}$$

Born-Oppenheimer approximation has been adopted to separate the degrees of freedom of fast electrons from slow ions. The first term $\hat{T}$ describes the kinetic energy of electrons. The second term $\hat{V}$ describes electron-ion Coulomb attraction where $\boldsymbol{R_l}$ represents the position of nuclei and $\boldsymbol{r_i}$ represents the position of electrons. The third term $\hat{U}$ describes electron-electron Coulomb repulsion.

As mentioned above, this many-body Schrodinger equation is not analytically solvable. There are many sophisticated methods to numerically solve it based on the expansion of the wavefunction in Slater determinants, e.g. Hartree-Fock method and post-Hartree-Fock methods. However, the huge computational effort makes it impossible to apply them to complex systems. DFT, on the other hand, provides a way to map the many-body problem onto a single-body problem. With this theory, the properties of a many-electron system are determined by using functionals, i.e. function of another function, which in this case is the electron density.

DFT is made possible by the existence of Hohenberg-Kohn (H-K) theorems [Hohenberg and Kohn, 1964], which state that:

1. The ground state density uniquely determines the potential and thus all properties of the system, including many-body wavefunction.

2. There exists an energy functional $E[n]$, and the correct ground state electron density minimizes it. The minimal value of $E[n]$ is then the ground state energy.

The proof of the H-K theorems is rather simple and can be found in many related materials [Hohenberg and Kohn, 1964; Martin, 2004]. The H-F theorems lay the groundwork for reducing the many-body problem of N electrons with $3N$ spatial coordinates to 3. In 1965, one year after the publish of H-K theorems, Kohn and Sham made another major step forward towards quantitative modeling of electronic structure, by introducing the Kohn-Sham equation (Eq. 1.4). The Kohn-Sham equation describes a fictitious system of non-interacting electrons that generate the same density as any given system of interacting electrons. As the electrons in the Kohn-Sham system are non-interacting, the Kohn-Sham wavefunction is a single Slater determinant constructed from a set of orbitals that are the lowest energy solutions to the Kohn-Sham equation.

$$\left(-\frac{\hbar^2}{2m}\nabla^2 + v_{eff}(\boldsymbol{r})\right)\phi_i(\boldsymbol{r}) = \varepsilon_i\phi_i(\boldsymbol{r}) \tag{1.4}$$

where the local effective external potential acting on the system is

$$v_{eff}(\boldsymbol{r}) = v_{ext}(\boldsymbol{r}) + e^2 \int \frac{n(\boldsymbol{r'})}{|\boldsymbol{r}-\boldsymbol{r'}|}d\boldsymbol{r'} + \frac{\delta E_{xc}[n]}{\delta n(\boldsymbol{r})}, \text{ and } n(r) = \sum_i |\phi_i(\boldsymbol{r})|^2$$

The Kohn-Sham equation can be solved self-consistently and the results are expected to be exact providing the exact functional form of the exchange-correlation term: $E_{xc}[n]$. Unfortunately, this term is not known exactly. Remarkably, it is possible to make simple approximations and produce extremely good results. Great effort has been made to developing different levels of approximations, such as local density approximation (LDA), generalized

gradient approximation (GGA), Meta-GGA, Hybrid functional, etc., which nowadays are referred to as the "Jacob's ladder of DFT" [Hafner, 2006].

DFT is now among the most popular methods available in condensed matter physics and has been successfully applied to many solid state systems in the last several decades [Perdew *et al.*, 1996; Chelikowsky and Louie, 1996; Kresse *et al.*, 1996, 1999]. It can accurately describe the ground state properties in many solid systems, such as their lattice parameters and formation energies, thus offering us a powerful tool to carry out the energy evaluations.

It is worth mentioning that there are still difficulties in using DFT to properly describe and explain some issues, such as intermolecular interactions, charge transfer excitations, and miscalculation of the band gap in semiconductors. In particular, the predictive capability of DFT becomes limited while dealing with systems with strong electron correlation effects, which will be further discussed in Chapter 7.

1.2.3 Empirical potentials

While DFT calculations usually offer accurate description of the total energies (at $T = 0$ K), its computational cost imposes the bottleneck to the structure prediction of complex materials with unit cells containing ~10^2 atoms for two reasons. First, the energy evaluation for the larger system simply cost more time. Second, the configuration space increases exponentially with the number of atoms in the unit cell, thus many more structures are to be sampled for larger systems. Empirical potentials, on the other hand, provide an alternative way to perform fast energy evaluations for very large systems.

Empirical potentials, or classical potentials, approximate the energy by summing over all interactions between atoms, such as chemical bonds, van der Waals and electrostatic interactions. They contain free parameters like equilibrium bond length, angle, or atomic charges, which can

be obtained by fitting against experimental physical properties or detailed first principles electronic calculations.

Various empirical potentials can be considered as either pair potentials or many-body potentials. For pair potentials, the total potential energy is calculated from the sum of energy contributions between pairs of atoms, while many-body potentials include the effects of three or more particles interacting with each other. To give one example of the pair potential, Eq. 1.5 describes the Lennard-Jones potential used for calculating van der Waals forces [Lennard-Jones, 1924].

$$U(r) = 4\epsilon \left[\left(\frac{\sigma}{r} \right)^{12} - \left(\frac{\sigma}{r} \right)^{6} \right] \tag{1.5}$$

As for the many-body potentials, embedded atom model (EAM) [Daw and Baskes, 1984] is a typical example and widely used for metallic systems. In the studies presented in the later chapters of this thesis, EAM potentials were also selected as our auxiliary potentials. Under the EAM formalism, the potential energy of an atom is given by:

$$E_i = F_\alpha \left(\sum_{i \neq j} \rho_\beta(r_{ij}) \right) + \frac{1}{2} \sum_{i \neq j} \phi_{\alpha\beta}(r_{ij}) \tag{1.6}$$

where r_{ij} is the distance between atom i and j; $\phi_{\alpha\beta}$ is a pairwise potential function; ρ_β is the contribution to the electron charge density from atom j of type β at the location of atom i; F is an embedding function that represents the energy required to place atom i of type α into the electron cloud.

Because of the enormous gaining in speed, people have devoted substantial effort to develop and fit empirical potentials, especially for the purpose of molecular dynamics simulations. Nonetheless, reliable empirical potentials are not always available for many systems

due to the simplicity of the potential model and the transferability of the empirical potentials is also constantly questioned.

1.2.4 Genetic algorithm

Genetic algorithm (GA), belonging to the larger class of evolutionary algorithms (EA), generates solutions to optimization problems using techniques inspired by natural evolution, such as inheritance, mutation, selection, and crossover. It was first introduced to optimize atomic structures by Deaven and Ho, where the fullerene cluster structures up to C_{60} were efficiently found starting from random atomic coordinates [Deaven and Ho, 1995].

Genetic algorithm has many variations, for example in how the crossover and mutation routines are actually defined. With years of development, GA has been applied to various problems, such as clusters [Ho *et al.*, 1998], bulk crystals [Oganov *et al.*, 2009], interfaces and grain boundaries [Zhang *et al.*, 2009; Chua *et al.*, 2010; Zhao *et al.*, 2014b], etc. Here some of the most relevant concepts are explained. Further information and reading can refer to Ref. [Ji *et al.*, 2010; Oganov, 2011].

Population: a group of candidate solutions to an optimization problem which is evolved toward better solutions. Analog to organism in the natural selection, the population here consists of candidate configurations or structures. The initial population is usually randomly generated. It may also be seeded in areas where optimal solutions are likely to be found, e.g. initializing the structures with certain space group or fixed unit cell when possessing such input from experimental measurements.

Selection: Parent structures are selected from the population through a fitness-based process to generate offspring. Usually, structures with lower energy (better fitness score) have larger probability to be selected.

Crossover: genetic operator which is used to generate offspring structures. One of the most popular choices nowadays for crossover operation is still based on real-space atom coordinates as introduced in the Ref. [Deaven and Ho, 1995].

Mutation: genetic operator which is used to preserve and introduce diversity to the population. Classic example is single point mutation, e.g. switch two arbitrary atoms.

CHAPTER 2.   ADAPTIVE GENETIC ALGORITHM FOR GEOMETRY OPTIMIZATION

2.1   Overview

As discussed in Chapter 1, crystal structure prediction is one of the key components in the discovery and design of new materials and has been one of the long-standing challenges in physical sciences. The adaptive genetic algorithm (AGA) was introduced to combine the speed of structure exploration by classical potentials with the accuracy of density functional theory calculations in an adaptive and iterative way.

In this scheme, auxiliary classical potentials are used to explore the structures. Parameters of the auxiliary potentials are adaptively adjusted to reproduce first-principles results during the course of the GA search, which at the same time assists the system in hopping from one basin to another in the energy landscape, leading to efficient sampling of the configuration space. While retaining the accuracy of DFT, AGA is much faster than full DFT GA and offers a useful tool to study the structures of complex materials containing large number of atoms.

2.2   Methods

The flowchart of the AGA scheme is illustrated in Fig. 2.1 [Wu *et al.*, 2014; Zhao *et al.*, 2014b]. The traditional GA loop, i.e., left-hand side of the flowchart, is embedded in an adaptive loop. Inheritance, mutation, selection, and crossover operations are implemented as usual to produce new structures, except that the optimization of the offspring structures in the GA loop is performed using auxiliary classical potentials. Parameters of the classical potentials are adjusted to reproduce DFT results in the adaptive loop. Newly obtained classical potentials are then

passed to next iteration of the AGA search. When the preset maximum number of iterations i_{max} is reached, all the structures calculated by DFT from every iteration are collected and ranked according to their energies. Finally, a set of low-energy structures selected from the DFT pool are fully relaxed by DFT calculations to locate the ground-state structures.
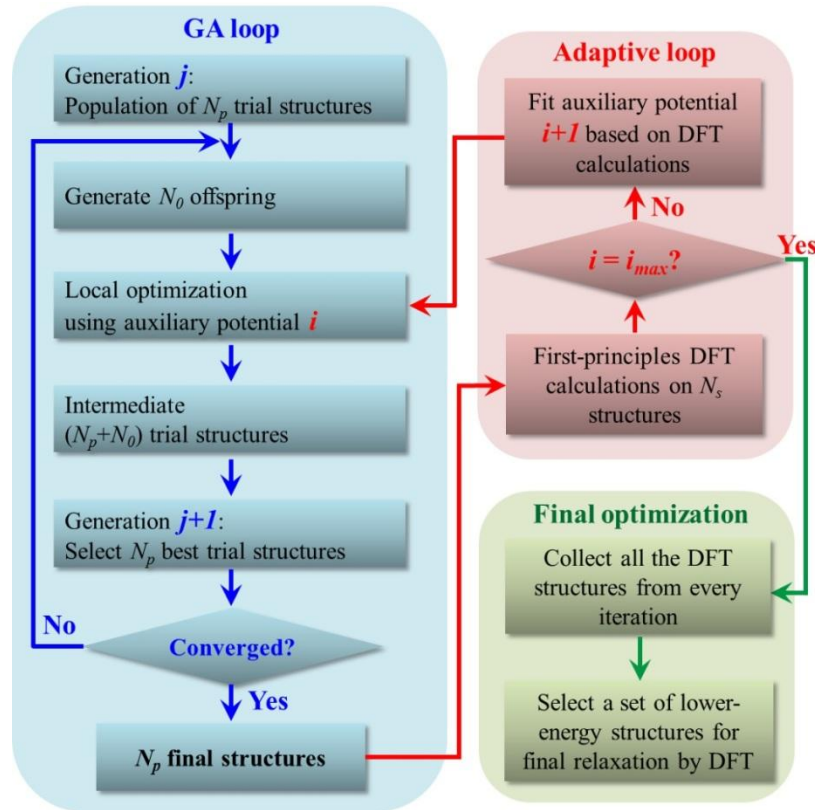
Figure 2.1 Flowchart of the adaptive genetic algorithm. An adaptive loop (with i as the iteration counter) is added to the regular GA-loop (with j as the generation counter).

In the traditional GA, the most time-consuming step is the local optimization of the offspring structures by DFT calculations. In the AGA scheme, DFT calculations are only performed on a small set of candidate structures ($16 \leq N_s \leq 32$) to gain information of their energies, forces, and stresses, which are later used to update the parameters of the auxiliary classical potentials. For such DFT calculations in the adaptive loop, in principle, both the local

optimization and the static calculations can be adopted. Based on the test of different cases, we found that the use of the static DFT calculations is good enough to get accurate results out of AGA searches.

The numbers of total population, N_p, and the number of the offspring structures to be updated, N_o, depend on the complexity of the system being investigated. For a typical binary system with around 30 atoms, we usually take $96 \leq N_p \leq 192$, and in every generation update one quarter of the total population, i.e., $24 \leq N_0 \leq 48$. The total number of structures optimized in each GA loop varies between ~10,000 and ~20,000. The use of classical auxiliary potentials for such a number of structure relaxations reduces the computational load by approximately five orders of magnitude. It usually takes 30-50 iterations to obtain the final structures and the net computational time of the entire AGA search can be reduced by more than three orders of magnitude.

In the current version of our AGA package, interfaces with first-principles DFT calculations using either VASP [Kresse and Furthmuller, 1996] or Quantum-ESPRESSO [Giannozzi *et al.*, 2009] have been implemented in a fully parallel manner. LAMMPS is used for classical potential calculations [Plimpton, 1995]. Potential fitting is carried out by force-matching method with stochastic simulated annealing algorithm as implemented in the *potfit* code [Brommer and Gahler, 2006, 2007].

2.3   Example and discussions

Structure search of TiO_2 by AGA is discussed as an example. The search used 4 formula units, i.e. 12 atoms in the unit cell. A Lennard-Jones-type EAM potential similar to that proposed by Srinivasan and Baskes [Srinivasan and Baskes, 2004] was used as our auxiliary potential:

$$E_{total} = \frac{1}{2} \sum_{i,j(i \neq j)}^{N} \phi_{ij}(r_{ij}) + \sum_{i} F_i(n_i) \tag{2.1}$$

where r_{ij} is the distance between atoms i and j and,

$$\phi(r_{ij}) = 4\epsilon \left[\left(\frac{\sigma}{r}\right)^{12} - \left(\frac{\sigma}{r}\right)^{6} \right] \tag{2.2}$$

$$F(n_i) = \alpha[\ln n_i - 1] \tag{2.3}$$

$$n_i = \sum_{j \neq i} \rho_j(r_{ij}) \tag{2.4}$$

$$\rho(r_{ij}) = \alpha \exp[-\beta(r_{ij} - r_0)] \tag{2.5}$$

Parameters of the EAM potential for pure Ti components were from the literature [Zhou *et al.*, 2004]. For oxygen, exponential decaying function (Eq. 2.5) was used as the density function and the form proposed in Ref. [Banerjea and Smith, 1998] (Eq. 2.3) was used as the embedding function. In addition, Lennard-Jones function (Eq. 2.2) was used to describe the Ti-O and O-O interaction. First-principles calculations were performed using the projector augmented wave (PAW) method [Blochl, 1994; Kresse and Joubert, 1999] within DFT as implemented in VASP code [Kresse and Furthmuller, 1996]. The exchange and correlation energy is treated within the spin-polarized generalized gradient approximation (GGA) and parameterized by Perdew-Burke-Ernzerhof formula (PBE) [Perdew *et al.*, 1996]. Wave functions are expanded in plane waves up to a kinetic energy cut-off of 500 eV. Brillouin-zone integration was performed using the Monkhorst-Pack sampling scheme [Monkhorst and Pack, 1976] over k-point mesh resolution of $2\pi \times 0.022$ Å^{-1}.

The energetic evolution versus the number of the adaptive iterations in the AGA search is plotted in Fig. 2.2. We can see that the two low-energy structures of TiO_2, i.e. the rutile structure

and the anatase structure [Cromer and Herrington, 1955] (both with 6 atoms per primitive cell), can be found within 20 AGA iterations. The theoretical structural parameters of the rutile and anatase TiO_2 together with the experimental values are listed in Table 2.1.
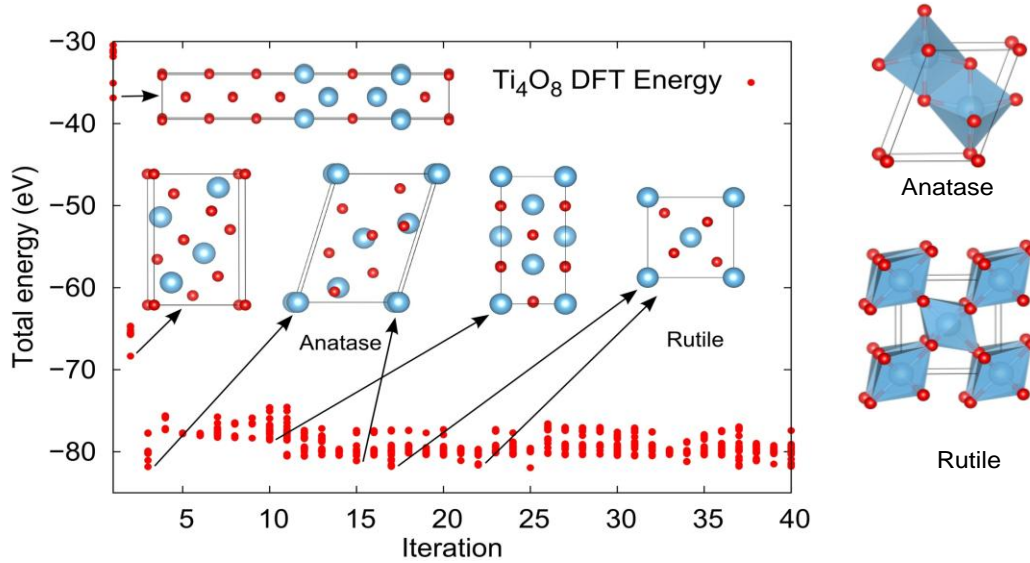
Figure 2.2 Structural and energetic evolution of TiO_2 vs. iteration number in an AGA search. Each point on this plot represents the DFT energy of a selected structure which was used for potential fitting.

Table 2.1 Structure parameters of the Rutile and Anatase TiO_2 structures from experiment and theoretical calculations.

TiO_2		Theoretical calculation	Experiment [Cromer and Herrington, 1955]
Space group		Rutile $P4_2/mnm$	
(a, c) (Å)		(4.6501, 2.9697)	(4.5929, 2.9591)
Ti	2a	(0.0000, 0.0000, 0.0000)	(0.0000, 0.0000, 0.0000)
O	4f	(0.3049, 0.3049, 0.0000)	(0.3056, 0.3056, 0.0000)
Space group		Anatase $I4_1/amd$	
(a, c) (Å)		(3.8074, 9.7050)	(3.7850, 9.5140)
Ti	4a	(0.0000, 0.0000, 0.0000)	(0.0000, 0.0000, 0.0000)
O	8e	(0.0000, 0.0000, 0.2067)	(0.0000, 0.0000, 0.2064)

We note that the commonly adopted approach of combining classical potentials with DFT calculations for structure optimization involves the use of a single set of classical potentials to screen all candidate structures followed by a refinement using DFT calculations. This requires accurate and transferable classical potentials capable of capturing the very-lowest (or few low) energy structures in a complex energy landscape. In contrast, from the energies of the final structures in each iteration as plotted in Fig. 2.2, we can see that AGA uses different adjusted potentials to sample structures located in different basins of the energy landscape. Each auxiliary classical potential may not just sample the structures in a particular basin, it can sample the structures in a subset of the basins in the energy landscape and some may overlap with those from other potentials. In another word, AGA is not designed to fit transferable potentials for general atomistic simulations. It is actually very difficult or even impossible to fit a classical potential to accurately describe a system under different bonding environments, especially for systems with multiple components. However, it is possible to adjust our auxiliary potentials to describe structures located within different subset of basins in the energy landscape with DFT accuracy. Adapted auxiliary potentials, which are adjusted throughout the AGA iterations, help the system hop between basins and ensure efficient and accurate sampling. Take the search for the crystal structure of TiO_2 with EAM potentials as example, we do not expect EAM potentials can describe the energies of various TiO_2 polymorphs very well, yet the two most stable structures of TiO_2 can be located successfully.

With above said, there is one drawback about the AGA as an optimization algorithm. From the flowchart, it can been seen that the adaptive loop is controlled and terminated by a preset number, i.e. there is no clear way to automatically end the AGA search. The reason is that while the fitting process allows the auxiliary potential to jump between different subset of basins

in the energy landscape, it usually cannot be guaranteed that the newly fitted potential leads to better results compared with the previous iteration. Nonetheless, with properly selected potential forms, the AGA searches are controllable in an empirical way. Based on our experiences, when the EAM form is used as the auxiliary potential in alloy systems, the potential fitting behaves very well.

We have successfully applied the AGA method to a variety of systems, for example, we resolved the crystal structures of CaO_2 [Zhao *et al.*, 2013] and "$Co_{11}Zr_2$" intermetallic polymorphs [Zhao *et al.*, 2014a] which remained mysterious for over 30 years, and proposed crystal structures for the cuprous chalcogenides (Cu_2Te and Cu_2Se) as thin film solar cell materials [Nguyen *et al.*, 2013]. We also predicted the existence of new stable phases in Re-B system for ultra-hard materials [Zhao *et al.*, 2014c] and several new low-energy and novel Si allotropes [Nguyen *et al.*, 2014], etc. In the following three chapters, some of those works will be discussed.

CHAPTER 3.   NON-RARE EARTH MAGNETS

Permanent magnets are one of the earliest functional materials and essential components in modern technologies. They are used in many electric and electronic devices from computers, motors and generators, medical equipment and so on. It has also been proved that traction motors in electrical vehicles and wind turbine generators using permanent magnets are more energy efficient compared with other options [Poudyal and Liu, 2013].

Among all types of permanent magnets, the rare earth (RE) magnets, particularly neodymium magnets and samarium-cobalt magnets have been the strongest since their discovery in the 1960s and '80s. They produce very strong magnetic field and tend to resist demagnetization extremely well. Since their prices became competitive in the 1990s, RE magnets have been replacing alnico and ferrite magnets in many applications requiring powerful magnets. However, towards the 21st century, seeking more efficient energy use to control global emission of greenhouse gases has caused an escalation of demand for electric cars and wind-powered electric generators. This increased demand was accompanied by great pressures with regard to RE production and supply, and consequently dramatic increase of price.

One way to solve the issue is to find replacement to the RE magnets. However, the advantages of permanent magnet-based machines disappear if lower-energy-product magnets, such as current non-RE permanent magnets, are used [McCallum *et al.*, 2014]. Therefore, there has been a strong need to design new powerful magnetic materials or improve the existing non-RE permanent magnets to meet the demanding performance criteria. In this chapter, some of our work on understanding and further improving the structural and magnetic properties of several promising non-RE systems are discussed.

3.1   Unraveling the structural mystery of "Zr_2Co_{11}" polymorphs[1]

3.1.1   Introduction

In recent years, increasing demand for permanent-magnet materials coupled with limited RE mineral resources and limited RE supplies have spurred the need to discover viable replacement compounds for the rare earth based magnets [Critical Materials Strategy, 2011; Kramer *et al.*, 2012]. In particular, much attention has been focused on Zr_2Co_{11} and related phases prepared in various ways [Demczyk and Cheng, 1991; Gabay *et al.*, 2001; Ivanova *et al.*, 2007, 2009; Zhang *et al.*, 2013; Balasubramanian *et al.*, 2013]. Studies have shown that some of the metastable phases close to the Zr_2Co_{11} intermetallic compound, resulting from the rapid quenching, exhibit strong magnetocrystalline anisotropy with a Curie temperature around 500 ℃ [Demczyk and Cheng, 1991; Gabay *et al.*, 2001]. However, the crystal structures of these phases remained unsolved. Multiple phases and small grain sizes in experimental samples make it difficult to determine the atomic decoration of the crystal structures of this compound using standard X-ray techniques. Even the exact compositions, the shape and size of the unit cells of the observed phases are under debate. The uncertainty in the crystal structures greatly hinders further development and optimization of the material for practical applications.

3.1.2   Results and discussions

In order to resolve the atomic structures of the Zr_2Co_{11} polymorphs, we performed a systematic crystal structure search for the $ZrCo_{5+x}$ compounds with x = 0.0, 0.1, 0.2, 0.25, and 0.5 using AGA [Wu *et al.*, 2014]. The global structure optimizations were performed without any assumptions on the Bravais lattice type, atom basis or unit cell dimensions. For this system,

---

[1] This part is a modified version of the published article: Zhao, X., Nguyen, M. C., Zhang, W. Y., Wang, C. Z., Kramer, M. J., Sellmyer, D. J., Ke, L. Q., Antropov, A. P. and Ho, K. M. "Exploring the structural complexity of intermetallic compounds by an adaptive genetic algorithm", *Phys. Rev. Lett.* **112**, 045502 (2014).

the auxiliary classical potentials in the form of EAM [Daw and Baskes, 1984] were adopted. The potential parameters for Zr-Zr and Co-Co interactions, the embedded energy functions and density functions were taken from the literature [Zhou *et al.*, 2004], while the Zr-Co interaction was modeled by a Morse function with 3 adjustable parameters (Eq. 3.1).

$$\phi(r_{ij}) = D\left[e^{-2\alpha(r_{ij}-r_0)} - 2e^{-\alpha(r_{ij}-r_0)}\right] \tag{3.1}$$

The potential parameters were adjusted adaptively by fitting to the DFT energies, forces, and stresses of selected structures according to AGA procedure. The fitting was performed by the force-matching method with stochastic simulated annealing algorithm implemented in the *potfit* code [Brommer and Gahler, 2006, 2007]. The *ab initio* calculations were performed using spin-polarized density functional theory within generalized-gradient approximation (GGA) with projector-augmented wave (PAW) method [Blochl, 1994; Kresse and Joubert, 1999] by VASP code [Kresse and Furthmuller, 1996]. The GGA exchange correlation functional parameterized by Perdew, Burke and Ernzerhof (PBE) was used [Perdew *et al.*, 1996]. The kinetic energy cutoff was 350 eV and the Monkhorst-Pack's scheme [Monkhorst and Pack, 1976] was used for Brillouin zone sampling with a dense k-point grid of $2\pi \times 0.025$ Å^{-1}.

From the AGA searches, we found many crystal structures with closely competitive energies. The lowest-energy structures at different compositions are plotted in Fig. 3.1. Among the different compositions studied by AGA, the $ZrCo_{5.25}$ structure (formula Zr_4Co_{21}; primitive cell is monoclinic containing 50 atoms) is found to be closest to the tie-lines defining the Co + Zr_6Co_{23} equilibrium. This structure can be considered as a derivative of the $SmCo_5$ structure. As shown in Fig. 3.1, the Zr-Co layer in $ZrCo_{5.25}$ (layer # 2) is similar to the Sm-Co layer in $SmCo_5$ except that the Zr atoms are slightly out of the plane. There are two types of pure Co planes in

the $ZrCo_{5.25}$ structure: one (layer #1) is the same as the pure Co layer in $SmCo_5$, while the other (layer #3) is a rippled hexagonal layer. The rippling periodicity is about 17Å, which explains the nature of the modulation along [010] direction observed in experiments [Ivanova and Shchegoleva, 2009]. Various low-energy structures of $ZrCo_{5.1}$, $ZrCo_{5.2}$, $ZrCo_{5.25}$, and $ZrCo_{5.5}$ obtained from our GA search represent different lateral shifts between neighboring blocks of the basic 3-layer motif, caused by the strain in the densely packed Co layer (layer #3), which has different densities and different strains depending on the Co concentration of the compound.
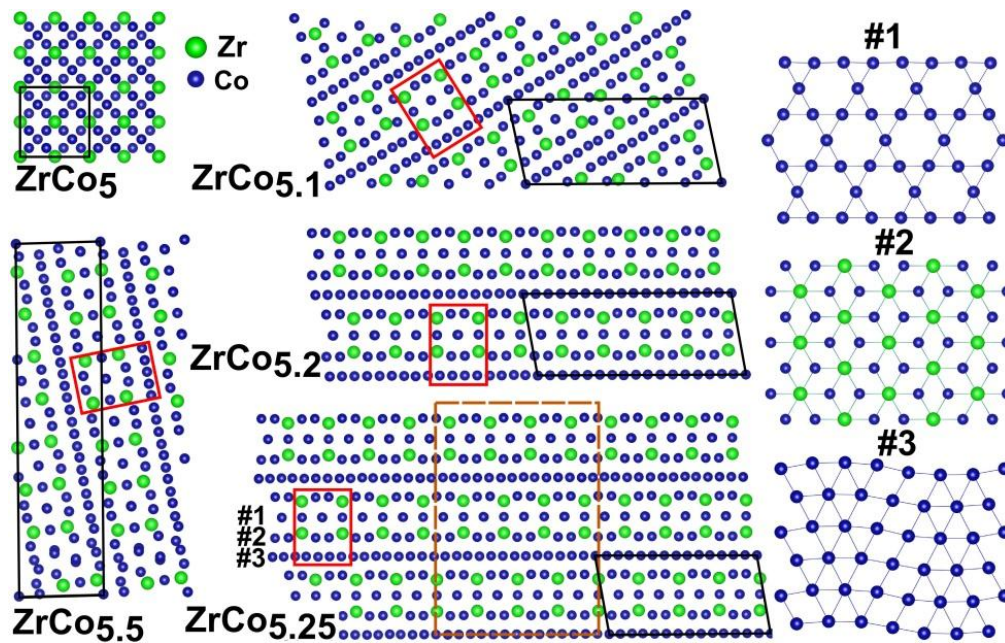
Figure 3.1 Lowest energy structures of $ZrCo_{5+x}$ from AGA searches. The black boxes indicate the unit cell for each structure. The largest unit cell used in our GA search contains 117 atoms at the composition of $ZrCo_{5.5}$. The red boxes indicate the common structure motif in the obtained structures. The brown box in the $ZrCo_{5.25}$ structure shows the supercell of the monoclinic structure corresponding to the experimentally observed "orthorhombic" structure with 150 atoms per unit cell. Top views of different layers in the common structure motif, labeled as #1, #2 and #3 respectively are plotted on the right.

Several years ago, Ivanova *et al*. [Ivanova *et al*., 2007, 2009] were able to carry out an X-ray diffraction (XRD) analysis using a large grain from one of their samples and identified the

compound's crystal structure as rhombohedral with a_{rhomb} = 4.76 Å and c_{rhomb} = 24.2 Å (in the hexagonal setting). A decrease in temperature induces a transformation into an orthorhombic structure with a_{orth} = 4.71 Å, b_{orth} = 16.7 Å, and c_{orth} = 24.2 Å. Evidence for a hexagonal, high-temperature phase with a_{hex} = a_{rhomb} and c_{hex} = $2c_{rhomb}/3$ was also observed from their TEM analysis. Some of these phases were confirmed by the recent work of Zhang *et al.* [Zhang *et al.*, 2013]. However, these experiments were not able to determine the atom positions in the proposed crystal structures.
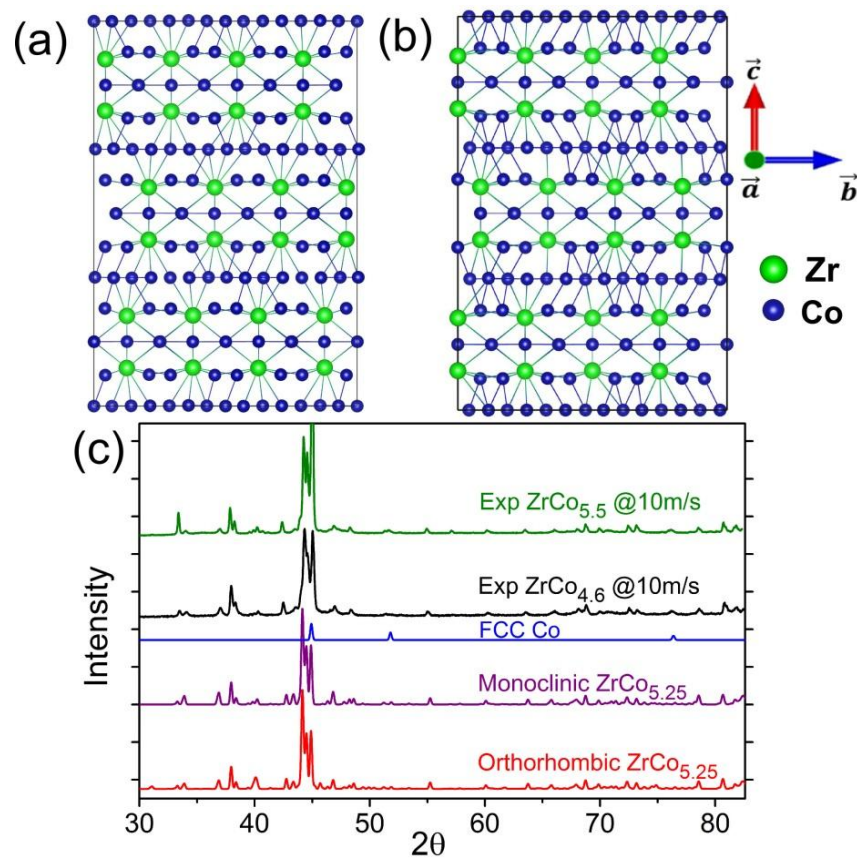
Figure 3.2 (a) Atomic structure with monoclinic symmetry. (b) Atomic structure with orthorhombic symmetry. (c) Comparison of the simulated XRD spectra from the predicted orthorhombic and monoclinic structure models (red and purple) with experiments (black and green, 10 m/s indicates the wheel speed). The blue line shows the XRD spectrum from fcc-Co structure. Cu Kα line and a broadening factor $B(2\theta) = 3.1 \times 10^{-3}/cos\theta$ were used in the simulation [Langford and Wilson, 1978].

We note that the lowest-energy $ZrCo_{5.25}$ structure from our prediction is consistent with the low-temperature orthorhombic phase reported by Ivanova *et al.* and Zhang *et al*. Two of its three lattice parameters (a = 4.68 Å, b = 16.34 Å) match well with the experimental values. The third lattice parameter along the c axis is 8.10 Å in our structure, which is about 1/3 of that in the experiment (24.2 Å). The Bravais lattice type of our structure is monoclinic rather than orthorhombic. However, if we allow this monoclinic structure to repeat three times along the *c*-axis to define a new unit cell, we can obtain a structure [Fig. 3.2(a)] with an almost orthorhombic cell containing 150 atoms with a = 4.68 Å, b = 16.54 Å, c = 24.08 Å, $\beta = \gamma = 90°$ and $\alpha = 90.09°$, after refinement using first-principles calculations. Another structure shown in Fig. 3.2(b) with orthorhombic symmetry and about 1 meV/atom higher in energy can also be constructed from the new 150-atom $ZrCo_{5.25}$ model by shifting part of it along b axis. More details about how the 150-atom structures are constructed can refer to the Supplemental Material of Ref. [Zhao *et al.*, 2014a]. The simulated XRD patterns from these two structures are nearly identical and would be difficult to distinguish in experiments. The simulated XRD spectra of our $ZrCo_{5.25}$ models agree well with the experimental data as can be seen from Fig. 3.2(c). In the experiments, ingots of $ZrCo_{5+x}$ were arc melted from high-purity elements in an argon atmosphere. The ribbons were made by ejecting molten alloys in a quartz tube onto the surface of a copper wheel rotating with different speeds. The ribbons are about 2 mm wide and 50 μm thick. The phase components were examined by Rigaku D/Max-B X-ray diffraction. Note that some peaks observed in the experimental data can be attributed to the presence of fcc Co phase. Energy-dispersive X-ray spectroscopy analysis shows that Co/Zr ratio in the orthorhombic phase is very close to 5.25, agreeing well with our theoretical prediction.
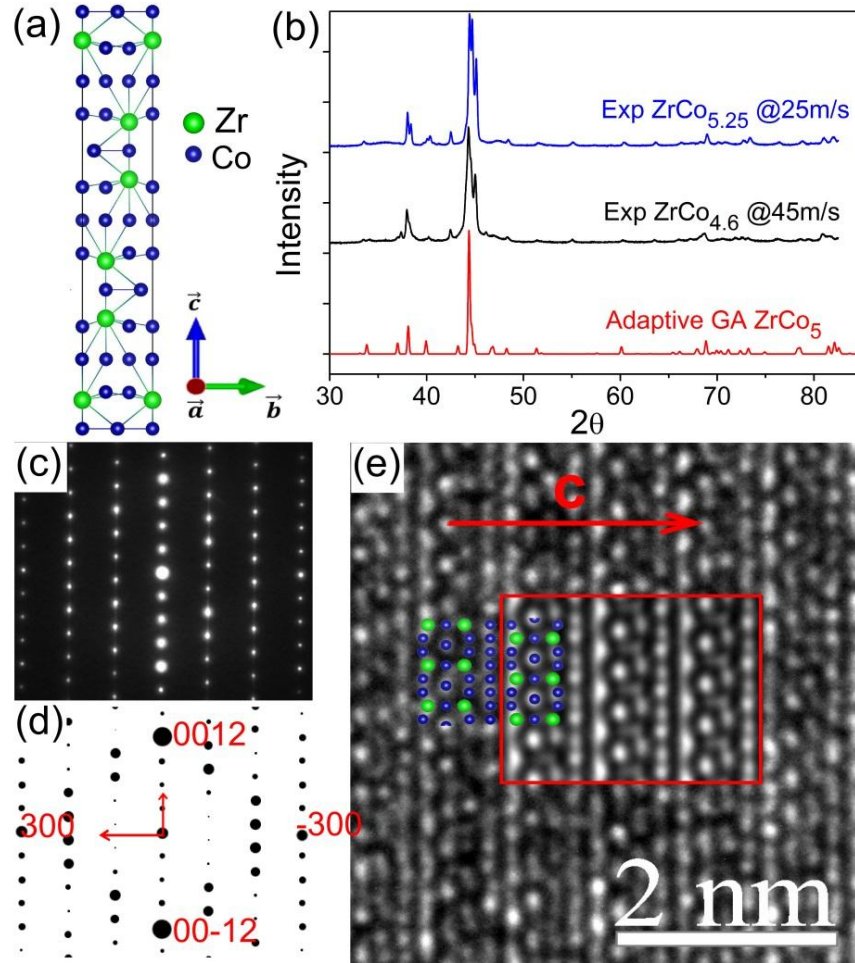
Figure 3.3 (a) Atomic structure proposed for the rhombohedral phase. (b) Comparison of simulated XRD spectrum from the rhombohedral structure model (red) with experiments (black and blue, wheel speeds are given). Cu Kα line and a broadening factor $B(2\theta) = 3.1 \times 10^{-3}/cos\theta$ were used in the simulation [Langford and Wilson, 1978]. (c, d) Experimental and simulated [Li, 2012] selected-area electron diffraction (SAED) patterns along [010] direction. (e) HREM image taken along the [010] zone axis. The red arrow indicates the repeat distance along the c-axis. Inset within the red box is the simulated HREM image and the structure model (green for Zr and blue for Co) is laid on top.

In our search, when the Co concentration is reduced, the distorted hexagonal plane of pure Co (layer #3, Fig. 3.1) relaxes towards an ideal hexagonal arrangement. Therefore, by reducing the Co concentration in the distorted hexagonal plane of the ZrCo$_{5.25}$ structure, the

atomic structures for the rhombohedral and hexagonal phases at the composition of $ZrCo_5$ can be obtained. The structures for the rhombohedral phase with 36 atom/cell and for the hexagonal phase with 24 atom/cell are shown in Fig. 3.3(a) and the inset of Fig. 3.4(b), respectively. The rhombohedral structure has space group $R32$ with lattice parameters $a = 4.69$ Å and $c = 24.02$ Å, which match well with experimental data [Ivanova *et al.*, 2007; Zhang *et al.*, 2013]. The hexagonal structure with space group *P*-62*c*, $a = 4.69$ Å, and $c = 16.01$ Å is also in good agreement with the reported hexagonal phase [Ivanova *et al.*, 2007]. Simulated XRD pattern of the rhombohedral structure from our prediction is presented in Fig. 3.3(b) in comparison with experimental measurement. While the main features from our predicted structures agree with the experimental data, the resolution of experimental spectra is too poor (due to overlapping reflections from multiple low symmetry phases and broadened peaks due to nanoscale grains) to make further comparison. On the other hand, the structure of the rhombohedral phase can also be revealed by selected-area electron diffraction (SAED) pattern and high-resolution electron microscopy (HREM) image. Figure 3.3(c) shows the experimental SAED pattern in [010] zone axis. The diffraction spots with higher intensities are in agreement with those in the simulated SAED pattern [Fig. 3.3(d)], which are labeled, e.g. (0 0 12) and (3 0 0). Figure 3.3(e) shows the HREM image taken along the [010] zone axis. The repeat distance along the c-axis in the HREM image is about 2.42 nm, very close to the lattice vector along the c-axis in our theoretical model. Typical features of the image can be viewed as the stacking layers along the c axis, which is consistent with the inserted structural projection and simulated image based on the rhombohedral structure from our theoretical prediction.

In order to gain more insight into the stability of the Zr_2Co_{11} phases, the formation energies of various low-energy structures relative to the line connecting the energies of hcp Co

and $ZrCo_2$ as a function of Zr composition is investigated and plotted in Fig. 3.4(a). In the composition range shown in Fig. 3.4(a), Zr_6Co_{23} is a stable structure, consistent with the well-known phase diagram [Zhu, 2006]. The formation energies of the structures from our AGA search are close to, but a little above the tie-lines, indicating these are metastable structures. However, it is interesting to note a deep local energy minimum around $ZrCo_{5.25}$. Since the energy of the orthorhombic structure (which has the composition of $ZrCo_{5.25}$) from our prediction is well located inside this valley, it is expected that this structure can be captured under rapid quenching conditions which prevent phase segregation in the system.

Both the rhombohedral and hexagonal structures have the composition of $ZrCo_5$ but their energies are about 20 meV/atom higher than that of the Ni_5Zr-type structure. In order to compare the stability of the rhombohedral and hexagonal structures with respect to that of the Ni_5Zr-type structure at high temperatures, we calculated the free energies of the three phases by including the entropy contribution from lattice vibrations. The phonon calculations were done via the first-principles supercell approach within harmonic approximation using the VASP and *phonopy* codes [Togo *et al.*, 2008]. The results are shown in Fig. 3.4(b). We can see that although the Ni_5Zr-type structure is energetically favorable at low temperature, the rhombohedral and hexagonal structures have lower free energies above ~1200 K. Therefore, these two phases are favored at high temperature.
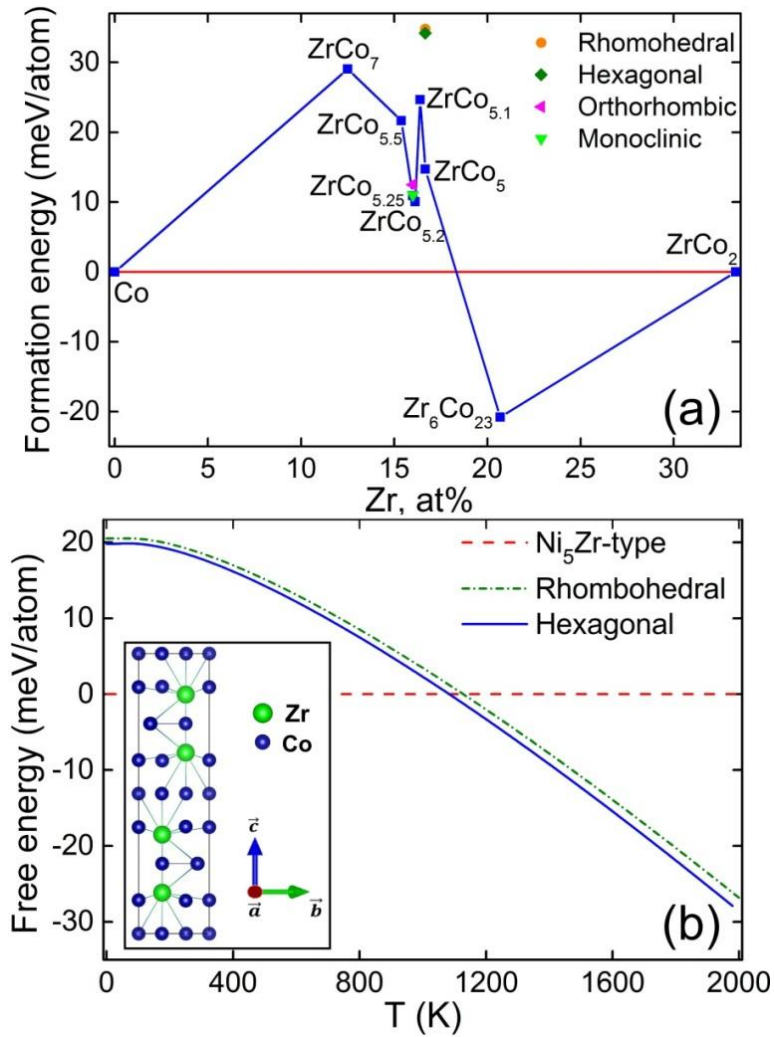
Figure 3.4 (a) Convex hull of the formation energies in Zr-Co system with Zr atomic percent $< 34\%$. The formation energy is defined relative to the hcp Co and $ZrCo_2$: $E_F(Zr_mCo_n) = [E(Zr_mCo_n) - xE(Co) - yE(ZrCo_2)]/(m + n)$, where $x = n - 2m$, $y = m$. (b) Free energy of three $ZrCo_5$ structures: the rhombohedral, hexagonal model and Ni_5Zr-type structure. The atomic structure of the hexagonal phase is shown as the inset of (b).

In experiments, the orthorhombic Zr_2Co_{11} exists not only in the low-cooling rate samples but also in the high-cooling rate samples, indicating the orthorhombic Zr_2Co_{11} is energetically favorable, consistent with our theoretical prediction. However, higher cooling rate is required to

form the rhombohedral Zr_2Co_{11}, which is a high-temperature-stable phase according to our free energy calculation [Fig. 3.4(b)].

Table 3.1   Calculated magnetic properties of different structure models. M (μ_B/atom): average magnetic moment over all atoms; K (MJ/m^3): magnetic anisotropy energy; T_c (K): Curie temperature. For M and K, both LDA and GGA (in the brackets) results are given. The easy magnetization axes of the rhombohedral and hexagonal structures are uniaxial and along c-axis of the plotted structures. The $ZrCo_{5.25}$ structure does not have uniaxial anisotropy, and the easiest axis is along *c*-axis shown in Fig. 3.2.

Structure	M	K	T_c
$ZrCo_{5.25}$*	1.05 [1.07]	0.64 [0.54]	950
$ZrCo_5$ (Ni_5Zr type)	1.09 [1.12]	~ 0	1063
Rhombohedral (*R*32)	0.92 [1.01]	1.04 [1.42]	709
Hexagonal (*P*-62*c*)	0.94 [1.01]	1.32 [1.33]	688

*The calculation on $ZrCo_{5.25}$ is done on the lowest energy structure with unit cell containing 50 atoms

We also performed first-principles calculations to study the magnetic properties of the structures discussed above, and results are listed in Table 3.1. Details of the methods used to calculate anisotropy and Curie temperature are described in Ref. [Ke *et al.*, 2013]. The magnetization in these structures (0.9 to 1.1 μ_B/atom) is much smaller than that of elemental hcp-Co (1.6 μ_B/atom), in agreement with experimental results. The large reduction of magnetization (relative to hcp-Co) can be attributed to two effects. First, Zr atoms in our structures have magnetic moments of −0.5 to −0.3 μ_B/atom, and are antiferromagnetically coupled with the surrounding Co atoms; second, Zr atoms also strongly suppress the magnetism of their nearest neighbor Co atoms, which is a consequence of the itinerant nature of Zr d-electrons. Like other transition metals at the end of the 3d row (Fe, Ni), elemental Co has unpaired electrons occupying the highest antibonding orbitals, which are the most localized. This is why metals at

the end of the 3d row are ferromagnets. On the other hand, Zr atom is at the beginning of the 4d row and has very extended wavefunctions, which overlap with the aforementioned localized orbitals of Co atoms in Zr-Co system and lead to the suppression of magnetism among Co atoms and the suppression of ferromagnetism overall. Correspondingly we also observe a large reduction of the Curie temperature relative to elemental Co. However, the Curie temperatures of Zr-Co compounds considered in this paper still remain high enough for practical use, such as in electric motors.

Magnetic anisotropy studies revealed a different picture for different structures. The results show that the cubic Ni_5Zr-type structure has a very small magnetic anisotropy, as expected. The largest anisotropy energy was found in the rhombohedral and hexagonal structures (~ 1.3 MJ/m^3). This number is nearly twice larger than the anisotropy of hcp Co. Analysis of the partial contributions to the magnetic anisotropy shows that the improvement in the uniaxial anisotropy is related to the increased anisotropy of the orbital magnetic moment of Co atoms with the largest orbital moment corresponding to the easy-axis direction. Thus the observed high coercivity in Zr-Co alloys can be attributed to intrinsic magnetic effects: significant decrease of magnetization and a large increase of magnetic anisotropy. Our results are consistent with the experimental measurements and indicate that the high temperature rhombohedral/hexagonal phases correspond to the hard magnetic phase in Zr_2Co_{11} compounds.

3.1.3 Conclusions

In summary, we showed that the adaptive genetic algorithm method gives a convincing solution of the long-standing structural mystery in the Zr_2Co_{11} polymorphs which allows us to elucidate the physical origin of high coercivity observed in this system and provides useful insight guiding further development of these materials for use as high performance permanent

magnets without rare earth elements. Resolving complicated atomistic structures with up to 150 atoms per cell by a first-principle computational approach in such a complex multiple-phase system demonstrated a new capability to aid the efficient materials discovery through the use of state-of-the-art supercomputers.

3.2 Structures and magnetic properties of Co-Zr-B magnets[2]

3.2.1 Introduction

As promising candidates for rare earth-free permanent magnets, Co_xZr alloys with x near 5 and related compounds, such as Co-Zr-B, Co-Zr-M-B (M = C, Si, Mo, etc.), have attracted considerable attentions. Great effort has been devoted to the improvement of their hard magnetic properties. The reported highest coercivity was 9.7 kOe, found in annealed $Co_{74}Zr_{16}Mo_4Si_3B_3$ ribbons [Zhang *et al.*, 2014] and the optimal magnetic properties were obtained in $Co_{80}Zr_{18}B_2$ with intrinsic coercivity $H_c = 4.1$ kOe and energy product $(BH)_{max} = 5.1$ MGOe [Chen *et al.*, 2005]. More recently, cluster beam deposition has been used to make Co-Zr/Hf samples and energy products of 16-20 MGOe were reported [Balasubramanian *et al.*, 2013, 2014]. The Co-Zr/Hf magnet alloys typically contain multiple phases and identifying the phase responsible for the magnetic hardness has been one of the research focuses. Several studies [Stroink *et al.*, 1990; Saito, 2003a; Zhang *et al.*, 2010] assumed that the hard magnetic phase in the Co-Zr system is the metastable Co_5Zr phase with the structure of Ni_5Zr. However, Ni_5Zr structure is cubic and thus unlikely to provide strong magnetocrystalline anisotropy energies, which was confirmed by first-principles calculations [Zhao *et al.*, 2014a]. Co_3ZrB_2 has also been proposed to be a

---

candidate for the hard magnetic phase [Schobel and Stadelmaier, 1969], which remains to be validated.

Determining the hard magnetic phase in the above-mentioned alloys has been a long-standing issue due to the ambiguity of their crystal structures. Recently, progress has been made in solving the crystal structures of the complex Co_xZr alloys as discussed in the first part of this chapter. Using AGA, we studied the crystal structures of the rhombohedral, hexagonal, and orthorhombic polymorphs close to the $Co_{11}Zr_2$ intermetallic compound [Zhao *et al.*, 2014a]. The common building block in the structures of these polymorphs was identified as a derivative from the $SmCo_5$ structure. Decrease of the temperature induces a phase transition from high symmetry rhombohedral/hexagonal phase to low symmetry orthorhombic/monoclinic phase, along with a slight increase of the Co concentration. The experimental data from the X-ray diffraction (XRD) and transmission electron microscopy were well explained by the crystal structures obtained from AGA searches. Through first-principles magnetic properties calculations, the hard magnetic phase in the Co_xZr alloys was identified to be the high temperature rhombohedral/hexagonal phase.

In this part, we extended the investigation to the effect of boron doping on the structures and magnetic properties of the Co_xZr alloys. Structure searches by AGA allowed us to access the preferred positions of boron atoms, thus energetics and magnetic properties of different Co-Zr-B compositions can be studied by first-principles calculations.

3.2.2   Computational details

Crystal structures of Co-Zr-B were investigated by AGA. The structure searches were performed without any assumption on the Bravais lattice type, atom basis or unit cell dimensions. The size of the unit cell studied in this work was up to 100 atoms. In the AGA

search for this system, EAM potential [Daw and Baskees, 1984] was used as the auxiliary classical potential. The parameters for Co-Co and Zr-Zr interactions were from the literature [Zhou *et al.*, 2004]. B-B interaction and the crossing-pair interactions (i.e. B-Co, B-Zr, and Co-Zr) were modeled by Morse function (Eq. 3.1), with 3 adjustable parameters each (D, α, r_0). For Co and Zr atoms, parameters of the density function and embedding function were taken from Ref. [Zhou *et al.*, 2004] as well, and for B atom, exponential decaying function was used as the density function (Eq. 2.5, with 2 adjustable parameters: α, β) and the form proposed by Benerjea and Smith [Banerjea and Smith, 1998] was used as the embedding function (Eq. 3.2, with 2 adjustable parameters: F_0, γ).

$$F(n) = F_0[1 - \gamma \ln n]n^\gamma \tag{3.2}$$

The total energy of the system then has the form of Eq. 2.1.

The potential parameters were adjusted adaptively by fitting to the DFT energies, forces, and stresses of selected structures according to the AGA scheme. The fitting was performed by the force-matching method with stochastic simulated annealing algorithm implemented in the *potfit* code [Brommer and Gahler, 2006, 2007]. First-principles calculations were performed using the projector augmented wave (PAW) method [Blochl, 1994; Kresse and Joubert, 1999] within density functional theory (DFT) as implemented in VASP code [Kresse and Furthmuller, 1996]. The exchange and correlation energy is treated within the spin-polarized generalized gradient approximation (GGA) and parameterized by Perdew-Burke-Ernzerhof formula (PBE) [Perdew *et al.*, 1996]. Wave functions are expanded in plane waves up to a kinetic energy cut-off of 350 eV. Brillouin-zone integration was performed using the Monkhorst-Pack sampling scheme [Monkhorst and Pack, 1976] over k-point mesh resolution of $2\pi \times 0.033$ Å^{-1}. The formation energy E_F of the alloy is calculated as:

$$E_F = \left[E\left(\mathrm{Co_m Zr_n B_p}\right) - m \cdot E(\mathrm{Co}) - n \cdot E(\mathrm{Zr}) - p \cdot E(\mathrm{B})\right]/(m + n + p) \qquad (3.3)$$

Where $E\left(\mathrm{Co_m Zr_n B_p}\right)$ is the total energy of the $\mathrm{Co_m Zr_n B_p}$ alloy; $E(\mathrm{Co})$, $E(\mathrm{Zr})$ and $E(\mathrm{B})$ are the energy per atom of Co, Zr and B in the reference structures, which are hcp Co, hcp Zr, and α-boron respectively.

Intrinsic magnetic properties of the Co-Zr-B structures, such as magnetic moment and magnetocrystalline anisotropy energy (MAE) were calculated using VASP code. The spin-orbit coupling (SOC) is included using the second-variation procedure [Koelling and Harmon, 1977]. We also calculated the MAE of the rhombohedral Co₅Zr structure by carrying out all-electron calculations using the full-potential (FP) LMTO method to check VASP calculation results. In addition, by evaluating the SOC matrix elements, the anisotropy of orbital moment and MAE was resolved into sites, spins and orbital pairs [Antropov *et al.*, 2014] to identify their contribution to the magnetic properties. Curie temperature (T_c) is checked for selected structures using mean-field approximation and more details can be found in Ref. [Ke *et al.*, 2013].

3.2.3   Results and discussions

To validate the selection of the auxiliary classical potential, we first performed crystal structure search for the $\mathrm{Co_3 Zr B_2}$ phase, whose crystal structure was well-characterized. The ground state structure of $\mathrm{Co_3 Zr B_2}$ was successfully found in the AGA search with above setup [Wu *et al.*, 2014]. Further calculations on its magnetic properties by DFT showed this phase is non-magnetic with zero magnetic moments. Therefore, this structure cannot be responsible for the hard magnetic properties observed in the Co-Zr-B system.

In order to obtain practically useful magnets, we then performed extensive AGA searches for Co-Zr-B with Co:Zr ratio around 5 and boron composition less than 6 at %. The contour map of their formation energies is plotted in Fig. 3.5 where the compositions searched in current work

are represented by squares. It can be seen that near the Co_5Zr composition (Co, at % ~ 83.3%) there is a local minimum in the energy landscape, which explains the Co_xZr (x ~ 5) phases obtained in experiments. For certain compositions at the high energy areas, such as $Co_{84}Zr_{15}B$, and $Co_{46}Zr_8B_2$, it is unlikely to synthesize such compounds experimentally. Among the compositions considered in Fig. 3.5, the lowest formation energy is found around $Co_{40}Zr_9B$ and $Co_{40}Zr_8B_2$, which are consistent with experimental results since most of samples produced by experiments were around these compositions [Ishikawa and Ohmori, 1990; Chen *et al.*, 2005; Chang *et al.*, 2013]. In the following, structures and magnetic properties of the Co-Zr-B alloys will be discussed respectively.
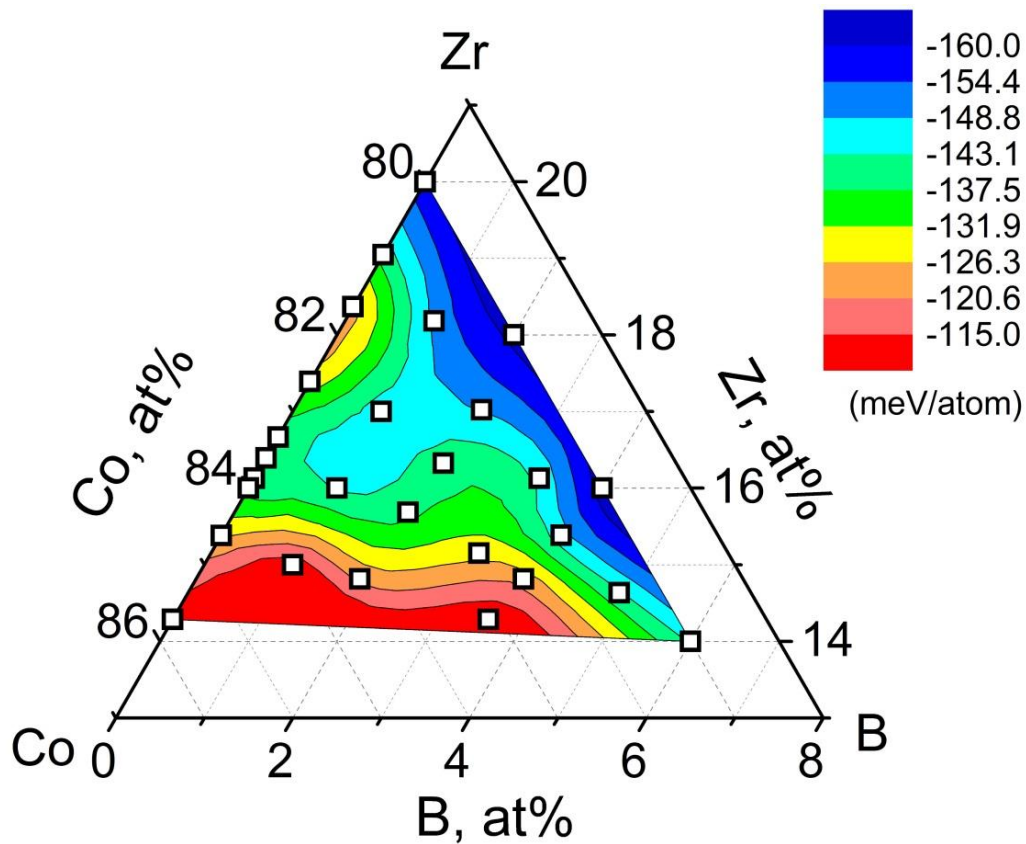
Figure 3.5 Contour map of the formation energies in the Co-Zr-B system. Only partial composition range is considered and the squares represent the compositions searched by AGA in the present work.

3.2.3.1 Structures

Several low-energy boron-doped Co_xZr structures obtained from our AGA searches are plotted in Fig. 3.6(a-d). Co and Zr atoms form the same building block as discovered in Co_xZr (Fig. 3.1), while boron atoms can either substitute Co atoms [e.g. Fig. 3.6(a)] or occupy interstitial positions [e.g. Fig. 3.6(c)] in company with local distortions. In the $Co_{40}Zr_8B_2$ structure plotted in Fig. 3.6(b), boron atoms can be considered as interstitial atoms in the Co_5Zr structure of high temperature phase, or as substitutional atoms in the $Co_{5.25}Zr$ structure of low temperature phase, because the main difference between the Co_5Zr and $Co_{5.25}Zr$ structures comes from the different packing density of one of the two pure Co layers. In our previous study, we also showed the layer-stacking feature in Co_xZr polymorphs is frequently interrupted to adjust the strain due to the rippled hexagonal Co layer. Figure 3.6(d) shows a similar structure with boron atoms located at the interruption site.

To give a better picture of the local environments of boron atoms, Fig. 3.6(e) listed several typical boron-centered clusters found in the Co-Zr-B structures. In general, the nearest neighbor distances for the B-Co and B-Zr pairs are about 2.1 Å and 2.6 Å, respectively. The coordination number of the boron atoms is 7 or 8, and the neighboring atoms are found to be Co or Zr atoms in most cases. The effect of different boron positions on the magnetic properties will be discussed later.
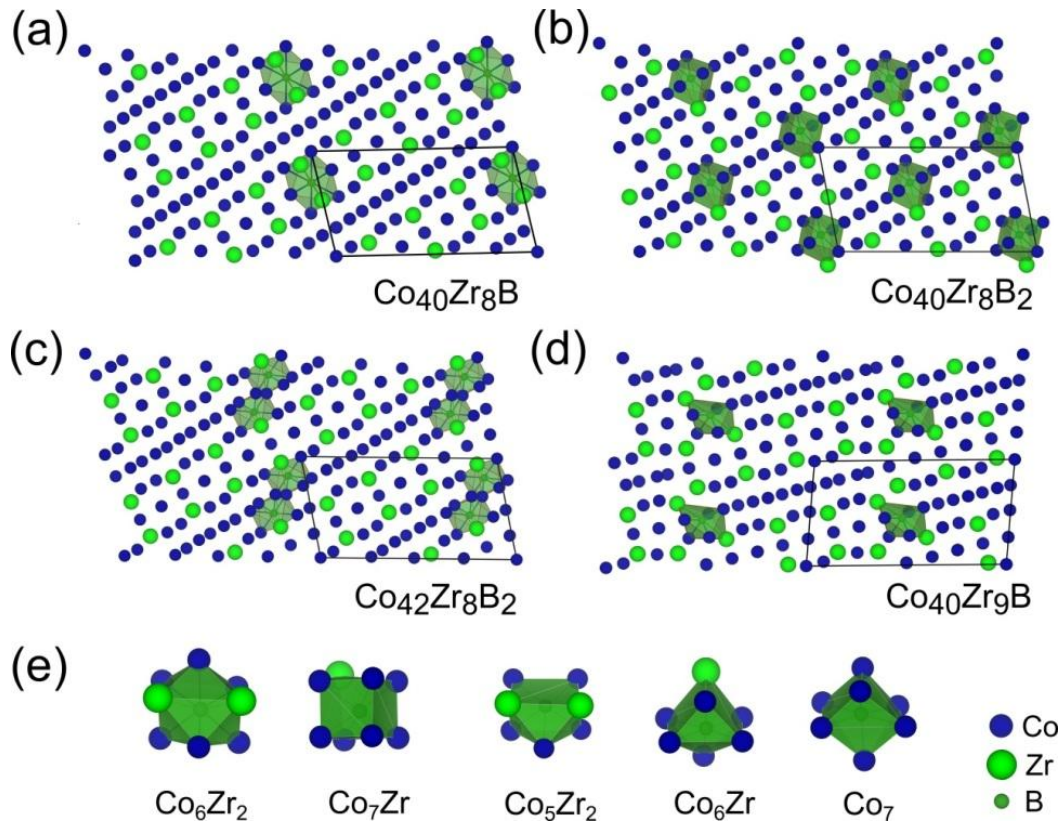
Figure 3.6 Examples of the low-energy structures obtained from the AGA searches with compositions of (a) $Co_{40}Zr_8B$; (b) $Co_{40}Zr_8B_2$; (c) $Co_{42}Zr_8B_2$; (d) $Co_{40}Zr_8B$. Unit cell of each structure is indicated by black lines. (e) Typical boron-centered clusters extracted from the Co-Zr-B crystal structures. The label under each cluster represents the neighboring atoms of boron.

The structure and glass formability in the Co-Zr-B alloy system have been studied experimentally [Saito, 2003b; Yuan *et al.*, 2008; Saito and Itakura, 2013]. In the XRD analysis [Saito, 2003b], the intensity of the crystalline peaks becomes weaker and broader as the boron content increases, indicating the reduction of the crystalline size in the samples. Amorphous and partially crystalline alloys have also been observed in this system [Ghemawat *et al.*, 1989; Yuan *et al.*, 2008]. From the AGA search, we found that all the low-energy structures of Co-Zr-B have low symmetries (triclinic system) due to the distortions induced by the doping of boron atoms. Moreover, many different structures were found to have closely competitive energies (within a

few meV per atom), similar to the Co_xZr binary system. Therefore, in the composition range plotted in Fig. 3.5, growing single crystals of Co-Zr-B alloy is difficult and the sample is expected to have small grains and defects.

3.2.3.2 Magnetic properties

A. High temperature Co_5Zr phase revisited

In our previous study [Zhao *et al.*, 2014a], the high-temperature rhombohedral phase was assigned to be responsible for the magnetic hardness in the Co_xZr alloys. The full potential calculation (GGA) showed it has a magnetic moment of around 1.0 μ_B/atom and MAE of 1.4 MJ/m^3. The rhombohedral structure, plotted in Fig. 3.7(a), has a space group *R*32 (#155) and 4 inequivalent Co sites as indicated by different colors in Fig. 3.7. Views along c axis of the different layers are plotted in Fig. 3.7(b). Among the four inequivalent Co sites, two of them (Co1, Co3) have nine-fold multiplicity and the other two (Co2, Co4) have six-fold multiplicity.

To examine the contribution of different sites to the magnetic properties of the rhombohedral phase, Fig. 3.8 shows the variations of orbital magnetic moments and relativistic energy as functions of the spin rotation. Rhombohedral Co_5Zr has uniaxial anisotropy. By evaluating the SOC matrix element, we found the Co3 site has in-plane magnetic easy axes while all other Co sites, especially Co4, support the uniaxial anisotropy. As shown in Fig. 3.8, the correlation between orbital moment and magnetic anisotropy is obvious. Co1, Co2 and Co4 sites have larger orbital magnetic moments along the z axis while Co3 has larger orbital magnetic moments when spin is along in-plane directions. The MAE calculated in LDA is smaller than the one calculated using PBE functional. By evaluating the SOC matrix elements, we found that this difference mostly comes from the Co1 site, whose contribution to MAE nearly disappears in LDA. The MAE contributions from all other sites barely depend on the exchange-correlation

functionals used in our calculations. Above analysis indicates if the Co3 site can be modified, such as substituting Co3 by other elements, the MAE of the system could be improved.
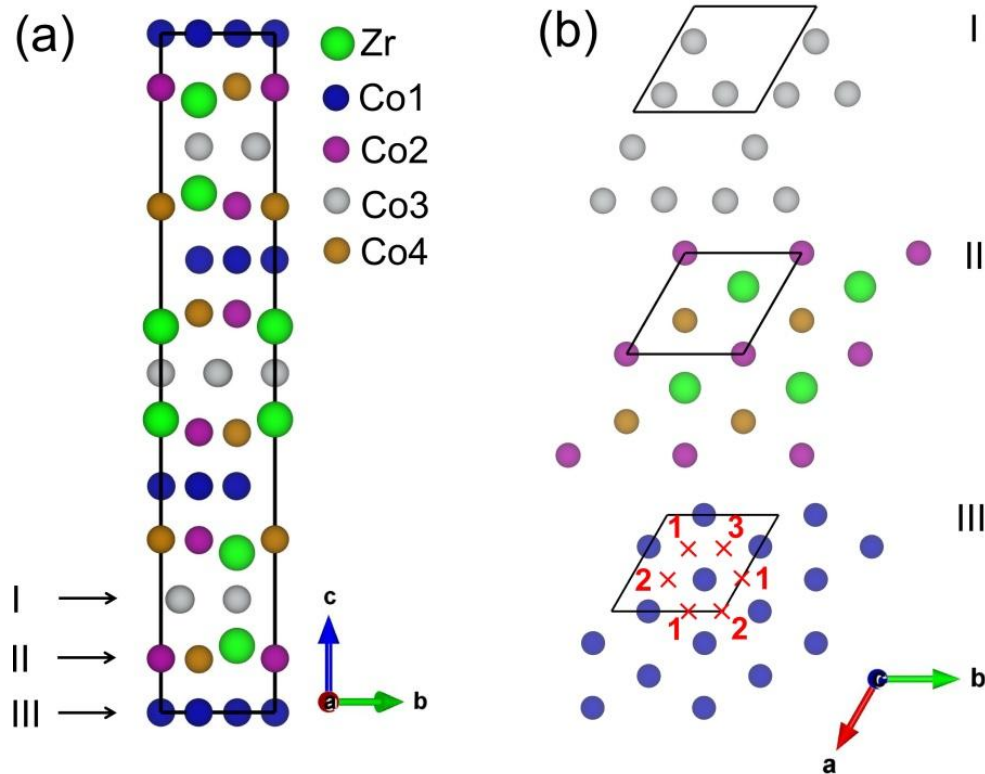
Figure 3.7 (a) Crystal structures of the rhombohedral Co_5Zr with different Co sites presented by different colors. The lattice parameters of the structure are $a = 4.66$ Å and $c = 24.0$ Å. It has one Zr site: 6c (0.0000, 0.0000, 0.4314) and four Co sites: Co1 9d (0.3300, 0.0000, 0.0000), Co2 6c (0.0000, 0.0000, 0.0795), Co3 9e (0.4946, 0.0000, 0.5000), and Co4 6c (0.0000, 0.0000, 0.2549). (b) Views of layer I, II and III along c axis. In the plot of layer III, all possible interstitial positions are grouped into 3 inequivalent sites based on symmetry. Unit cells of the crystal structures are indicated by the black boxes.
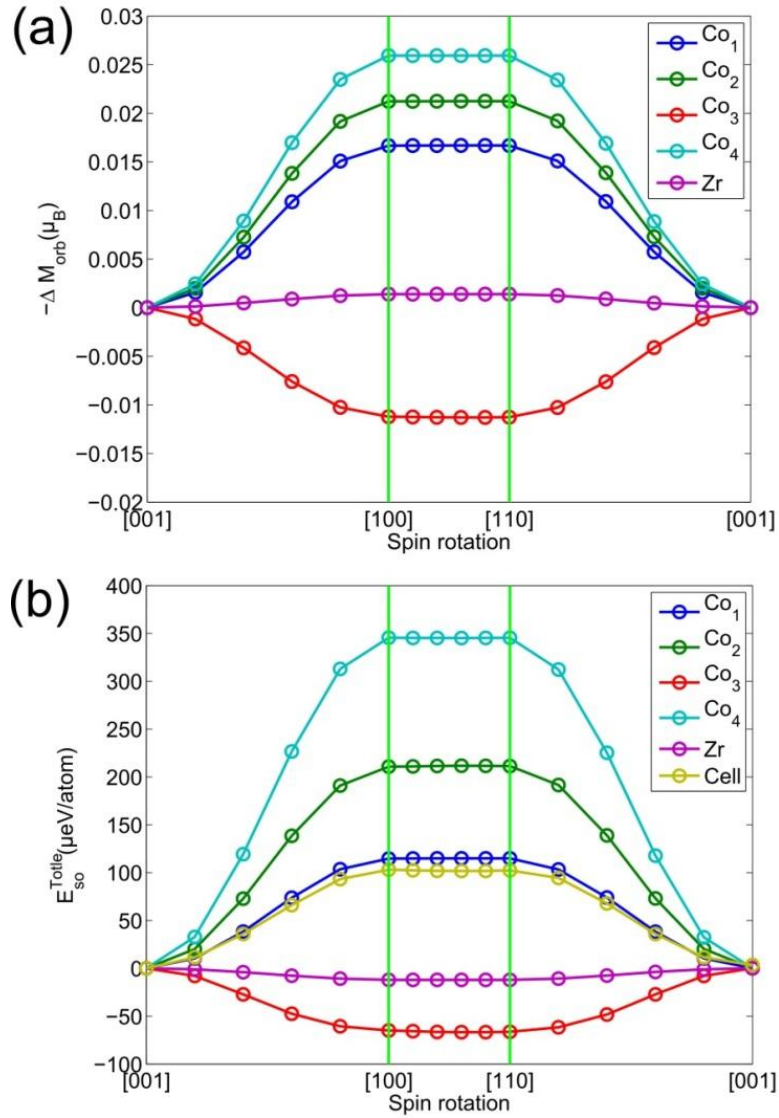
Figure 3.8 Variations of the orbital moment (a) and relativistic energy (b) as a function of spin quantization direction. Orbital moment and relativistic energy values are averaged over all atoms which belong to the corresponding inequivalent sites.

B. Boron doping on magnetic moments
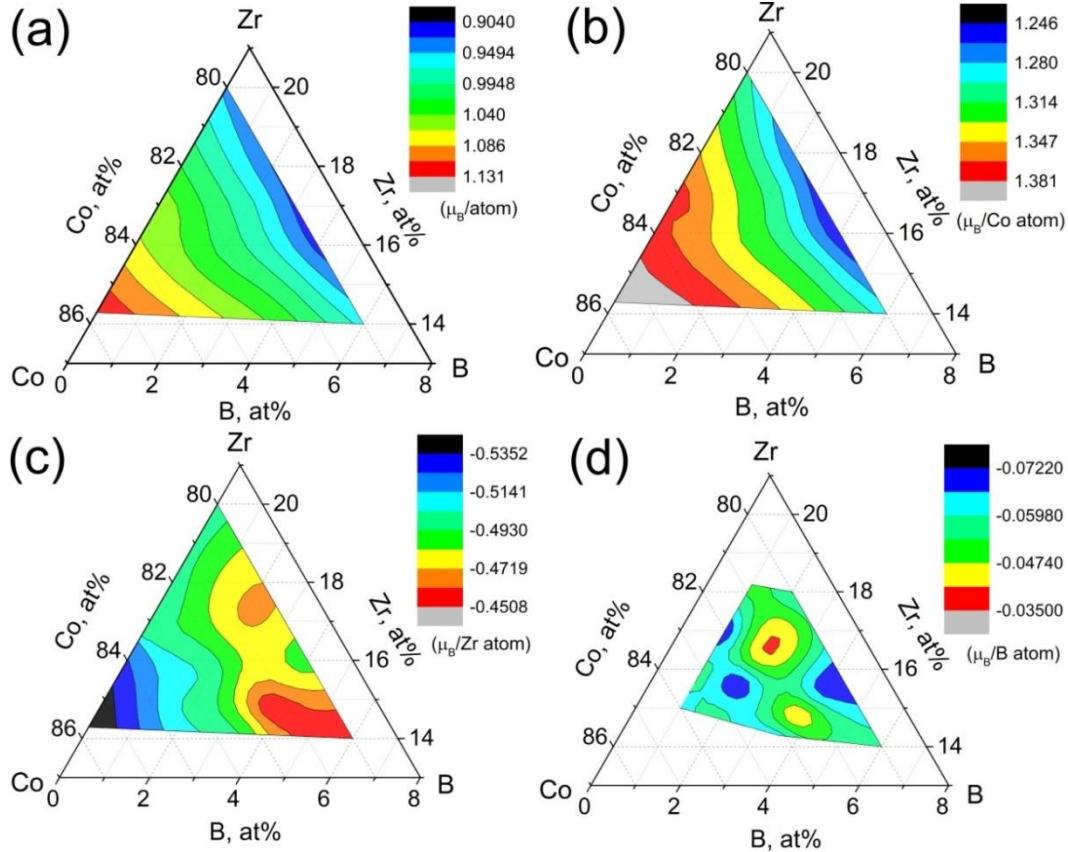
Figure 3.9   (a) Contour map of the total magnetic moment per atom in the composition range studied for Co-Zr-B; (b, c, d) contour plots of the partial contributions from Co, Zr and B atoms to the magnetic moment respectively.

To map out the magnetic moments of the Co-Zr-B alloys, results from VASP calculations were collected for all the compositions presented in Fig. 3.5. The results of total moments in the system are plotted in Fig. 3.9(a), and the partial contributions from Co, Zr, and B atoms are plotted in Fig. 3.9(b), (c), and (d) respectively. The total magnetic moment per atom is calculated as the moment of the whole system divided by the total number of atoms, while the moment contribution from atom type M (M = Co, Zr, or B) is calculated as the moment from all the M

atoms divided by the number of atom M. Results plotted in Fig. 3.9 for each composition are averaged over ten lowest-energy structures from the AGA searches.

It can be seen that the magnetization in the Co-Zr-B system mainly comes from the Co atoms. Both the Zr and B atoms are antiferromagnetically coupled to the Co atoms. As shown in Fig. 3.9(a), the magnetic moment of the system becomes smaller with the decrease of Co atomic composition, which can be explained by two reasons. First, Zr and B atoms give negative contribution to the total moment of the system. More Zr and B atoms will lower the moment of the system. Second, the Zr and B atoms suppress the moment of Co, which can be seen from Fig. 3.9(b). The average moment of the Co atoms is decreased with the increase of the Zr, B compositions. In contrast to the Co moment, the variation of the moment in Zr and B atoms as the function of composition is more complicated and there is no clear trend of how the magnetic moments of Zr and B change with composition. However, due to the small atomic percentages of the Zr and B atoms and their small moments, total magnetic moment of the system is dominated by Co atoms and varies in the same manner as that of Co.

C. Boron doping on MAE

The computational cost of calculating magnetocrystalline anisotropy energy can be enormous, which makes it infeasible to scan all the low-energy structures from AGA searches, especially when the unit cells contain as many as 100 atoms. In the following, the effect of boron doping on MAE was investigated based on the rhombohedral Co_5Zr structure and the knowledge of the preferred sites by boron atoms from above analysis. All calculations were performed using VASP. To compare, the MAE of the rhombohedral structure calculated from VASP is about 1.6 MJ/m^3, which is very close to the result from FP calculations (1.4 MJ/m^3).
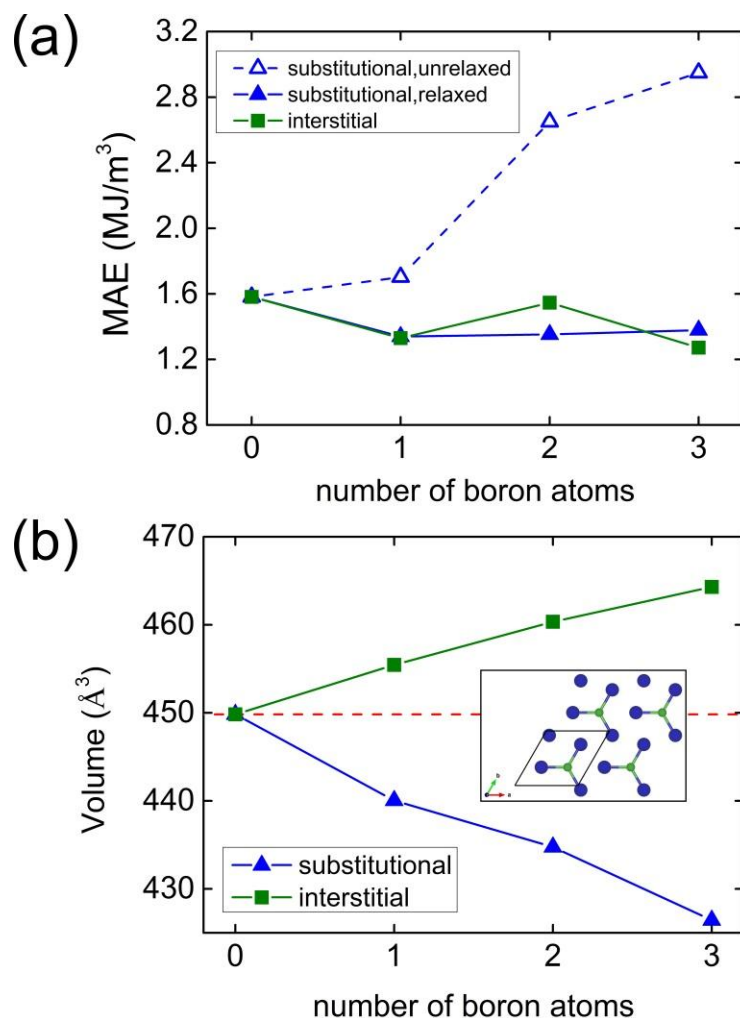
Figure 3.10 (a) Effect of boron doping on MAE. The calculations were based on the rhombohedral Co_5Zr structure. In the case of substitution, results of both the relaxed (solid triangles) and unrelaxed structures (empty triangles) are plotted, while for interstitial positions, only results of the relaxed structures (solid squares) are plotted. The positions of doped boron atoms are discussed in the main text. (b) Volume comparison between the original Co_5Zr structure (dash line) and boron doped structures after DFT relaxations. The layer III with interstitial boron atom after relaxation is plotted as the inset.

We have showed that the same structure motif found in Co_5Zr polymorphs also exists in the boron-doped Co_xZr alloys, which explains the origin of the high coercivity observed in Co-Zr-B alloys. Referring to the rhombohedral Co_5Zr structure plotted in Fig. 3.7, the boron atoms appear to prefer substituting Co atoms in layer I or entering layer III as interstitial atoms. Therefore, we scanned all the possibilities of adding up to 3 boron atoms into the conventional unit cell of the rhombohedral Co_5Zr structure [Fig. 3.7(a), 36 atoms] and selected the one with lowest energy for each scenario to calculate MAE. All structures have uniaxial anisotropy unless noted otherwise.

In the substitutional case, all the Co atoms in layer I belong to the same Wyckoff position, therefore the choices of substituting Co by B are limited. We found while substituting more than one Co atoms, lower energies were obtained with one B atom per layer, i.e. two B atoms substituting the same layer is not energetically favored for the 1×1 cell studied in this work. This can be explained by the fact that the size of the boron atom is much smaller than that of Co atom. Large distortions would be introduced if the boron density in one layer is too big. The calculated MAE results are plotted in Fig. 3.10(a) for both the relaxed and unrelaxed structures. It can be seen that the MAE increases significantly with the number of boron atoms for the unrelaxed structures, which confirms our speculation that replacing Co atoms at the Co3 site with other elements without modifying the structure can improve the MAE. However, after structure relaxations, MAE values of the boron substituted structures become slightly smaller than the original Co_5Zr structure. From volume comparisons plotted in Fig. 3.10(b), we can see the relaxation changes the structure noticeably. The changes in the environments of Co atoms cause the change of their electronic configuration and contributions to the MAE.

In the interstitial case, there are three inequivalent positions in each Co1 layer where boron atoms can occupy, as indicated in Fig. 3.7(b). We scanned all the possibilities of adding up to 3 boron atoms and plotted the MAE results in Fig. 3.10(a). Considering that interstitial defects usually introduce much larger distortions to the neighboring atoms, we only calculated the MAE of the relaxed structures. We note again that adding one boron atom into each layer III gives more competitive energy and the relaxed structure of the B-Co mixed layer is plotted as the inset of Fig. 3.10(b). The MAE data shows the interstitial boron atoms do not change the MAE too much compared with the Co_5Zr structure.

Although above calculations were performed on models that were created based on the rhombohedral Co_5Zr structure, the results are representative due to the consideration of the preferable positions of boron. In our previous study, we showed in the low temperature $Co_{5.25}Zr$ phase where extra Co atoms packed in layer III to form the orthorhombic phase, the MAE is much lower than the high temperature Co_5Zr rhombohedral phase. However, if the extra atoms are boron atoms instead, such as Fig. 3.6(b), the MAE is expected to be close to the rhombohedral Co_5Zr from above analysis. Meanwhile, when the density of boron substitution to the Co3 site is much smaller, such as Fig. 3.6(a), the distortion introduced to the neighboring atoms will be smaller, thus there exists a great chance to increase the anisotropy. Finally, we calculated the Curie temperatures for the model structures discussed above and it shows that the change in Curie temperature due to boron addition is not significant. The calculated Curie temperature is around 700 K which is high enough for practical use.

3.2.4 Conclusions

In summary, we studied the Co-Zr-B system using AGA method and first-principles calculations. We noted that the Co_3ZrB_2 phase is paramagnetic and cannot be responsible for

magnetic hardness. Near the Co_5Zr composition, the Co and Zr atoms in the structures of Co-Zr-B share the same structural motif as discovered in the Co_xZr polymorphs, while boron atoms can appear both as substitutions for Co atoms or in the interstitial positions. Based on the AGA results, we constructed the formation energy and magnetic moment contour maps for partial composition range of the Co-Zr-B system, which can be used as guidance to adjust the experimental processing to further optimize the magnetic properties.

We believe the high coercivity observed in the ternary alloy system origins from the Co-Zr layer packing feature, as in the high temperature Co_5Zr rhombohedral phase. Through the MAE calculations on Co-Zr-B model structures, we found both substitutional and interstitial boron atoms give similar magnetic anisotropy energies as the original rhombohedral Co_5Zr structure. Our calculations provide insight into the significant improvement of the MAE in Co-Zr system through chemical doping.

3.3   Lattice Monte Carlo simulations of alnico 5-7[3]

3.3.1   Introduction

Alnico is a family of FeCo-based alloys which in addition to Fe and Co are composed primarily of Al and Ni, with small amount of Ti, Cu and sometimes Nb [Kramer *et al.*, 2012; Xing *et al.*, 2013; McCallum *et al.*, 2014; Zhou *et al.*, 2014]. Alnico alloys were the strongest type of magnets before the development of RE magnets and have some of the highest Curie temperatures of any magnetic materials (around 800 ˚C), making them useful magnets even when heated red-hot. In the 1950s and 1960s, the anisotropic microstructure of alnico was achieved by adopting directional solidification processing and applying a magnetic field during

---

[3] This part is based on the published article: Nguyen, M. C., Zhao, X., Wang, C. Z., Ho, K. M. "Cluster Expansion Modeling and Monte Carlo Simulation of Alnico 5-7 Permanent Magnets", *J. Appl. Phys.* **117**, 093905 (2015).

the annealing processes. The magnetic annealing procedure creates superior alnico alloys, referred to by their grades, such as alnico 5-7, alnico 8 and alnico 9. They are now widely used in industrial and consumer applications where strong permanent magnets are needed, such as electric motors, microphones, loudspeakers and cow magnets.

Alnico magnets derive their magnetic strength due to a spinodal phase decomposition from the high-temperature homogeneous composition into a two-phase nanocomposite of ferromagnetic FeCo-rich and essentially nonmagnetic NiAl-rich phases [McCallum *et al.*, 2014]. More specifically, alnico 5-7 consists of very long FeCo-rich rods with aspect ratio of about 5:1 separated by NiAl-rich phase in a "brick-and-mortar" pattern in the perpendicular plane cutting through the rods. The cross-sections of the FeCo-rich rods are 50 ~ 100 nm. Alnico 8 and alnico 9 show nanoscale "mosaic" structures with "tiles" of similar sizes, about 35 nm across. The aspect ratio of the FeCo-rich rods in alnico 8 varies from 1:1 to 10:1, whereas that of alnico 9 is greater than 10:1 [Xing *et al.*, 2013; Zhou *et al.*, 2014]. Previous studies have defined the general features of alnico at large scale, but the structure at the atomic scale has not been resolved clearly, e.g. whether the FeCo-rich phase is in BCC or B2 order and whether the NiAl-rich phase is in BCC, B2 or L2$_1$ order. Such ambiguity blocks the understanding of the magnetic properties of alnico from atomic view point. In addition, atomic scale picture is also necessary to understand the role played by the phase boundary between the FeCo-rich and NiAl-rich phases in further enhancing their magnetic strength.

It is known from experiments that the two phases in alnico alloys have the underlying lattice of BCC [Xing *et al.*, 2013; McCallum *et al.*, 2014; Zhou *et al.*, 2014]. With a fixed lattice as input, the cluster expansion (CE) method is the most suitable energy model to describe the alnico system, especially when the simulation requires thousands of atoms or even more due to

the complexity of the alnico alloys. With CE coefficients obtained via fitting to the energies of DFT calculations, we performed lattice Monte Carlo (MC) simulations [Metropolis and Ulam, 1949] to investigate the phase selection, site occupation and phase boundaries in alnico 5-7 at atomic scale.

3.3.2 Computational details

DFT were used to calculate the energies of the reference structures to fit CE coefficients and the fitting was performed by ATAT code [van de Walle *et al.*, 2002a, 2009]. As alnico 5-7 alloys mainly consist of Al, Ni, Co, and Fe, a set of 600 structures with a $2 \times 2 \times 2$ supercell composited of above 4 elements was chosen as fitting targets and all structures were relaxed until the force acting on each atom is smaller than 0.01 eV/Å and external pressure is smaller than 5 Kbar (0.5 GPa). The unit cells of all structures were kept cubic during the relaxation to avoid structure transformations from BCC to FCC which happens to a small amount of the selected structures. The spin-polarized DFT calculations were performed by VASP [Kresse and Furthmuller, 1996] with PAW pseudopotential [Blochl, 1994; Kresse and Joubert, 1999] within generalized gradient approximation (GGA) [Perdew *et al.*, 1996]. The energy cutoff was 350 eV and Monkhost-Pack scheme [Monkhorst and Pack, 1976] was used for Brillouin zone sampling.

To simulate the alnico magnets in a full manner, huge supercells containing millions of atoms are required in the lattice MC simulations as estimated from the length scale of the two phases mentioned above. Such MC simulations are not feasible under current model. Here we limited our model to describe the atomic structure crossing the boundary of the FeCo-rich and NiAl-rich phases. A supercell with the longest side along z direction and moderate widths in x and y directions should be able to capture the composition variation across the phase boundary between the FeCo-rich and NiAl-rich phases. We used a $6 \times 6 \times 80$ supercell of the smallest

BCC cell, which is about 1.8 nm × 1.8 nm × 23 nm in dimension and contains 5760 lattice sites. In the lattice MC simulations, Metropolis-Hastings algorithm [Metropolis and Ulam, 1949] is used to draw samples from the Boltzmann distribution, thus different temperatures can be introduced into the system.

3.3.3 Results and discussions

In the fitting of the cluster expansion coefficients, up to the 3rd nearest neighbor pair and triplet interactions and the smallest quadruplet interaction are considered. In Fig. 3.11, the formation energies of the reference structures calculated by the CE model are compared with the DFT calculations. We can see that the CE and DFT energies are very well correlated, in another word, the DFT energies of the reference structures were well reproduced by the CE model. The cross-validation score [van de Walle *et al.*, 2002a, 2009] in our fitting is ~ 13.8 meV/atom, indicating a decent predictive power of the obtained CE coefficients.
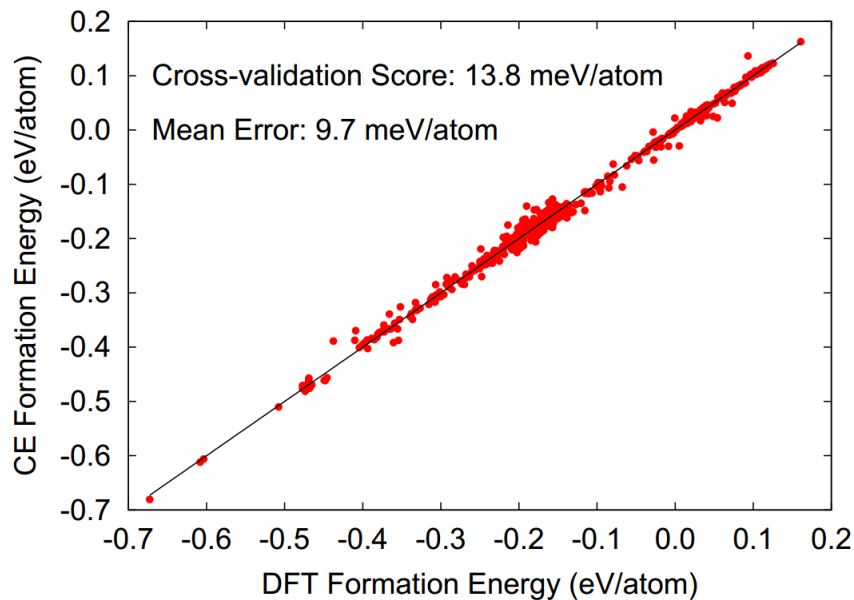
Figure 3.11 Correlation between the cluster expansion energies and DFT energies of the reference structures that were used in the fitting of alnico 5-7.

The composition of the sample used in our simulations was $Al_{0.17}Ni_{0.13}Co_{0.22}Fe_{0.48}$ based on experiment [Xing *et al.*, 2013; Zhou *et al.*, 2014], which corresponds to 979 Al atoms, 749 Ni atoms, 1267 Co atoms and 2765 Fe atoms in the simulation. We performed multiple MC simulations with different initial configurations at different temperatures ranging from 773 K to 2173 K. At each temperature, 5000 configurations from every independent MC simulation were collected and used for analysis after the corresponding sample reached equilibrium [Nguyen *et al.*, 2015]. The composition histograms at different temperatures, which were obtained by averaging over all the selected configurations, are plotted in Fig. 3.12. We can see that at the high temperature, such as the case of 1873 K plotted in Fig. 3.12(a), each element shows a Gaussian like distribution centering at its initial composition, indicating that the sample is homogenized at high temperature. While the temperature decreases to 1473 K, the shape of each peak except that of Co changes to asymmetric and the appearance of shoulders can be observed. After further decreasing the temperature to lower than 1100 K, the composition histograms of all elements separate into two distinct peaks, as shown in Fig. 3.12(c) and (d). Therefore, the phase decomposition into two different phases has happened in the sample at the temperature of 1073 K. The positions of the two peaks tell us the compositions of each element in the corresponding phases. Through analyses, we found that they are the FeCo-rich and AlNi-rich phases, as observed in the experiments.
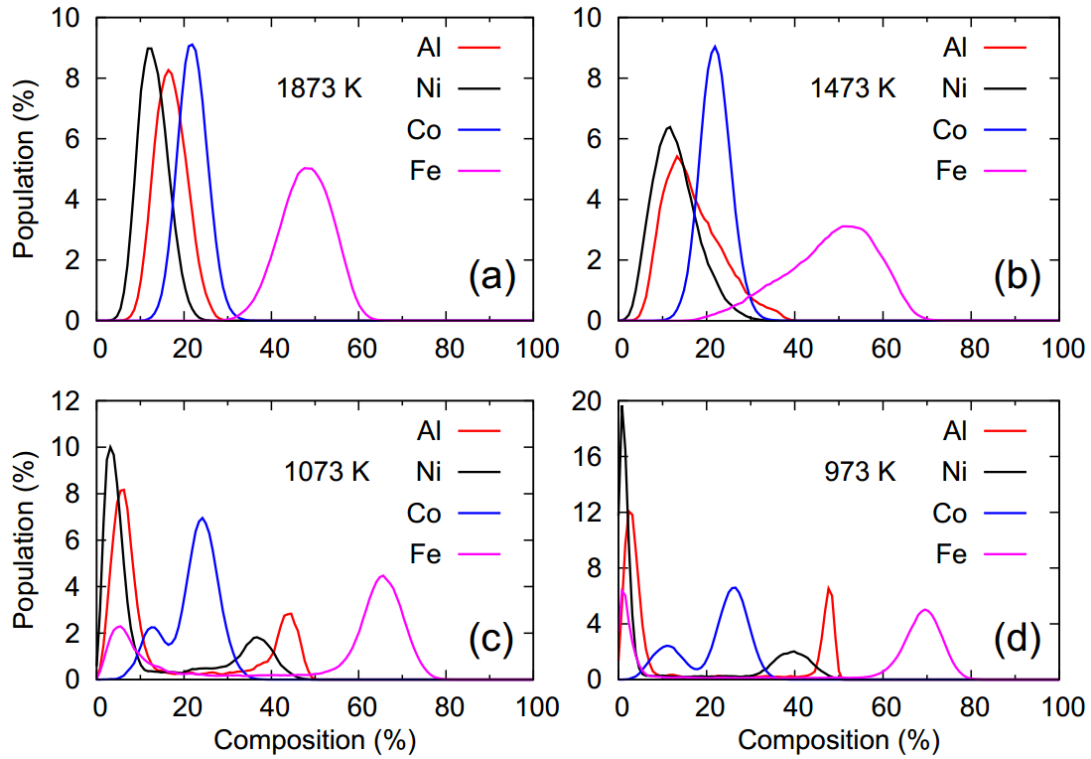
Figure 3.12 Composition histograms of alnico 5-7 from the lattice MC simulations at different temperatures.
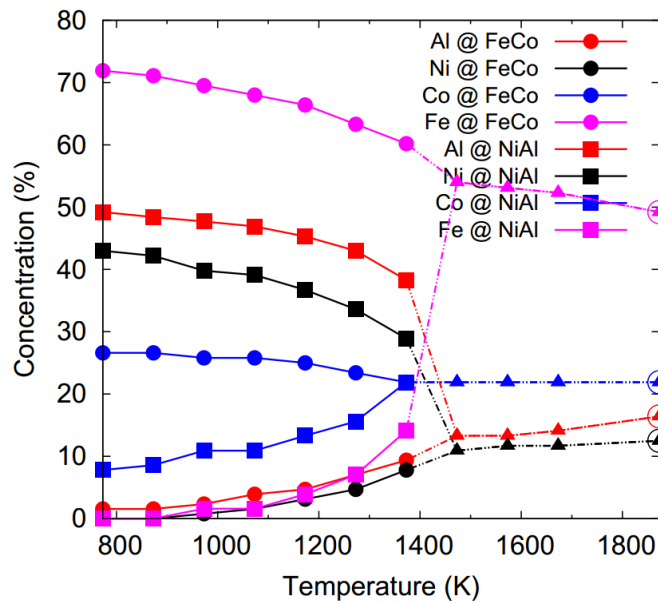
Figure 3.13 Compositions of the simulated FeCo-rich and NiAl-rich phases in alnico 5-7 as a function of temperature.

The details of the composition evolution in the MC simulations as a function of temperature are plotted in Fig. 3.13. The dash lines connecting the data points between 1873 K and 1373 K show the system is in transition from a homogenized phase to two separated phases. From the trend, we see that as the temperature decreases, the compositions of Fe and Co in the FeCo-rich phase, as well as the compositions of Ni and Al in the NiAl-rich phase become higher. At the lowest temperature in our simulations, i.e. 773 K, the percentage of Fe in NiAl-rich phase and Ni/Al in the FeCo-rich phase is as small as 2%. These results suggest that Fe or Ni/Al could be extracted almost completely out of the NiAl-rich or FeCo-rich phases. In contrast, the amount of Co left in the NiAl-rich phase is almost 10% at 773 K, indicating that Co cannot be easily extracted out of the NiAl-rich phase, which is consistent with the experimental observation [Xing *et al.*, 2013; Zhou *et al.*, 2014]. Practically, the high concentration of Co in the NiAl-rich phase is not preferred for two reasons. First, Co is relatively more expensive than the other elements and the remaining Co atoms in the non-magnetic NiAl-rich phase do not help the magnetic properties. Second, the NiAl-rich phase is expected to be non-magnetic, therefore serves as the separator for the FeCo-rich phases. The remained Co atoms in the NiAl-rich phase may introduce non-zero magnetic moment to it. The information we learnt from the simulations suggests that simply changing the annealing temperature and time may not help reduce the Co concentration in the NiAl-rich phase significantly.

By quantitatively comparing the compositions of each element in the two separated phases, we found consistent results between the simulation and experiment. For example, at 1273 K, the composition of the FeCo-rich phase in our simulation is $Al_7Ni_5Co_{24}Fe_{64}$, similar to that measured from experiment, $Al_5Ni_3Co_{25}Fe_{67}$ [Xing *et al.*, 2013; Zhou *et al.*, 2014]. We then studied the ordering in the FeCo-rich and NiAl-rich phases based on the samples obtained in the

simulations. Experimentally, Fe and Co are almost indistinguishable in X-ray scattering due to their similar scattering factors, which makes the determination of the ordering in the FeCo-rich phase very difficult. Here we calculated the neighbor correlation matrices to analyze the ordering in the NiAl-rich and FeCo-rich phases at different temperatures where the phase decomposition has already happened, i.e. from 773 K to 1273 K.

For the NiAl-rich phase at low temperature, there are almost no Al-Al, Al-Fe and Ni-Co nearest neighbors and a small fraction, ~5%, of Ni-Ni nearest neighbors, indicating that the NiAl-rich phase is in B2 ordering with Al/Fe on α-site and Ni/Co on β-site. The small fraction of Ni-Ni nearest neighbors could be attributed to anti-site defect at finite temperature. In the FeCo-rich phase, there are no Al-Al nearest neighbors and small amount of Al-Fe, Ni-Ni, Co-Co and Ni-Co nearest neighbors, indicating that the FeCo-rich phase also has B2 ordering, but with lower degree of order than that of the NiAl-rich phase. At higher temperature, the fractions of Al-Al, Al-Fe, Ni-Ni, Co-Co, and Ni-Co neighbors are increasing but still smaller than those obtained from a totally random alloy. Therefore, the B2 ordering in both the NiAl-rich and FeCo-rich phases is expected in the temperature range considered in our simulations. Quantitative analysis of the ordering in those two phases can be found in Ref. [Nguyen *et al.*, 2015].

Finally, we show the composition profile of alnico 5-7 at the temperature of 873 K and 1073 K along the z direction of the simulation model in Fig. 3.14, from which the boundary between the separated phases can be observed. The compositions of each element at a given z-value were calculated by averaging the local compositions over x and y directions. The phase decomposition of alnico 5-7 into the FeCo-rich and NiAl-rich phases can be seen clearly from Fig. 3.14. And for a wide range of temperatures from 773 to 1273 K (some are not plotted in Fig.

3.14), the boundaries between the FeCo-rich and NiAl-rich phases are quite sharp with a width

of about 2 nm. This is also consistent with experimental STEM EDS scan results, where sharp

phase boundaries were observed in alnico 5-7 [Xing *et al.*, 2013].
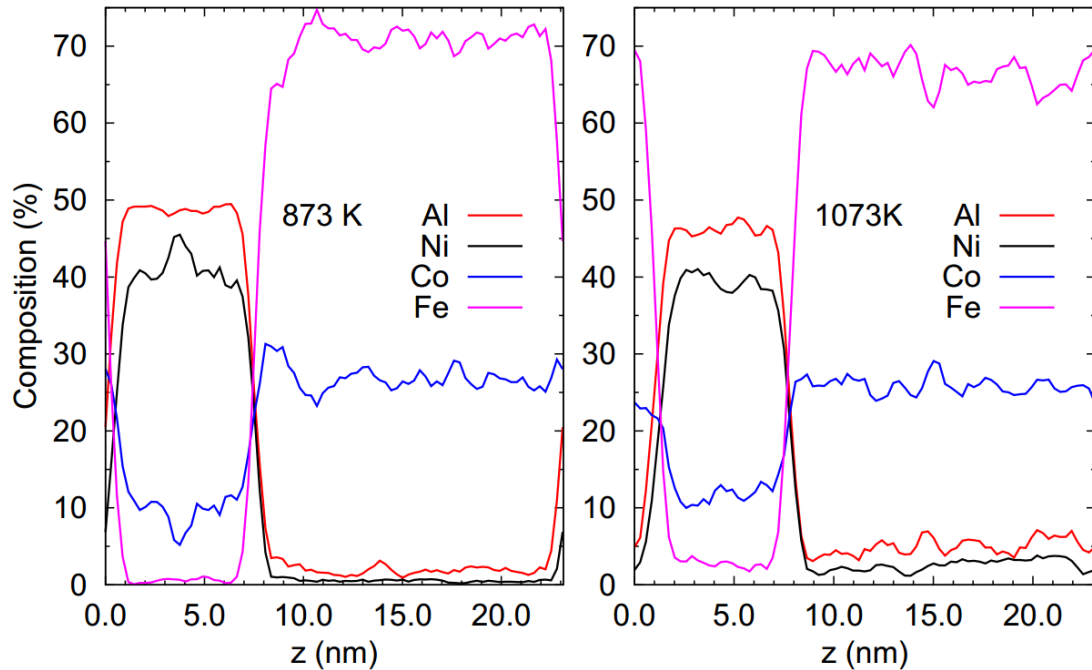
Figure 3.14 Composition profiles of the alnico 5-7 samples obtained from the lattice MC simulations along the decomposition direction (z) at the temperature of 873 K (left) and 1073 K (right).

3.3.4 Conclusions

In conclusion, we have fitted an accurate energy model for alnico 5-7 alloys containing

Al, Ni, Co and Fe using the Cluster Expansion method. Lattice MC simulations were performed

to study the structures of alnico 5-7 at atomic and nano scales as functions of temperatures. The

results showed that the CE model correctly describes the phase selections in alnico 5-7. Based on

analyses of the samples obtained from the MC simulations, we found the separation of Co is not

as complete as the other three elements, i.e. considerable amount of Co atoms exist in both the

FeCo-rich and NiAl-rich phases. We also studied the ordering in the two separated phases and

the grain boundaries between them. For a wide range of temperatures, the B2 ordering was observed in both the NiAl-rich phase and the FeCo-rich phase, although the degree of order in the FeCo-rich phase is lower than that in the NiAl-rich phase. The phase boundaries between the two phases were found to be very sharp and roles played by the sharp grain boundaries in improving the magnetic properties are to be investigated.

CHAPTER 4. NEW STABLE RE-B PHASES FOR ULTRA-HARD MATERIALS[4]

4.1 Abstract

As a distinct class of ultra-hard materials, transition metal borides are found to have superior mechanical properties that challenge the traditional materials. In this chapter, we explored the existence of new stable rhenium borides with different stoichiometries using genetic algorithm and first-principles calculations. Based on theoretical calculations, ReB in a *P*-3*m*1 structure is found to be stable against decomposition reactions below 10 GPa and ReB_3 in a *P*-6*m*2 structure is stable above 22 GPa. Two new phases of Re_2B are predicted to be thermodynamically stable at pressures higher than 55 GPa and 80 GPa respectively. We also show that a *C*2/*m* structure discovered for ReB_4 has energy lower than that of the *R*-3*m* structure reported earlier [Wang *et al.*, 2013]. Elastic and vibrational properties from first-principles calculations indicate that the low-energy structures obtained in our search are mechanically and dynamically stable and are promising targets as new ultra-hard materials.

4.2 Introduction

Transition metal (TM) borides have attracted considerable attentions due to their outstanding physical properties, such as superconductivity and extreme incompressibility. Among them, rhenium boride is one of the most studied. Re_3B, Re_7B_3 and ReB_2 have been synthesized experimentally [Telegus, 1969]. In addition to being superconductors [Strukova *et*

---

al., 2001; Kawano *et al.*, 2003], these compounds have been intensively investigated for potential applications as ultra-hard materials [Chung *et al.*, 2007; Dubrovinskaia *et al.*, 2007; Qin *et al.*, 2008; Juarez-Arellanoa *et al.*, 2013]. It was reported by Chung *et al.* that ReB_2 can be synthesized under ambient pressure with a hardness of 48 GPa, which makes it one of the hardest compounds on earth. However, the validity of these results was questioned [Dubrovinskaia *et al.*, 2007] and one of the later experiments [Qin *et al.*, 2008] showed that ReB_2 has a hardness of about 20 GPa and does not belong to the class of ultra-hard materials. Recently [Juarez-Arellanoa *et al.*, 2013], the hardness of Re_7B_3 and Re_3B has been measured experimentally. Re_7B_3 was found to be extremely incompressible with bulk modulus equal to 435(14) GPa, and the bulk modulus of Re_3B was also determined to be 320(15) GPa.

In addition to the three known phases, formation of new phases in Re-B system during the reaction of elemental rhenium and boron at high pressure and high temperature conditions has also been observed [Juarez-Arellanoa *et al.*, 2013]. At around 15 GPa and 1500K, extra reflections appeared in the powder x-ray diffraction pattern (XRD), which cannot be assigned to any previously reported Re-B phases, or to any boron phases. Therefore the extra peaks indicate the formation of a new phase, referred to as phase A in Ref. [Juarez-Arellanoa *et al.*, 2013]. After increasing the temperature to around 4000 K and pressure to around 22 GPa, another set of new reflections was observed and has been assigned to a second new phase, named phase B. Unit cell parameters and space groups of these two new phases have not been determined.

On the theoretical side, structures and elastic properties of rhenium borides with different boron concentrations have been studied [Gou *et al.*, 2009; Zhao *et al.*, 2010; Zang *et al.*, 2012]. Most of the previous theoretical studies are restricted to known prototype crystal structures. In order to obtain a more comprehensive understanding of the structures and properties of this

system, global searches for the crystal structures of Re-B system without any *a prior* assumption are necessary. We note that such global structure search has been performed for ReB_4 recently using a particle swarm optimization algorithm [Wang *et al.*, 2013]. An R-3m structure was found to be more stable than the earlier proposed WB_4-type structure [Zhao *et al.*, 2010].

In this chapter, we discuss our global structural searches for the stable phases in the Re-B system using GA and first-principles calculations. Four different rhenium borides are explored, with stoichiometry of Re_2B, ReB, ReB_3, and ReB_4 respectively. We found that the structures obtained from our GA search are energetically more favorable than those reported in the literature including the *R*-3*m* structure proposed for ReB_4 [Wang *et al.*, 2013]. Stability and mechanical properties of the predicted structures are investigated.

4.3   Computational Details

The genetic algorithm based on real space cut-and-paste operations [Deaven and Ho, 1995] is used to perform the crystal structure search. The searches were carried out at zero pressure, thus energy was used as the selection criteria for optimizing the candidate pool. In the beginning of the GA search, initial structures are generated randomly, without any assumption of their Bravais lattice type, atom basis or unit cell dimensions. Population size of the structure pool was set to be 64. In each generation, one quarter of the total population were updated through operations on the selected parent structures, such as crossover and mutation. Then the newly generated structures were locally optimized and their energies were evaluated by first-principles calculations. The search was done when the lowest-energy structure in the population pool remains unchanged in 300 consecutive generations in the present study. Finally, several lowest-energy structures survived in the pool were fully relaxed to identify the ground-state structure. In

the present work, up to 4 formula units were considered in the simulation cells for each composition.

First-principles calculations were carried out using spin-polarized density functional theory (DFT) [Kohn and Sham, 1969] within generalized-gradient approximation (GGA) with projector-augmented wave (PAW) method [Blochl, 1994; Kresse and Joubert, 1999] by VASP code [Kresse and Furthmuller, 1996]. The GGA exchange correlation functional parameterized by Perdew, Burke and Ernzerhof (PBE) [Perdew *et al.*, 1996] was used. Kinetic energy cutoff was set to be 400 eV. The Monkhorst-Pack's scheme [Monkhorst and Pack, 1976] was selected for Brillouin zone sampling with a k-point grid of $2\pi \times 0.033$ Å^{-1} during the structure searches. In the final structure refinements, a denser grid of $2\pi \times 0.02$ Å^{-1} was used and the ionic relaxations stop when the forces on all of the atoms are smaller than 0.01 eV/Å.

4.4   Results and Discussions

4.4.1 Structures

Lowest-energy structures of Re_2B, ReB, ReB_3, and ReB_4 obtained from the GA searches at zero pressure are plotted in Fig. 4.1 and the Wyckoff positions of each structure can be found in the figure caption. Lattice information, such as space group, lattice parameters and volume of unit cell, are listed in Table 4.1.
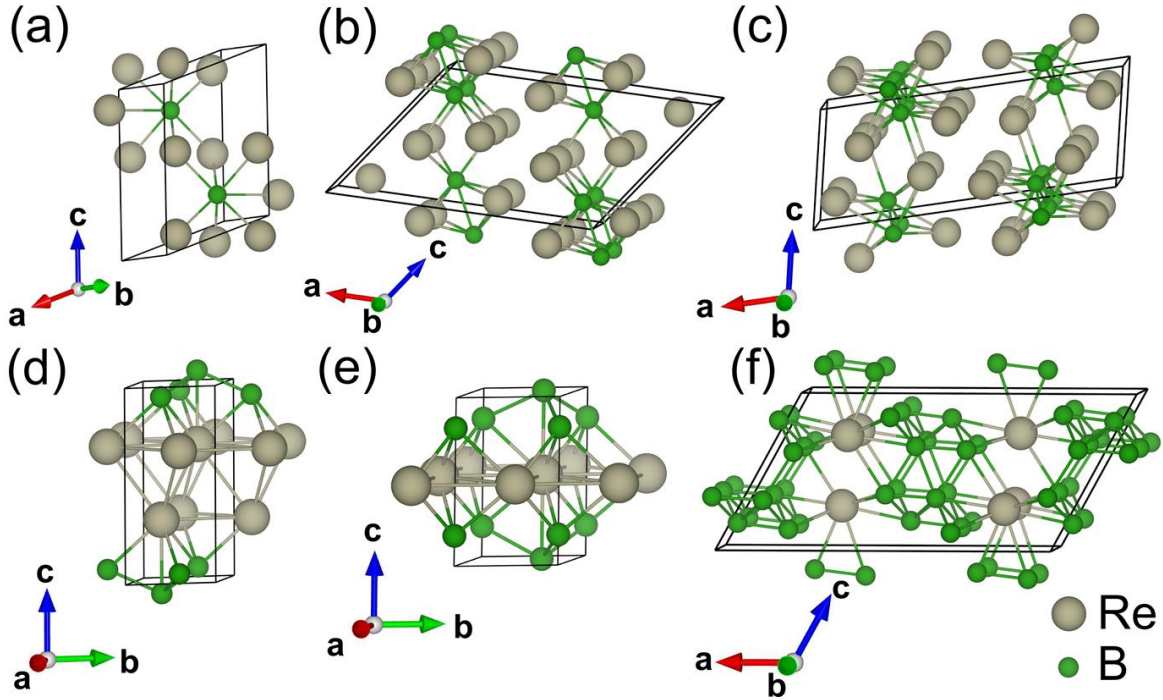
Figure 4.1 Low-energy structures for (a, b, c) Re_2B, (d) ReB, (e) ReB_3, (f) ReB_4 obtained from our GA searches. (a) $P2_1/m$: Re1 2e(0.2096, 1/4, 0.43425), Re2 2e(0.2025, 1/4, -0.0817), and B 2e(0.6099, 1/4, 0.7800); (b) $C2/m$: Re1 4i(0.8446, 0, 0.4247), Re2 4i(0.40457, 0, 0.1129), and B 4i(0.8836, 0, 0.8163); (c) $C2/m$: Re1 4i(0.0674, 0, 0.7869), Re2 4i(0.3522, 0, 0.6781), and B 4i(0.2676, 0, 0.1234); (d) P-3m1: Re 2d(1/3, 2/3, 0.6842) and B 2d(1/3, 2/3, 0.0596); (e) P-6m2: Re 1d(1/3, 2/3, 1/2), B1 2g(0, 0, 0.8191), and B2 1c(1/3, 2/3, 0); (f) $C2/m$: Re 4i(0.2069, 0, 0.2682), B1 4i(-0.0223, 0, 0.1744), B2 4i(0.4154, 0, 0.6420), B3 4i(0.5722, 0, 0.6639), and B4 4i(0.1839, 0, 0.8652).

Table 4.1 Lattice information of the crystal structures of Re_2B, ReB, ReB_3, and ReB_4 obtained in the current study. a, b, c: optimized lattice parameters; V: cell volume per formula unit.

Structure	Space group	a (Å)	b (Å)	c (Å)	V (Å^3)
Re_2B_#1	$P2_1/m$	4.45	2.93	5.92	36.43
Re_2B_#2	$C2/m$	9.79	2.85	6.32	35.35
Re_2B_#3	$C2/m$	11.21	2.89	4.44	35.15
ReB	P-3m1	2.88	2.88	5.93	21.26
ReB_3	P-6m2	2.92	2.92	4.59	34.01
ReB_4	$C2/m$	11.01	2.92	5.88	41.26

Re₂B: Three low-energy structures for Re_2B, labeled as _#1, _#2, and _#3 based on their energy order, are plotted in Fig. 4.1(a), (b), and (c) respectively. They all have monoclinic symmetry and all the boron atoms have 7-fold coordination with rhenium atoms. Apart from this, every boron atom in Re_2B_#2 bonds with another boron atom and every boron atom in Re_2B_#3 bonds with another two boron atoms. All three structures have lower energy than previously reported structures [Gou *et al.*, 2009; Zhao *et al.*, 2010].

ReB: For ReB, a trigonal structure with space group *P*-3*m*1 was found to be most stable, with much lower energy than the WC-type structure [Gou *et al.*, 2009; Zhao *et al.*, 2010]. As plotted in Fig. 4.1(d), the *P*-3*m*1 structure of ReB can be viewed as a layered structure with stacking of one buckled boron layer followed by two hexagonal Re layers along the c-axis.

ReB₃: For ReB_3, while all previous structure models have positive formation enthalpy, the lowest-energy structure obtained from our GA search has the formation energy very close to the tie-line of α-boron and ReB_2. It has a hexagonal structure with space group *P*-6*m*2 [Fig. 4.1(e)]. Boron and rhenium atoms form two types of hexagonal layers (boron layer is buckled, while rhenium layer is flat) and alternatively stack in the c direction. The layered feature of the ReB_3 structure, as well as that of the ReB structure is reminiscent of the crystal structures of some well-known superconducting materials, e.g. MgB_2 [Nagamatsu *et al.*, 2001], ReB_2 [Strukova *et al.*, 2001], etc.

ReB₄: The lowest-energy structure for ReB_4 obtained from our GA search is plotted in Fig. 4.1(f). This structure has *C*2/*m* symmetry and its energy is about 5 meV per atom lower than that of the *R*-3*m* structure reported earlier using a particle swarm optimization algorithm [Wang *et al.*, 2013]. This structure contains four formula units and each rhenium atom is coordinated by nine boron atoms. Different boron sites have different environments: site B1 (-0.0223, 0, 0.1744)

bonds with 2 rhenium atoms and 6 boron atoms; site B2 (0.4154, 0, 0.6420) bonds with 3 rhenium atoms and 4 boron atoms; site B3 (0.5722, 0, 0.6639) bonds with 1 rhenium atom and 7 boron atoms; site B4 (0.1839, 0, 0.8652) bonds with 3 rhenium atoms and 5 boron atoms.

4.4.2 Thermodynamic stability
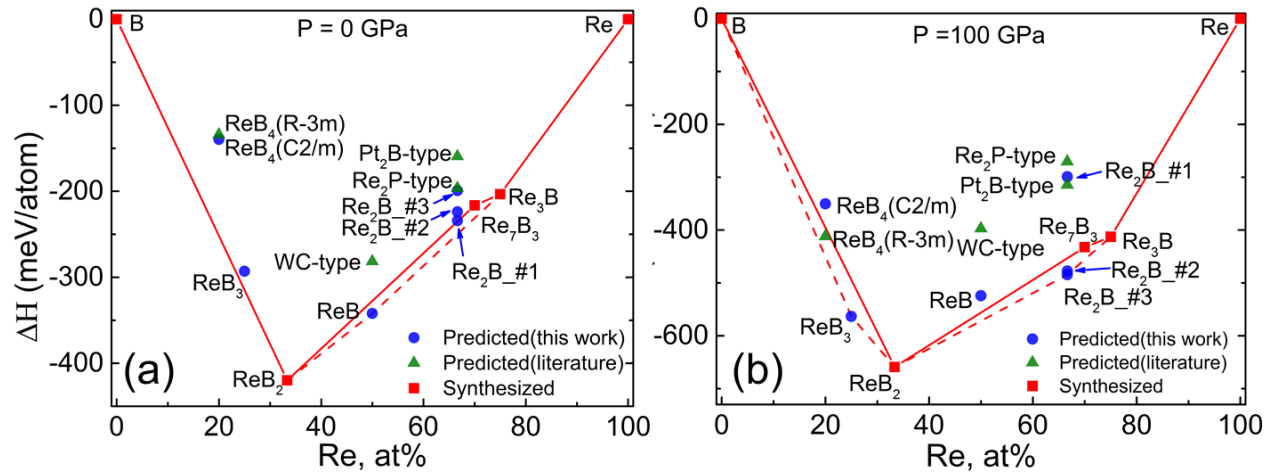
Figure 4.2 Convex hulls of the formation enthalpies in the Re-B system at the pressure of (a) 0 GPa, and (b) 100 GPa. The solid line connects the phases observed in experiments and the dash line represents the updated convex hull, including the results from our GA searches. Enthalpies of the structures from both this work and literatures are plotted, indicated by different symbols.

In order to access the stability of new structures obtained from our GA search, the convex hulls of formation enthalpies at $P = 0$ GPa and $P = 100$ GPa are plotted in Fig 4.2(a) and (b) respectively. Results of the new structures and those proposed in the literatures are indicated by circles and triangles respectively. The formation enthalpy is calculated by $\Delta H = [H(\text{Re}_m\text{B}_n) - m \cdot H(\text{Re}) - n \cdot H(\text{B})]/(m+n)$, where H, defined as $H = E + PV$, is the enthalpy of the corresponding alloys or elementary phases. For elemental boron, H was calculated based on the structure of α-boron [Will and Kiefer, 2001]. Once the hull of ground state energies of various structures is

constructed, the configurations with energy above the limiting boundary of the convex hull are considered to be unstable or metastable.

From Fig. 4.2(a), we can see that the ReB structure obtained from our GA search is below the tie-line of ReB_2 and Re_3B, indicating that ReB is a thermodynamically stable phase at zero pressure and zero temperature based on DFT calculations. For other new structures found from our present study, ReB_3 and Re_2B structures are very close to, but above the corresponding tie-lines and ReB_4 structure is far above the tie-line. Including the new stable ReB structure from our present study, the convex hull at zero pressure is updated as shown by the dashed lines in Fig. 4.2(a).

Since the relative stability of different phases can be altered at high pressures, we further studied the enthalpy-pressure relations of the structures obtained from our present study. As the pressure increases, the contribution from the *PV* term plays more important roles to the enthalpy. Therefore, the stability of structures with smaller volumes will surpass that of structures with larger volumes. Relative formation enthalpies vs. pressure for Re_2B, ReB, ReB_3, and ReB_4 are plotted in Fig. 4.3(a), (b), (c), and (d) respectively.

In Fig. 4.3(a), the relative enthalpies as the function of pressure of the three new Re_2B structures are compared with each other and with several possible decomposition pathways as indicated. From Table 4.1, we note that the volume of the $Re_2B\_\#1$ structure is the largest among the three new Re_2B structures, followed by those of $Re_2B\_\#2$ and $Re_2B\_\#3$. As a consequence, when the pressure is higher than 5 GPa, structure #2 becomes most stable among them and after ~ 80 GPa, structure #3 becomes most stable. Even considering the possible decompositions, such as $Re_2B \rightarrow 2Re + B$, and $Re_2B \rightarrow ReB_2 + Re_3B$, we found that $Re_2B\_\#2$ is still the most stable

structure when the pressure is between 55 and 80 GPa. When the pressure is above 80 GPa the

$Re_2B\_#3$ structures become more stable.
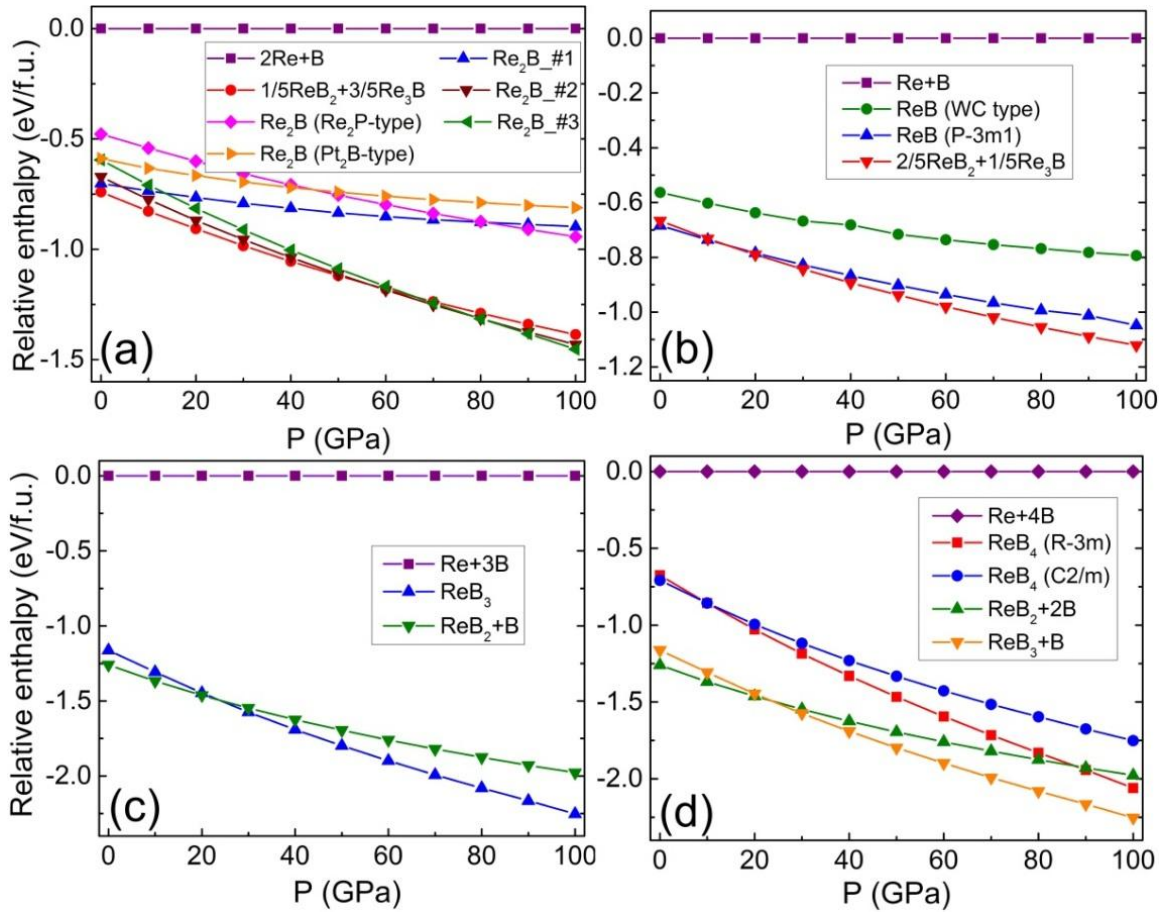
Figure 4.3 Relative enthalpies vs. pressure for (a) Re_2B, (b) ReB, (c) ReB_3 and (d) ReB_4. The competing phases with respect to possible initial reactants are compared in each figure.

ReB is stable against decomposition at zero pressure as shown in Fig. 4.2(a). However, as pressure exceeds 10 GPa, it becomes unstable towards decomposition into $ReB_2 + Re_3B$ as shown in Fig 4.3(b). At zero pressure, the ReB_3 structure from our present search lies above the tie line between ReB_2 and pure B phases. At around 22 GPa, our ReB_3 structure becomes more stable than ReB_2 + B as one can see from Fig 4.3(c).

From DFT calculations, the R-3m structure of ReB_4 has a volume of 40.73 Å^3, smaller than that of the $C2/m$ structure. Around 8 GPa, the R-$3m$ structure outperforms the $C2/m$ structure. It also wins against the decomposition into ReB_2 and B after ~ 88 GPa, consistent with previous report [Wang *et al.*, 2013]. However, in the pressure range from zero up to 100 GPa, enthalpies of both ReB_4 structures are much higher than that of ReB_3 + B as shown in Fig. 4.4(d), therefore, ReB_4 will decompose into the pure boron and ReB_3 phase.

From above discussions, we can see that the phase stability in Re-B system changes substantially with pressure. Taking the structures found in our search into consideration, a more comprehensive convex hull for the Re-B system at P = 100 GPa, with respect to the stable phases ReB_3, ReB_2, Re_2B, and Re_3B, is constructed in Fig 4.2(b).

In Fig. 4.4, we plotted the relative stability of the three Re_2B structures, ReB_2+Re_3B and Re_7B_3 at high pressure in more details. From Fig 4.4(a), we can see clearly that the $Re_2B\_\#2$ and $Re_2B\_\#3$ structures are the most stable structures when the pressure is higher than 55 GPa. In Fig. 4.4(b), we plotted the enthalpies of possible decomposition reactions of Re_7B_3 with respect to that of the parent compound. At low pressure, ReB_2+Re_3B is most table. Above 55 GPa, Re_2B+Re_3B becomes more stable. There is another transition from $Re_2B\_\#2+Re_3B$ to $Re_2B\_\#3+Re_3B$ around 80 GPa which is related to the phase transitions in Re_2B as discussed above. Since the Re_7B_3 phase is always above the tie-line of ReB_2 and Re_3B, and above the tie-line of Re_2B and Re_3B, we can tentatively identified the $Re_2B\_\#2$ and $Re_2B\_\#3$ structures as the candidates for the two new phases, i.e. phase A and B, discovered in recent synthesis experiments [Juarez-Arellanoa *et al.*, 2013] under high pressures and high temperatures. The transition pressures from our calculation at T = 0 K, 55 GPa and 80 GPa, are higher than the

observed experimental pressures. The discrepancy may be expected because temperature effects are not included in the theoretical calculations.
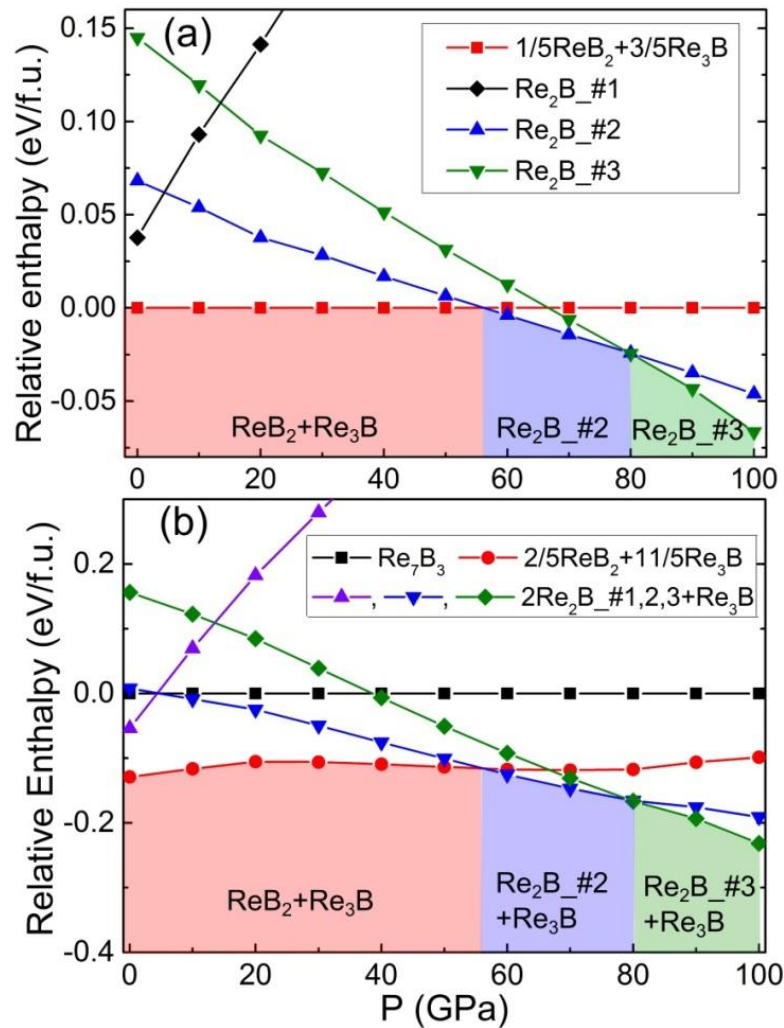
Figure 4.4 (a) Relative enthalpies of three Re_2B structures and the decomposition reaction: $Re_2B \rightarrow ReB_2 + Re_3B$. (b) Relative enthalpies of Re_7B_3 and possible decomposition reactions: $Re_7B_3 \rightarrow ReB_2 + Re_3B$, $Re_7B_3 \rightarrow Re_2B + Re_3B$. Different pressure ranges are highlighted and labeled corresponding to different ground states.

4.4.3 Elastic properties

To study the mechanical properties of the newly discovered structures, elastic constants were calculated using VASP package [Page and Saxe, 2002; Wu *et al.*, 2005]. The elastic tensor is determined by performing six finite distortions of the lattice and deriving the elastic constants from the strain-stress relationship [Page and Saxe, 2002]. Bulk modulus B and shear modulus G were estimated using the Voigt-Reuss-Hill approximation [Hill, 1952]. Furthermore, the Young's modulus Y and Poisson's ratio v were calculated by: $Y = (9GB)/(3B+G)$ and $v = (3B-2G)/(6B+2G)$. The results for Re_3B, Re_7B_3, Re_2B (#1, #2, #3), ReB, ReB_2, ReB_3 and ReB_4 ($C2/m$ structure) are listed in Table 4.2. The calculated elastic constants suggest that all the structures in Table 4.2, including the new structures obtained in this work, are mechanically stable, as they satisfy the mechansical stability criteria [Wu *et al.*, 2007].

Table 4.2 Calculated elastic constants (in GPa), bulk modulus B (in GPa), shear modulus G (in GPa), B/G raito, Young's modulus Y (in GPa) and Poisson's ratio v of various rhenium borides.

Structure	$c11$	$c22$	$c33$	$c12$	$c13$	$c23$	$c44$	$c55$	$c66$	B	G	B/G	Y	v
Re_3B	627	607	567	266	269	294	24	249	233	420	123	3.41	337	0.37
Re_7B_3	603		590	268	273		133		169	380	151	2.50	402	0.32
Re_2B_#1	587	562	686	279	270	240	199	219	199	378	188	2.01	483	0.29
Re_2B_#2	627	670	733	257	268	235	265	176	203	393	210	1.87	535	0.27
Re_2B_#3	558	679	621	277	354	214	239	182	254	394	192	2.05	496	0.29
ReB	618		915	218	171		248		205	360	243	1.48	596	0.22
ReB_2	642		1032	168	131		262		245	347	276	1.26	654	0.19
ReB_3	575		911	140	181		223		220	332	235	1.41	570	0.21
ReB_4[*]	928	597	615	148	95	85	183	180	248	303	234	1.29	558	0.19

[*] $C2/m$ structure is used for the calculation.

The highest bulk modulus is found in the Re_3B phase, about 420 GPa, and the highest shear modulus is found in the ReB_2 phase, about 276 GPa. As indicators for hardness, shear modulus is believed to be better than bulk modulus [Pugh, 1954]. Based on shear modulus, ReB_2 is still the hardest among all the compositions considered in Table 4.2. ReB and ReB_3 also have very high shear modulus, and at the same time have higher bulk modulus than ReB_2, which makes them potentially ultra-hard materials. Comparing the hardness of Re_7B_3 and the new Re_2B phase, we note that structures of Re_2B have higher B, G, and Y. Therefore, Re_2B is expected to be harder than Re_7B_3.

Considering the whole composition range, it is easy to notice that the B-rich phases and the Re-rich phases have much difference in the mechanical properties. Poisson's ratio v of rhenium borides with B% $\geq$ 50% is smaller than those with B% < 50%, as well as the bulk modulus. On the other hand, the shear modulus and Young's modulus of rhenium borides with B% $\geq$ 50% are larger than those with B% < 50%. It is known that B/G ratio is related to brittleness (ductility) and the critical value is about 1.75 [Haines *et al.*, 2001]. For rhenium borides with boron composition smaller than 50%, the calculated B/G ratios are bigger than 1.75, suggesting that they are ductile. Other rhenium borides, i.e. with B% $\geq$ 50%, have B/G values smaller than 1.75, suggesting that they are brittle. The structural change from ductile to brittle is due to the fact that higher boron composition induces more covalent bonds.
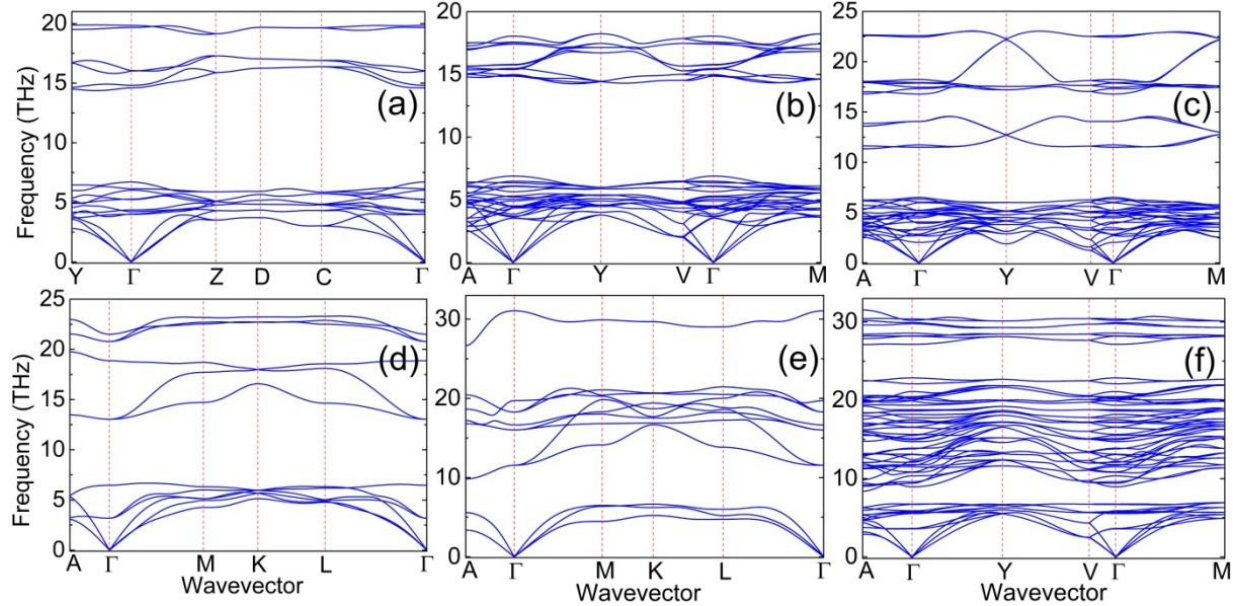
Figure 4.5 Phonon dispersion relations of the structures obtained from our GA search: (a) Re$_2$B_#1, (b) Re$_2$B_#2, (c) Re$_2$B_#3, (d) ReB, (e) ReB$_3$ and (f) ReB$_4$.

Phonon dispersion relations were also calculated for the newly found structures to check their dynamical stability. The calculation was performed within harmonic approximation using a supercell approach and the *Phonopy* code [Togo *et al.*, 2008]. Supercell with each lattice parameter larger than 10 Å was used to do the calculation. Finite atomic displacements are created from the unit cell considering crystal symmetry, whose amplitude is 0.01 Å. The results of the new structures, plotted in Fig 4.5, showed no imaginary phonon frequency in the whole Brillouin zone, indicating that in addition to being mechanically stable, all the presented structures are dynamically stable.

Finally, in Fig. 4.6, we provide simulated XRD spectra for the lowest-energy structures of the newly predicted stable phases. The simulation used Cu Kα radiation with $\lambda = 1.5406$ Å.
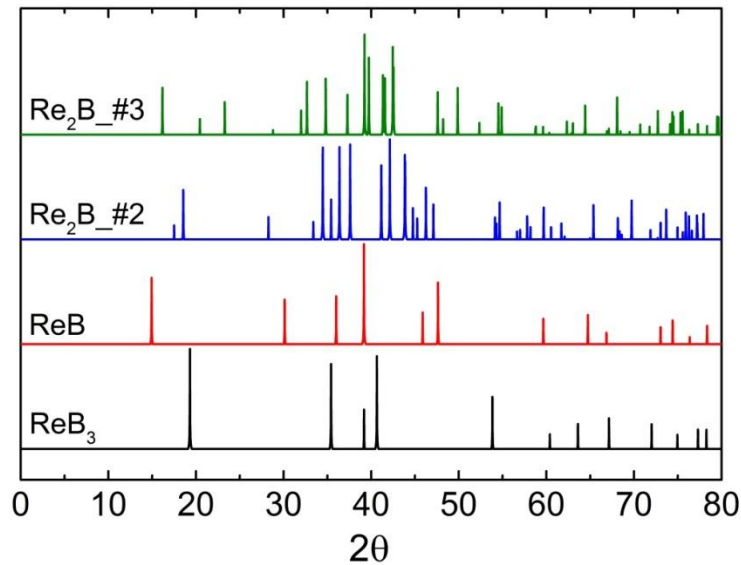
Figure 4.6 Simulated X-ray diffraction spectra of the predicted stable phases (ReB$_3$, ReB, Re$_2$B_#2 and Re$_2$B_#3) with Cu Kα radiation with $\lambda = 1.5406$ Å.

4.5 Conclusions

To summarize, we predict that ReB is a stable phase at zero pressure and ReB$_3$ is a stable phase above 22 GPa. Re$_2$B goes through two phase transitions with increasing pressure and the Re$_2$B_#2 and Re$_2$B_#3 structures found from our search are shown to be stable against decompositions. Meanwhile, the R-$3m$ structure reported earlier for ReB$_4$ was found to have higher energy than a $C2/m$ structure at zero pressure. Elastic properties calculations indicate that B-rich and Re-rich compounds show clear difference in mechanical properties and the newly discovered stable phases of ReB and ReB$_3$ are extremely incompressible. Under the guidance of the theoretical predictions, new compounds in the Re-B system could be synthesized in experiments and the stability of the predicted phases and their mechanical properties presented in this work can be verified.

CHAPTER 5.   INTERFACE STRUCTURE PREDICTION FROM FIRST-PRINCIPLES[5]

5.1   Abstract

Information about the atomic structures at solid-solid interfaces is crucial for understanding and predicting the performance of materials. Due to the complexity of the interfaces, it is very challenging to resolve their atomic structures using either experimental techniques or computer simulations. In this chapter, we present an efficient first-principles computational method for interface structure prediction based on the adaptive genetic algorithm. This approach significantly reduces the computational cost, while retaining the accuracy of first-principles prediction. The method is applied to the investigation of both stoichiometric and non-stoichiometric $SrTiO_3$ $\Sigma3(112)[\bar{1}10]$ grain boundaries with unit cell containing up to 200 atoms. Several novel low-energy structures are discovered, which provide fresh insights into the structure and stability of the grain boundaries.

5.2   Introduction

Solid-solid interfaces and grain boundaries (GBs) usually exhibit structure reconstructions within nanometer scale that are different from their corresponding bulk structures. These nanoscale structure reconstructions play a crucial role in determining the performance metrics of materials, such as mechanical strength or ductility, electrical transport, magnetic properties, etc. [Hilgenkamp and Mannhart, 2002; Robertson, 2006; Dillon *et al.*, 2007;

Luth, 2010] The urgent demand for new technologies has put great pressure on the development of efficient methods for fast predicting complex GB and interface structures to aid materials discovery and design. Although the recent development in experimental techniques such as high resolution transmission electron microscopy (HRTEM) has made the atomic-scale investigation of GBs and interfaces possible [Zhang *et al.*, 2003], detailed characterization also relies heavily on theory and simulation to interpret the data, because point defects and chemistry of the atoms are not easy to be identified by HRTEM.

During the last 10 years, there has been considerable progress in predicting the crystal structures using advanced computational algorithms and modern computers as discussed in Chapter 1. However, much less work on GB and interface structure prediction has been reported [van Alfthan *et al.*, 2006; Peacock *et al.*, 2006; Zhang *et al.*, 2009; Xiang *et al.*, 2009; Chua *et al.*, 2010; Feng *et al.*, 2012; Hellberg *et al.*, 2012]. Due to the complexity of the GB and interface problem, which requires large number of atoms in the simulation, it is not feasible to perform straightforward structure searches using accurate quantum mechanics methods (e.g. first-principles density functional theory). Most of the interface structure searches so far were carried out either using classical interatomic potentials [van Alfthan *et al.*, 2006; Zhang *et al.*, 2009; Chua *et al.*, 2010; Feng *et al.*, 2012] or under the assumption of simplified coherent interfaces [Peacock *et al.*, 2006; Xiang *et al.*, 2009; Feng *et al.*, 2012; Hellberg *et al.*, 2012].

In this chapter, we present a generic and accurate computational approach to study the atomic structures of GBs and interfaces based on AGA [Wu *et al.*, 2014], which has been described in greater detail in Chapter 2. AGA combines fast structure exploration using auxiliary classical potentials with accurate energy evaluation using first-principles calculations in an iterative way, so that it can speed up the search process by at least 10^3 times and at the same time

maintains the accuracy of first-principles calculations. The efficiency and accuracy of the AGA method makes it possible to tackle the complex problems of GB and interface structure predictions within available computing capability.

We demonstrate the power of AGA by predicting the structures of SrTiO$_3$ Σ3(112)[$\overline{1}$10] symmetrical tilt GB, which has been attracting a lot of attentions recently [Benedek *et al.*, 2008; Chua *et al.*, 2010; Dudeck *et al.*, 2010], due to the broad applications of SrTiO$_3$ in many oxide-based electrical and electronic devices. Benedek *et al.* predicted two low-energy structures for the stoichiometric Σ3(112)[$\overline{1}$10] GB by first-principles DFT calculations. One is SrTiO-terminated with mirror symmetry at the interface and no translation between the top and bottom bulk parts, while the other is O$_2$-terminated with mirror-glide symmetry. Although the energies of these two structures are very similar in DFT calculations, the structure with mirror symmetry gives a better agreement with experimental observation by quantitative HRTEM analysis [Dudeck *et al.*, 2010]. Non-stoichiometric Σ3(112)[$\overline{1}$10] GB of SrTiO$_3$ system was investigated by Chua *et al.* using genetic algorithm with empirical interatomic potentials, followed by structure refinement using DFT calculations. A structure with $\Gamma_{TiO_2} = N_{TiO_2} - N_{SrO} = 2$ (refer to as *Γ2-lit* in the rest of this paper) was shown to be slightly more stable than the stoichiometric GBs within a very narrow chemical potential range. These previous studies provide the bases for benchmarking and evaluating the performance of our AGA approach. We performed structural searches for this grain boundary with the number of atoms in the unit cell ranging from 90 to 200. The AGA searches not only reproduced the low-energy stoichiometric Σ3(112)[$\overline{1}$10] GB structures, but also revealed several new structures for the non-stoichiometric GBs with different

excesses and provided a more comprehensive picture about the stability of $SrTiO_3$ $\Sigma3(112)[\bar{1}10]$ grain boundary.

5.3 Methods

To search for interface structures, the real space cut-and-paste operation [Deaven and Ho, 1995] is employed to generate the offspring in AGA. In this approach, the interface is represented by a slab, which is divided into four parts as schematically plotted in Fig 5.1. All the atoms in fixed-bulk part at the bottom of the slab are not allowed to move. During the local optimization step in the GA search, the atoms at the interface region are fully relaxed, while the atoms in the rigid-bulk part above the interface can only move as a whole by rigid-body translations with respect to the fixed-bulk part. A vector $\vec{v}$ is used to describe the movement of the rigid-bulk part relative to the fixed-bulk part during the local optimization. A vacuum region (usually larger than 20Å) is added above the slab in the simulation in order to avoid the interactions between the top and bottom surfaces of the slab when period boundary conditions are applied. During the mating process, a pair of parent structures is selected from the population pool and the offspring is generated through the cut-and-paste operation on the interface regions (Fig. 5.1). The probability for a structure being selected as a parent depends on the energy order of the structure in the pool and follows a Gaussian distribution, which is defined with the lowest-energy structure as the expectation and one quarter of the pool size as the standard deviation. The offspring structures retain their chemical composition the same as the parent structures. The rigid translation vector $\vec{v}$ between the top and bottom bulk portions from the lower-energy parent is passed on to the offspring, i.e. the offspring will inherit $\vec{v}$ from the "stronger" parent.
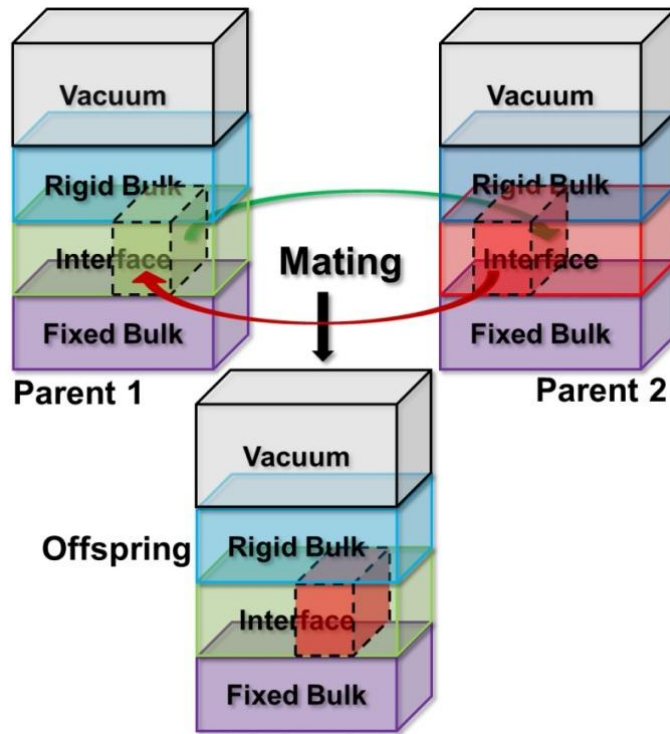
Figure 5.1   Schematic representation of the interface model and mating operation in our adaptive genetic algorithm. Four parts are included in the model: fixed bulk where all atoms are fixed; interface where atom positions are to be optimized; rigid bulk which can move as a rigid body relative to the fixed bulk during the search; and a vacuum region to avoid interactions between the two surfaces of the slab. During the mating process, part of the parent structures as indicated by the dashed cuboids will be exchanged to generate the offspring structure.

To perform the AGA search for the $SrTiO_3$ GB structures, classical potentials in the EAM formalism [Daw and Baskes, 1984] were used. Morse functions (Eq. 5.1) were used to describe the pair interactions (Sr-Sr, Sr-Ti, Sr-O, Ti-Ti, Ti-O, and O-O) in the EAM potentials with 3 fitting parameters each (D, α, r_0). Exponential decaying function (Eq. 5.2) with 2 adjustable parameters (α, β) was used as the density function for each element, and the form proposed by Banerjea and Smith (Eq. 5.3) was used as the embedding function, which also has 2 adjustable parameters (F_0, γ). Total adjustable parameters are 30.

$$\phi(r_{ij}) = D\left[e^{-2\alpha(r_{ij}-r_0)} - 2e^{-\alpha(r_{ij}-r_0)}\right] \tag{5.1}$$

$$\rho(r_{ij}) = \alpha \exp\left[-\beta(r_{ij} - r_0)\right] \tag{5.2}$$

$$F(n) = F_0[1 - \gamma \ln n]n^{\gamma} \tag{5.3}$$

The total energy of the system then has the following form:

$$E_{total} = \frac{1}{2} \sum_{i,j(i\neq j)}^{N} \phi_{ij}(r_{ij}) + \sum_{i} F_i(n_i) \tag{5.4}$$

Where r_{ij} is the distance between atoms i and j, $n_i = \sum_{j\neq i} \rho_j(r_{ij})$ is the electron density at the site occupied by atom i.

Our first-principles calculations were carried out within the local density approximation (LDA) [Perdew and Zunger, 1981] to DFT as implemented in VASP package [Kresse and Furthmuller, 1996]. Plane wave energy cutoff was 520 eV. During the final DFT refinement after finishing the AGA search, the slab model is transferred to a supercell model, with two equivalent GBs and no vacuum region. All atoms in the supercell model are fully relaxed by DFT. Big enough bulk regions are used to separate the two GBs so that there is no interaction between them and the interfacial energy from such a calculation is converged. For example, when the length of the bulk region separating the two interfaces changes from 12 Å to 24 Å, the change in interfacial energy is found to be less than 0.02 J·m^{-2}.

Here, SrTiO$_3$ is treated as a pseudo-binary system of binary oxides SrO and TiO$_2$ with chemical potentials μ_{SrO} and μ_{TiO_2} respectively. The stoichiometry is described in terms of interfacial excesses. In the present work, the excess of component TiO$_2$ with respect to SrO is defined as $\Gamma_{TiO_2} = N_{TiO_2} - N_{SrO}$ following Ref. [Chua *et al.*, 2010]. In our calculation, we

approximate the Gibbs free energy as the total energy from DFT calculation at 0 K. The interfacial excess free energy is defined as:

$$\sigma = \frac{1}{2A_S}(G - N_{SrO}\mu_{SrO} - N_{TiO_2}\mu_{TiO_2}) \tag{5.5}$$

where G is the energy of the supercell, N_{SrO} and N_{TiO_2} are the numbers of formula units of SrO and TiO_2 in the supercell, and $2A_S$ is the area of the two equivalent interfaces in the supercell. The chemical potentials μ_{SrO} and μ_{TiO_2} are chosen to lie within certain bounds at standard temperatures and pressures: $\mu_{SrO} = g_{SrO}^0 + (1 - \lambda)\Delta G_{f,SrTiO_3}^0$, and $\mu_{TiO_2} = g_{TiO_2}^0 + \lambda\Delta G_{f,SrTiO_3}^0$, where $0 \leq \lambda \leq 1$ and g_{SrO}^0, $g_{TiO_2}^0$ are the energies per formula unit of the bulk SrO (in rock-salt structure) and TiO_2 (in rutile structure), respectively. $\Delta G_{f,SrTiO_3}^0$ is the formation energy of $SrTiO_3$ per formula unit from component binary oxides SrO and TiO_2. When $\lambda = 0(1)$, bulk phases of $SrTiO_3$ and $TiO_2(SrO)$ coexist.

Our calculated result for $\Delta G_{f,SrTiO_3}^0$ at $T = 0$ K is listed together with the literature data in Table 5.1. VASP calculation gives $\Delta G_{f,SrTiO_3}^0 = -1.398\ eV$, which is about 0.1 eV higher than the value obtained using CASTEP package [Chua *et al.*, 2010]. From the comparison, we can see that the energy obtained in the present work from VASP calculation is closer to the experimental data, although the results from difference between different experiments are somewhat different.

Table 5.1 Comparison of the formation energy of $SrTiO_3$ per formula unit from constituent binary oxides SrO and TiO_2, i.e. $\Delta G^0_{f,SrTiO_3}$, between theoretical calculations and experimental measurements at $T = 0$ K.

	In eV/f.u.	In kJ/mol
VASP	−1.398	−134.9 [This work]
CASTEP	−1.501	−144.8 [Chua *et al.*, 2010]
Experiment	-	−121.9 [Jacob and Rajitha, 2011]
	-	−137.7 [Knacke *et al.*, 1991]

5.4   Results and discussions

5.4.1   Validation

Before applying AGA, we first evaluated the performance of the mating operation for interface structure prediction shown in Fig. 5.1. Using the classical potentials for $SrTiO_3$ from Ref. [Benedek *et al.*, 2008], we searched for several known structures, i.e., bulk $SrTiO_3$, stoichiometric $\Sigma3(111)[\bar{1}10]$ and $\Sigma3(112)[\bar{1}10]$ GBs, with only chemical composition as input. When the orientation of the rigid-bulk part is set to be same as the fixed-bulk part (i.e., without tilting), the search successfully recovered the bulk $SrTiO_3$ structure, as expected. For the stoichiometric cases, the SrO_3-terminated structure with mirror-symmetry was found to be most stable for the $\Sigma3(111)[\bar{1}10]$ GB, and both the SrTiO-terminated structure with mirror-symmetry and the O_2-terminated structure with mirror-glide symmetry were obtained for the $\Sigma3(112)[\bar{1}10]$ GB, consistent with previous studies. Furthermore, using the same Buckingham potential as in Ref. [Chua *et al.*, 2010] and including 6 atoms (2 Ti atoms and 4 O atoms) in the interface region, the *Γ2-lit* structure for the non-stoichiometric $\Gamma_{TiO_2} = 2$ GB were successfully reproduced within 5 generations of our GA search. When the number of atoms in the interface

region was increased, several structures with energies much lower than that of the *Γ2-lit* structure were found under the same classical potential. However, these structures are not energetically more favorable in DFT calculations. The results suggest that our interface structure search scheme is efficient and robust, but the classical potentials from the literature are not accurate and transferable to describe various grain boundaries in SrTiO$_3$.

5.4.2 AGA searches
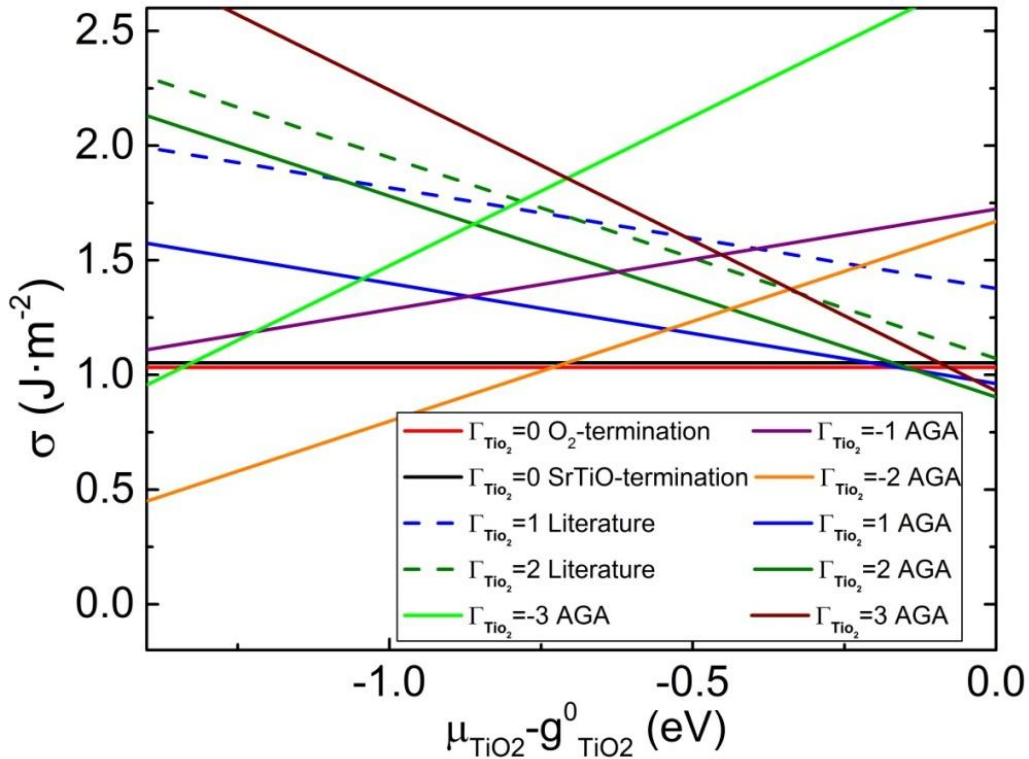
Figure 5.2 Grain boundary free energies as a function of μ_{TiO_2} for the $\Sigma3(112)[\bar{1}10]$ system. The dashed lines represent structures reported in the literature [Chua *et al.*, 2010] with excess equal to 1 and 2, and the solid lines represent the structures obtained from AGA searches with different excesses. σ, μ_{TiO_2} and $g^0_{TiO_2}$ are the interfacial excess free energy, chemical potential of TiO$_2$ and free energy of bulk TiO$_2$ respectively, as defined in the methods section.

The problem discussed above encountered by classical potentials can be overcome by the AGA method. To demonstrate this point, we performed structure searches for the $\Sigma3(112)[\overline{1}10]$ GBs with Γ_{TiO_2} between -3 and +3 using AGA. In the stoichiometric case, i.e. $\Gamma_{TiO_2} = 0$, the most stable structure from the AGA search is the O_2-terminated mirror-glide symmetric structure, which is about 0.02 J·m^{-2} lower than the SrTiO-terminated mirror symmetric structure, consistent with the results obtained using classical potential. However, for the non-stoichiometric GBs, the AGA searches revealed several new structures that are missed in previous studies. These new structures are stable over a wide range of the chemical potentials, as plotted in Fig. 5.2.

The lowest-energy structures obtained from AGA search for all the three positive Γ_{TiO_2} (= 1, 2, 3) cases are more stable than the stoichiometric ones when the chemical potential of TiO_2 is taken to be close to the bulk cohesive energy of TiO_2 (i.e. λ is close to 0, see the methods section). When $\lambda = 0$, the interfacial excess free energy σ of the lowest-energy structure for $\Gamma_{TiO_2} = 1$ from AGA search is about 0.12 J·m^{-2} lower than that of the stoichiometric GB and about 0.4 J·m^{-2} lower than that of the structure proposed in the literature [Chua *et al.*, 2010]. The lowest-energy structure with $\Gamma_{TiO_2} = 2$ from AGA search is about 0.17 J·m^{-2} lower in σ than the Γ2-*lit* structure and 0.13 Jm^{-2} lower than the stoichiometric GB. For $\Gamma_{TiO_2} = 3$, the lowest-energy structure from AGA search is about 0.11 J·m^{-2} lower in σ than the stoichiometric GB. We noticed that as the chemical potential of TiO_2 is very close to the cohesive energy of bulk TiO_2, Γ2-*lit* has slightly higher energy than that of the stoichiometric GB structures, while the calculation in Ref. [Chua *et al.*, 2010] showed that Γ2-*lit* structure is energetically more favorable. This small discrepancy could be due to the different setups in the DFT calculations.

Because the energy difference from the two DFT calculations is very small, it will not affect the

conclusion that the new structures found from our AGA search are more stable.
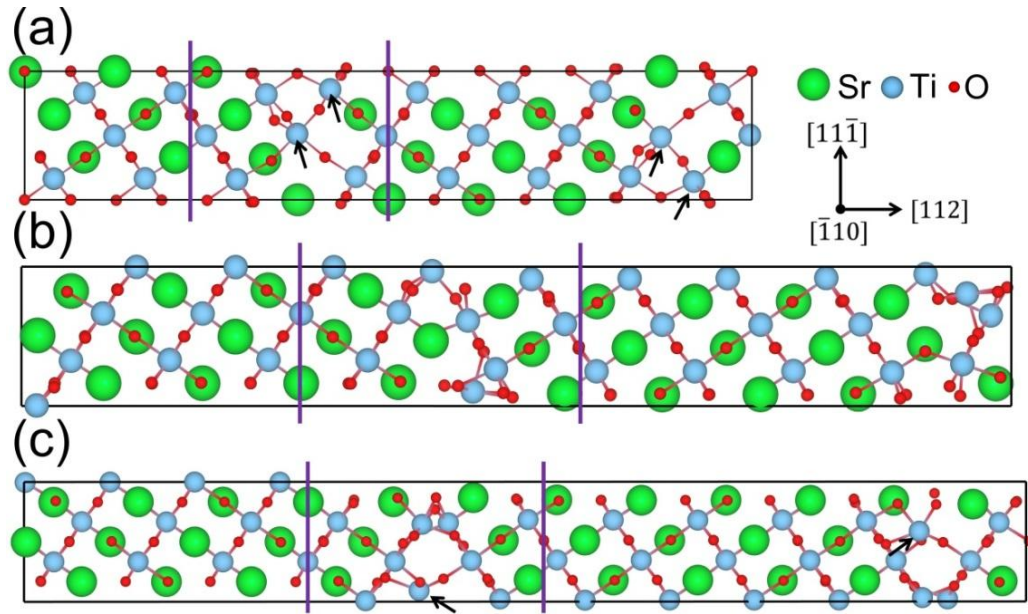
Figure 5.3 New grain boundary structures for positive Γ_{TiO_2}. (a) $\Gamma_{TiO_2} = 1$ $\Sigma3(112)[\bar{1}10]$ grain boundary; (b) $\Gamma_{TiO_2} = 2$ $\Sigma3(112)[\bar{1}10]$ grain boundary; (c) $\Gamma_{TiO_2} = 3$ $\Sigma3(112)[\bar{1}10]$ grain boundary. The black arrows point to the Ti atoms with coordination number 5 and the purple vertical lines indicate one of the two equivalent grain boundary regions.

The lowest-energy structures for $\Gamma_{TiO_2} = 1$, 2, 3 obtained from AGA search are plotted in

Fig 5.3(a), (b), and (c) respectively. We noticed that those low-energy structures tend to have Ti

atoms bonded with six or five oxygen atoms in the GB region. This tendency to lower the energy

is related to bulk SrTiO$_3$ structure, in which each Ti atom is in the center of an octahedron

formed by oxygen atoms. By comparing our structure for $\Gamma_{TiO_2} = 1$ [Fig. 5.3(a)] with the one

proposed in the literature [Chua *et al.*, 2010], we found that both structures have 2 Ti atoms in

the GB region bonded with 5 oxygen atoms, but the locations of the empty octahedron sites are

different in the two structures. In the lowest-energy structure for $\Gamma_{TiO_2} = 2$ [Fig. 5.3(b)], all the

Ti atoms in the GB region have 6-fold coordination with oxygen atoms, while in the *Γ2-lit* structure two of Ti atoms have coordination number of 4. As plotted in Fig. 5.3(c), in the lowest-energy structure for $\Gamma_{TiO_2} = 3$, all the Ti atoms at the GB bond with 6 oxygen atoms, except one having coordination number of 5.
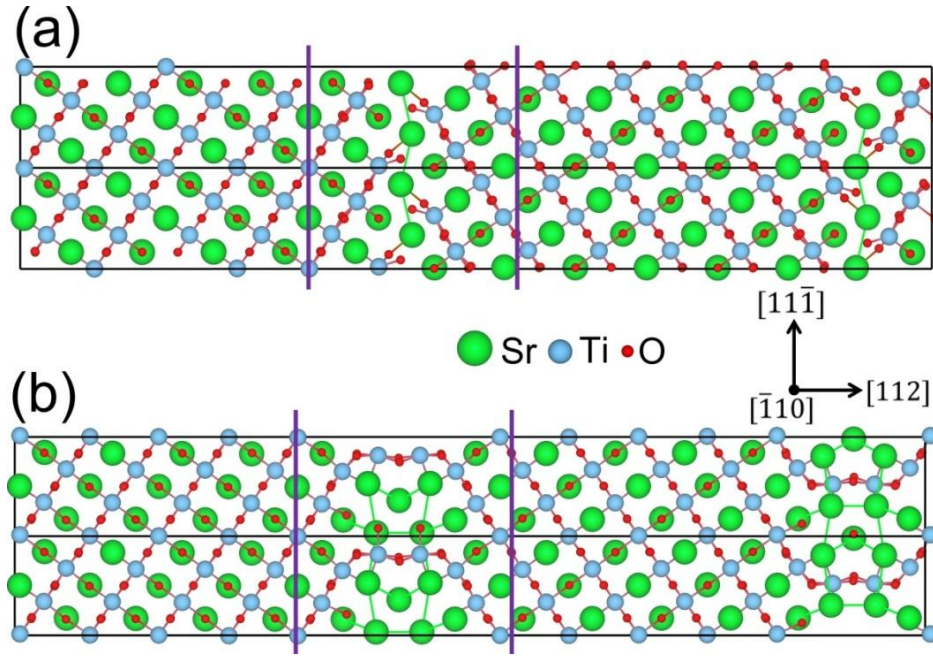
Figure 5.4 New grain boundary structures for negative Γ_{TiO_2}. (a) $\Gamma_{TiO_2} = -2$ Σ3(112)[$\bar{1}$10] grain boundary; (b) $\Gamma_{TiO_2} = -3$ Σ3(112)[$\bar{1}$10] grain boundary. The purple lines indicate one of the two equivalent grain boundary regions. Note: both structures plotted here are repeated twice along [11-1] direction and the unit cell is shown as the black box.

In Ref. [Chua *et al.*, 2010], for negative Γ_{TiO_2}, their genetic algorithm search was unable to locate any stable structures. In our study, stable structures for negative Γ_{TiO_2} can be found (see Fig. 5.2). For $\Gamma_{TiO_2} = -2$ and $\Gamma_{TiO_2} = -3$, the structures obtained from AGA search are more stable than the stoichiometric GBs as the chemical potential of SrO is close to the cohesive energy of the bulk SrO (i.e. λ close to 1). When λ = 1, the interfacial free energy of the $\Gamma_{TiO_2} =$

-2 structure is about 0.58 Jm^{-2} lower than that of the O$_2$-terminated stoichiometric structure. The atomic structures of $\Gamma_{TiO_2} = -2$ and -3 are plotted in Fig 5.4(a) and (b). Combining the results with both positive and negative excesses, we can see that the stoichiometric $\Sigma3(112)[\bar{1}10]$ GB is stable only in a small region of the chemical potential.

5.4.3 Discussions

We note that the AGA method is greatly superior to the conventional approach using classical potentials followed by refinements by first-principles calculations because the requirements for the classical potentials in the two approaches are very different. The conventional GA scheme requires accurate and transferable classical potentials that can describe the complicated global energy landscape of the system, so that the global energy-minimum structure can be captured from the GA search as a candidate for further refinement by first-principles calculations. Due to the simplicity of the interactions assumed by the classical potentials, it is usually very difficult and in many cases impossible to fit a classical potential which can accurately describe the global energy landscape of systems containing multiple chemical elements. In contrast, the classical potential in our AGA scheme is only an auxiliary potential to speed up the exploration of the configuration space. Such auxiliary classical potentials are updated adaptively under the guidance of first-principles calculations to describe the local energy landscape around different basins separately as schematically shown in Fig. 5.5. It is much easier to adjust the auxiliary potentials to accurately describe the energy landscape around each basin (or a subset of basins) one-by-one. As an example to show the different performances of conventional GA and AGA, the relative energies of two GB structures with $\Gamma_{TiO_2} = 2$ obtained from conventional GA and AGA are compared in Table 5.2. Structure A is the lowest-energy structure obtained from the AGA search, while structure B is the ground-state

structure from the conventional GA search using the Buckingham potential. First-principles DFT calculations confirm that structure A has lower energy, same as the AGA result. We note that although the Buckingham potential fits well to bulk $SrTiO_3$ properties, it fails to describe the lowest-energy structure at the GB. If the structure A is relaxed using the Buckingham potential, its energy is much higher than that of the structure B. Therefore, the true ground-state structure, i.e. structure A is unlikely to be captured by the conventional GA search. On the other hand, both structures with correct energy order can be captured by the AGA search since it can sample different local basins in the global energy landscape.

Table 5.2   Comparison of the performance of different potentials. Total energies of two structures with $\Gamma_{TiO_2} = 2$ obtained from AGA search (structure A) and the conventional GA search using Buckingham potential (structure B) were calculated. They are relaxed by the Buckingham type potential (pot_0), one of the adapted potentials (pot_A) and first-principles method (DFT) respectively. The calculations are based on supercell model with two equivalent grain boundaries (total 132 atoms) and the energy of structure B is set to be 0 as reference.

$\Gamma_{TiO_2} = 2$	Structure A	Structure B
$E(pot_0)$ (eV)	+1.74	0
$E(pot_A)$ (eV)	−0.966	0
$E(DFT)$ (eV)	−0.435	0
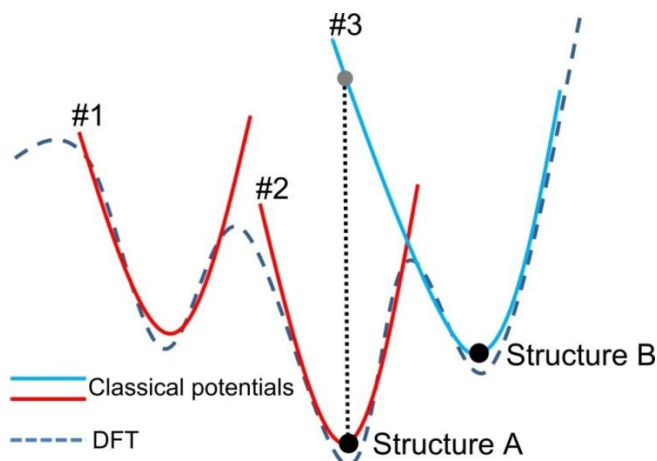
Figure 5.5   Schematic representation of potential energy surfaces explored in the AGA searches. Dashed line indicates the DFT energy landscape and solid lines indicate the energy surface of different classical potentials. In the AGA process, the classical potential is adaptively adjusted to fit the DFT results, so that it can hop between different local minima in the DFT energy surface (e.g. #1 and #2). Structure A and B are schematic representations of the examples in Table 5.2. Structure A is energetically unfavorable under classical Buckingham potential (e.g. #3), therefore is highly possible to be missed in the GA searches using this potential.
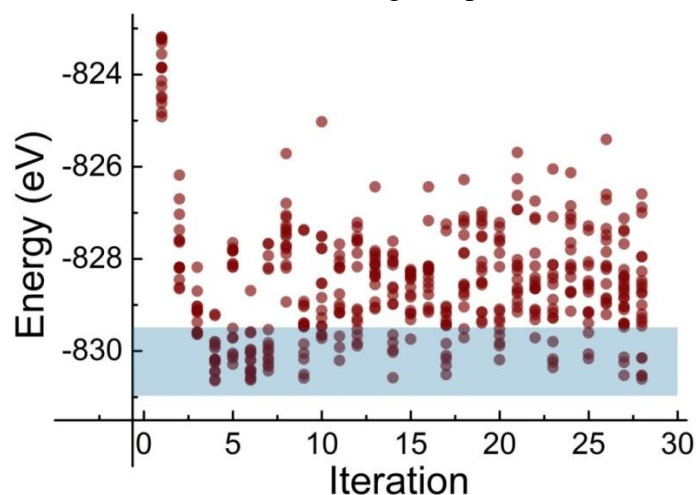
Figure 5.6   Energetic evolution in the AGA process. Each point on this plot represents the DFT energy of a selected structure, whose force and stress information was used to fit the classical potential. DFT energy here was calculated based on the structures from the GA searches using classical potential without further relaxation. In the end of the AGA search, structures in the energy window indicated by the shaded area were collected for final DFT relaxation optimizations to capture the global energy minimum structure.

Adapted auxiliary potentials throughout the AGA iterations also help the system hop from one basin to another and ensure efficient and accurate sampling of the configuration space. Figure 5.6 is an example of the energetic evolution versus the number of the adaptive iterations. Each point represents the DFT energy of a structure from the converged GA search using the classical potentials. We can see that the DFT energies of the obtained structures are relatively high in the first iteration and start to drop after the potential is adjusted. During the later search process, while the potentials keep being tuned, the corresponding DFT energies are hopping around. It should be noted that, since the classical potential can evolve towards a new set of parameters which can explore a new basin in the energy landscape, the DFT energy is not necessary decreasing with the iteration but rather fluctuating from iteration to iteration. In the end of the AGA search, all the structures within certain energy window, as shown in Fig. 5.6, will be collected and further optimized by first-principles calculations. In this way, the search can avoid being trapped at certain local minimum and locate the global optimum in the DFT energy surface.

Due to the complexity of the GB and interface systems, it is too time-consuming to perform GA searches using straightforward first-principles calculation. On the other hand, results obtained from classical potential search are not always reliable. In contrast, not only can AGA adjust the potentials iteratively to describe the local minima more accurately, it also allows the search to visit different basins in the energy surface more efficiently. Therefore, with current available computing capability, AGA provides a feasible tool for GB and interface structure predictions and optimizations.

5.5   Conclusions

In summary, we developed an efficient and accurate first-principles method for complex GB and interface structure prediction. It allows us to predict low-energy structures for systems with hundreds of atoms with affordable computing power. We performed AGA searches for the SrTiO$_3$ $\Sigma3(112)[\bar{1}10]$ GBs with Γ_{TiO_2} value ranges from -3 to $+3$. New lower-energy structures are predicted for the non-stoichiometric boundary, which provided a more comprehensive insight into the stability of the GB in SrTiO$_3$ over a wide range of chemical potential μ_{TiO_2}. In particular, We show that, in contrast to the previous results in the literature, the stoichiometric boundary is stable only within a chemical potential range of -0.72 eV $< \mu_{TiO_2} - g_{TiO_2} < -0.15$ eV. Outside this range, non-stoichiometric grain boundary structures are energetically more favorable. The capability to efficiently predict atomic structures of GBs and interfaces at the accuracy level of DFT paves a way for more accurate description of various properties at the interfaces and helps to speed up the pace of design and discovery of novel materials.

CHAPTER 6.   FAST MOTIF-NETWORK SCHEME FOR EXTENSIVE EXPLORATION OF THE CRYSTAL STRUCTURES IN SILICATE CATHODES[6]

6.1   Abstract

In this chapter, a motif-network search scheme is presented to study the crystal structures of the dilithium/disodium transition metal orthosilicates A_2MSiO_4. Using this fast and efficient method, the structures of all six combinations with A = Li or Na and M = Mn, Fe or Co were extensively explored. In addition to finding all previously reported structures, we discovered many other different crystal structures which are highly degenerate in energy. These tetrahedral-network-based structures can be classified into 1D, 2D and 3D types based on M-Si-O frames. A clear trend of the structural preference in different systems was revealed and possible indicators that affect the structure stabilities were introduced. For the case of Na systems which have been much less investigated in the literature relative to the Li systems, we predicted their ground state structures and found evidence for the existence of new structural motifs.

6.2   Introduction

Li_2MSiO_4 (M = Mn, Fe, Co) have been the subject of intensive studies as promising Li storage materials because of their high potential capacities, low cost, environmental friendliness and excellent safety characteristics. Realizing a two electron exchange per formula in orthosilicates leads to higher capacities (e.g. ~ 331 mAh/g for Li_2FeSiO_4) than the olivine

---

[6] This chapter is a version of the submitted article: Zhao, X., Wu, S. Q., Lv, X. B., Nguyen, M. C., Wang, C. Z., Lin, Z. J., Zhu, Z. Z., and Ho, K. M. "Fast motif-network scheme for extensive exploration of complex crystal structures in silicate cathodes", arXiv: 1504.02070.

phosphates where there is only one Li atom per formula unit [Dominko *et al.*, 2006; Kokalj *et al.*, 2007]. In the last decade, much effort has been devoted to the study of different Li_2MSiO_4 polymorphs. However, it was reported that Li_2FeSiO_4 exhibits a reversible capacity of only 130 ~ 165 mAh/g [Nytén *et al.*, 2005; Armstrong *et al.*, 2011; Sirisopanaporn *et al.*, 2011] or high initial charge capacities (~ 240 mAh/g) with noticeable decay in the following cycles [Lv *et al.*, 2011; Kojima *et al.*, 2012], while both Li_2MnSiO_4 [Dominko *et al.*, 2006; Li *et al.*, 2007; Muraliganth *et al.*, 2010; Gummow *et al.*, 2012] and Li_2CoSiO_4 [Lyness *et al.*, 2007] show more than one electron exchange in the first charge cycle but suffer from poor rate capability and drastic capacity fade.

In comparison with the Li compounds, much less experimental work was carried out to investigate the orthosilicates as Na host matrix. The chemical similarities between Na and Li imply that exploration of the sodium equivalent offer more opportunities to advance energy storage technology through rechargeable batteries, owing to the even lower cost and ubiquitous availability of Na. Recently [Chen *et al.*, 2014], Na_2MnSiO_4 was synthesized and investigated for use as a positive electrode material for Na secondary batteries. A reversible capacity of 125 mAh/g was found compared with the theoretical capacity of 278 mAh/g based on the two electron reaction.

The discrepancy between measured and calculated capacities has been attributed to the instability of the crystal structures upon delithiation/desodiation [Kokalj *et al.*, 2007; Duncan *et al.*, 2011; Chen *et al.*, 2014; Lee *et al.*, 2014]. In order to circumvent the capacity fading and further improve the electrochemical properties, it is essential to understand their crystal structures and explore other possible polymorphs that may be stable in the delithiated/desodiated state.

Experimental data indicate that the crystal structures of the orthosilicate compounds A_2MSiO_4 (A = Li, Na; M = Mn, Fe, Co) belong to a family of tetrahedral structures that exhibit a rich polymorphism [West and Glasser, 1972; Bruce and West, 1980]. Polymorphs of these tetrahedral structures were classified into low- and high-temperature forms, which differ in the distribution of cations within tetrahedral sites of a hexagonal close-packed (hcp) based arrangement of oxygen. Five different structures were observed and studied for Li_2FeSiO_4 [Nytén *et al.*, 2005; Armstrong *et al.*, 2011; Sirisopanaporn *et al.*, 2011; Eames *et al.*, 2012; Saraciber *et al.*, 2012; Zhang *et al.*, 2012], three as-synthesized (two are orthorhombic, *Pmnb* and *Pmn*2$_1$; one is monoclinic, *P*2$_1$/*n*) and two cycled phases (*Pmn*2$_1$-cycled and *P*2$_1$/*n*-cycled). Likewise, multiple phases have been reported for Li_2MnSiO_4 (*Pmn*2$_1$ [Dominko *et al.*, 2006], *Pn* [Duncan *et al.*, 2011], *P*2$_1$/*n* [Politaev *et al.*, 2007] and *Pmnb* [Gummow *et al.*, 2012]) and Li_2CoSiO_4 (*Pnb*2$_1$ [Armstrong *et al.*, 2010], *Pmn*2$_1$ [Lyness *et al.*, 2007; Armstrong *et al.*, 2010], and *P*2$_1$/*n* [Armstrong *et al.*, 2010]). The recent work of Na_2MnSiO_4 [Chen *et al.*, 2014] showed that Na_2MnSiO_4 has a monoclinic structure with space group *Pn*.

In the above reported structures of A_2MSiO_4, all the atoms form tetrahedral units, i.e. every atom is in the center of a tetrahedron and has a coordination number of 4. Taking advantage of this structural feature, we developed a fast motif-network scheme based on genetic algorithm [Deaven and Ho, 1995] to explore the complex crystal structures of these materials.

6.3   Methods

Although systematic enumerations of 4-connected crystalline networks have been applied to zeolites and other silicates [Deem *et al.*, 1989; Treacy *et al.*, 2004; Foster *et al.*, 2004], considering the great effort of selecting energetically preferable structures out of millions of possible configurations owing to the lack of decent classical potentials for A_2MSiO_4, here we

took a different route to obtain tetrahedral networks from the low-energy crystal structures of silicon. Silicon is well known to have rich phases and forms sp3-hybridized framework structures [Nguyen *et al.*, 2014]. We used GA and Tersoff potential [Tersoff, 1998] to search for silicon structures that form tetrahedral networks. Once such a silicon structure was located, all the sites were re-assigned to A (Li or Na), M (Mn, Fe or Co), Si and O atoms in the ratio of 2:1:1:4. During the substitution, only structures where every oxygen atom bonds with two A atoms, one M atom and one Si atom, as illustrated in Fig. 6.1, were accepted. This is because of the observation that structures with uniformly distributed A, M and Si atoms have noticeably lower energies. Newly generated structures that had not been visited were collected for further refinement by first-principles calculations. In this way, various A_2MSiO_4 structures were obtained.
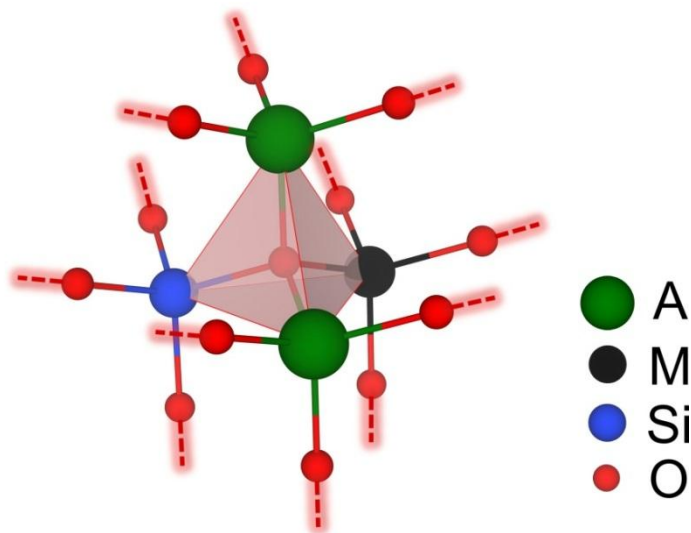
Figure 6.1 Schematic representation of the structure generations. The A_2MSiO_4 structures are generated from tetrahedral networks, where A = Li or Na; M = Mn, Fe or Co. For a given tetrahedral network, once one of its sites (e.g. the center of the tetrahedron) is assigned to oxygen, its four neighbors are randomly assigned to two A atoms, one M atom and one Si atom. Then, neighbors of A, M and Si are only assigned to oxygen atoms. In such an iterative manner, the occupations of all sites are determined. The oxygen-centered tetrahedron is shown by red, transparent planes.

The first-principles calculations on A_2MSiO_4 (A = Li, Na; M = Mn, Fe, Co) were carried out using the projector augmented wave (PAW) method [Kresse and Joubert, 1999] within density functional theory (DFT) as implemented in the Vienna ab initio simulation package (VASP) [Kresse and Furthmuller, 1996]. The exchange and correlation energy is treated within the spin-polarized generalized gradient approximation (GGA) and parameterized by Perdew-Burke-Ernzerhof formula (PBE) [Perdew *et al.*, 1996]. Wave functions are expanded in plane waves up to a kinetic energy cut-off of 500 eV. Brillouin zone integration was performed using the Monkhorst-Pack sampling scheme [Monkhorst and Pack, 1976] over k-point mesh resolution of $2\pi \times 0.03$ Å^{-1}. The ionic relaxations stop when the forces on all the atoms are smaller than 0.01 eV·Å^{-1}.

Since the energy difference between ferromagnetic (FM) and antiferromagnetic (AFM) is very small and the resulting lattice parameters are almost the same [Wu *et al.*, 2007; Wu *et al.*, 2009], all calculations in present work were spin-polarized with FM configuration. The effects due to the localization of the d electrons of the transition metal ions in the silicates were taken into account with the GGA + U approach of Dudarev et al. [Dudarev *et al.*, 1998]. Within the GGA + U approach, the on-site coulomb term *U* and the exchange term *J* were grouped together into a single effective interaction parameter $U_{eff} = U\text{-}J$. In our calculations, *U-J* values were set to 4 eV for M = Fe, and 5 eV for M = Co, Mn.

Generation of the tetrahedral networks costs very little time due to the usage of classical potentials during the GA searches. In this work, up to 48 atoms in the unit cell were searched for Si to find tetrahedral networks, i.e. up to 6 formula units were considered for A_2MSiO_4. In order to obtain as many tetrahedral networks as possible, energies of the silicon structures that satisfy

the coordination constraints (every atom in the structure has a coordination number of 4) were lowered by a pre-set amount to increase their chance of survival.

6.4 Results and discussions
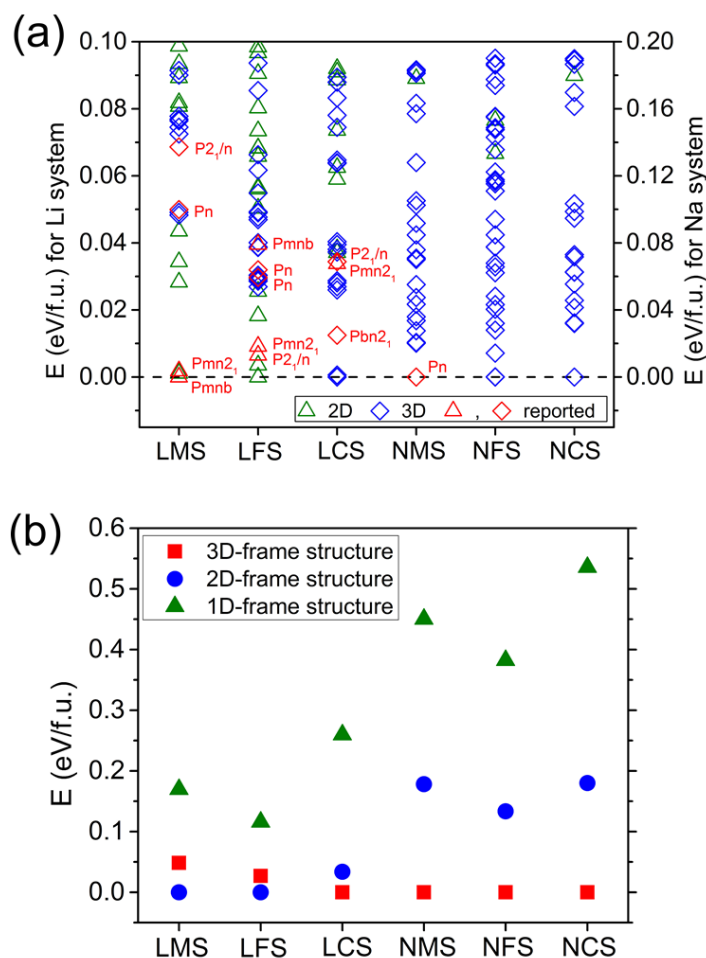
Figure 6.2 Energetic results. (a) Relative energies of the structures obtained in this work for Li_2MnSiO_4 (LMS), Li_2FeSiO_4 (LFS), Li_2CoSiO_4 (LCS) and Na_2MnSiO_4 (NMS), Na_2FeSiO_4 (NFS), Na_2CoSiO_4 (NCS). Triangles (green) indicate the layered 2D-frame structures and diamonds (blue) indicate 3D-frame structures. Structures that have been reported in the literature are shown in red color and also labeled by their space groups. For the two LFS *Pn* phases, the lower-energy one corresponds to the *Pmn2_1*-cycled phase with 2 formula units and the higher-energy one corresponds to the *P2_1/n*-cycled phase with 4 formula units. (b) Relative energies of the most stable 3D-, 2D-, and 1D-frame structures for each system. Energy of the ground state structure for each system is set to 0 eV as reference in (a) and (b).

Results of the A_2MSiO_4 structures from current study are summarized in Fig. 6.2, where the relative energies are plotted by setting the energy of the ground state structure to 0 eV for each system. We found that the structures of A_2MSiO_4 are highly degenerate in energy, in agreement with the rich crystal chemistry observed in experiments. Using our method, in addition to the structures previously reported in the literature [shown in red color in Fig. 6.2(a)] and structures included in the Materials Project database [Jain *et al.*, 2013], many more structures with competitive or even lower energies were found. Within the energy window plotted in Fig. 6.2(a), less than 10 structures were included in the Materials Project database for each Li system and none for the Na systems, while more than 30 structures are shown in Fig. 6.2(a) for each system. We classified those low-energy structures into different types based on the M-Si-O frames [Saracibar *et al.*, 2012; Lee *et al.*, 2014].

6.4.1 3D-frame structures

In the first type (referred to as "3D-frame structure" from now on), M, Si and O atoms form a 3D frame (see examples plotted in Fig. 6.3). Difference between structures in Fig. 6.3(a), (b) and (c) comes from the different orientations of the tetrahedrons and all three structures consist of only 2-hole ring as indicated by the arrow in Fig. 6.3(a). In contrast, structures in Fig. 6.3(d) and (e) consist of a combination of 1-hole ring and 3-hole ring as indicated in the plot. Structure in Fig. 6.3(f) mixes the 2-hole rings and the combination of 1 & 3-hole rings. In these structures, M and Si atoms occupy different tetrahedron centers in an oxygen hcp framework, affecting the orientation of the tetrahedrons. Following this structural motif, more structures with similar features and various mixings can be constructed by increasing the size of the unit cell.
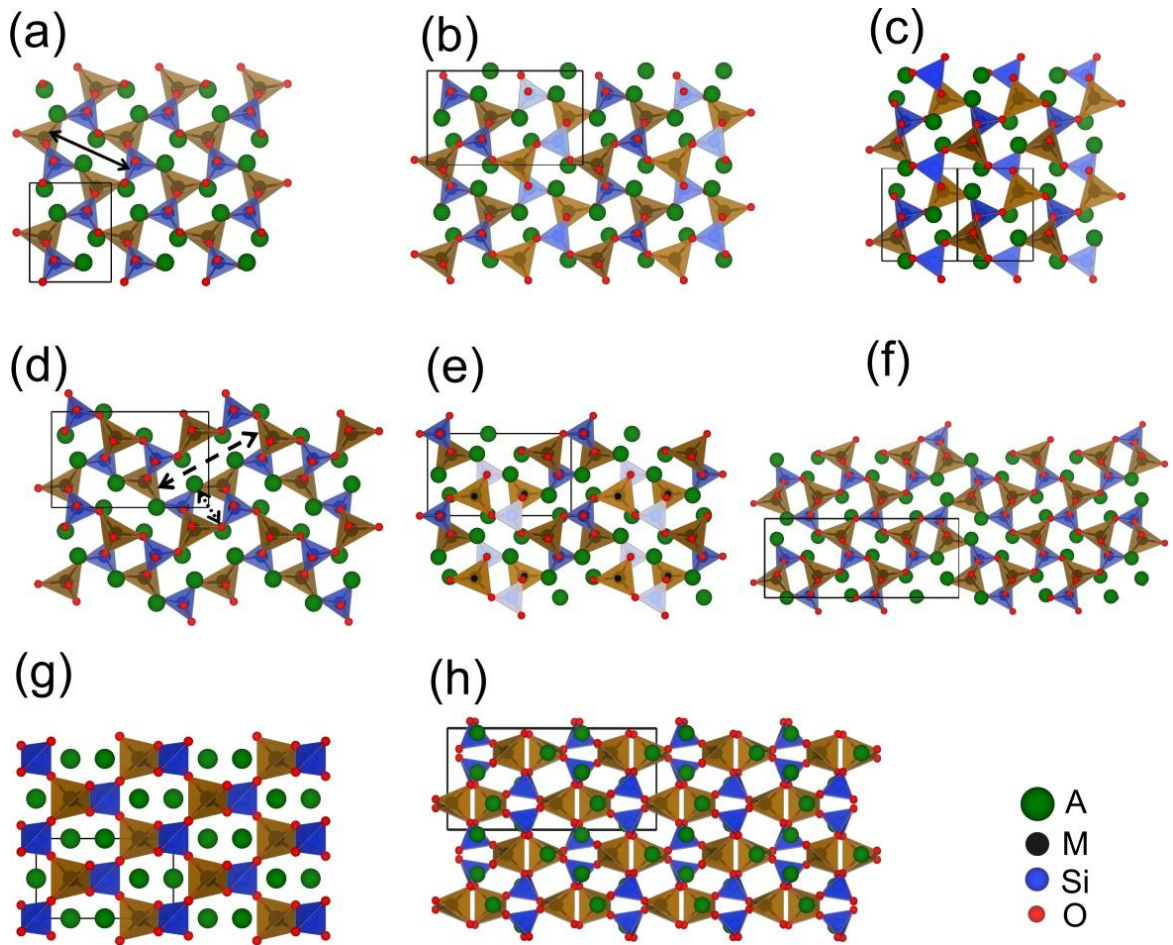
Figure 6.3 Examples of the 3D-frame structures. Space group of each structure is (a) *Pn* (# 7), (b) *Pna2₁* (# 33), (c) *C222₁* (# 20), (d) *Pna2₁* (# 33), (e) *P2₁2₁2₁* (#19), (f) *Pn* (# 7), (g) *I-4* (# 82), and (h) *Pccn* (# 56). Solid arrow in (a) indicates the 2-hole ring; dash arrow in (d) indicates the 3-hole ring; dot arrow in (d) indicates the 1-hole ring. The black boxes indicate the unit cells of each structure.

The structures plotted in Fig. 6.3(g) and (h) look distinct from the others, but the M and Si atoms share the same local tetrahedral environment. Although less favored in energy than the structures plotted in Fig. 6.3(a-f), the differences are very small. For instance, for Na_2FeSiO_4, the energies of the structures in Fig. 6.3(g) and (h) are about 0.11 and 0.12 eV/f.u. higher respectively than the ground state structure.

6.4.2 2D-frame structures
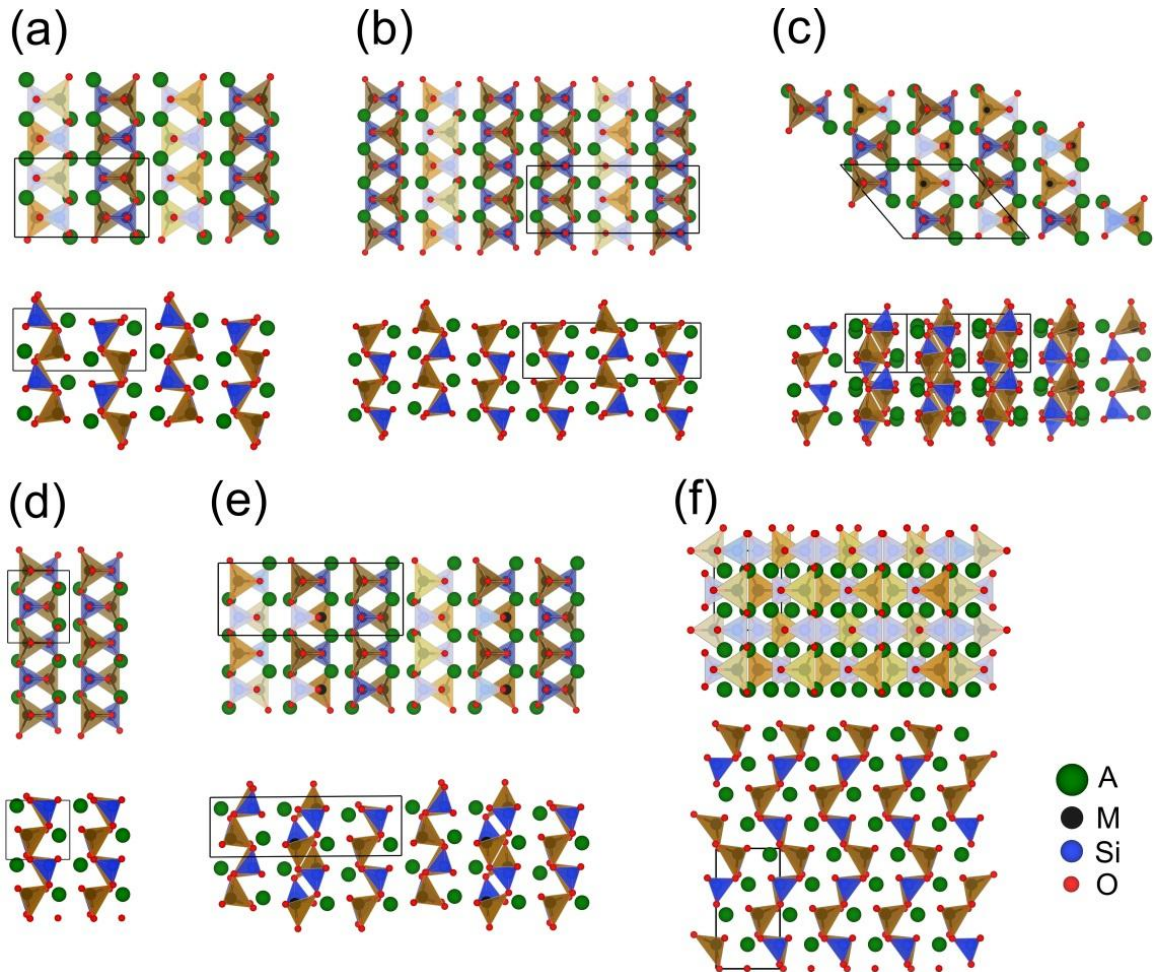
Figure 6.4 Examples of the 2D-frame structures. Space group of each structure is (a) *Pnma* (# 62), (b) *Pmn2₁* (# 31), (c) *P2₁/n* (# 14), (d) *Pmn2₁* (# 31), (e) *P2₁/m* (# 11), (f) *Pn* (# 7). Two mutually perpendicular views are plotted for each structure. The black boxes indicate the unit cells of each structure.

The second type (referred to as "2D-frame structure") is that M, Si and O atoms form disconnected layers, as those plotted in Fig. 6.4. Similar to the 3D-frame structures, M and Si atoms can occupy different tetrahedron centers and as a result, the orientation of the tetrahedrons looks different in different structures. For example, the structures plotted in Fig. 6.4(a), (b) and (d) are from various stacking of two different tetrahedron-oriented layers and in each layer, all

the tetrahedrons point to the same direction. In comparison, layers in the structures plotted in Fig. 6.4(c) and (e) mix different-oriented tetrahedron. It can also be expected that by increasing the unit cell size, more ways to stack those layers can be found. Meanwhile, through the exchange of the A and M atoms, more layered structures were found as Fig. 6.4(f), which becomes closer to the 3D-frame structures.

6.4.3   Existence of 1D-frame structures?
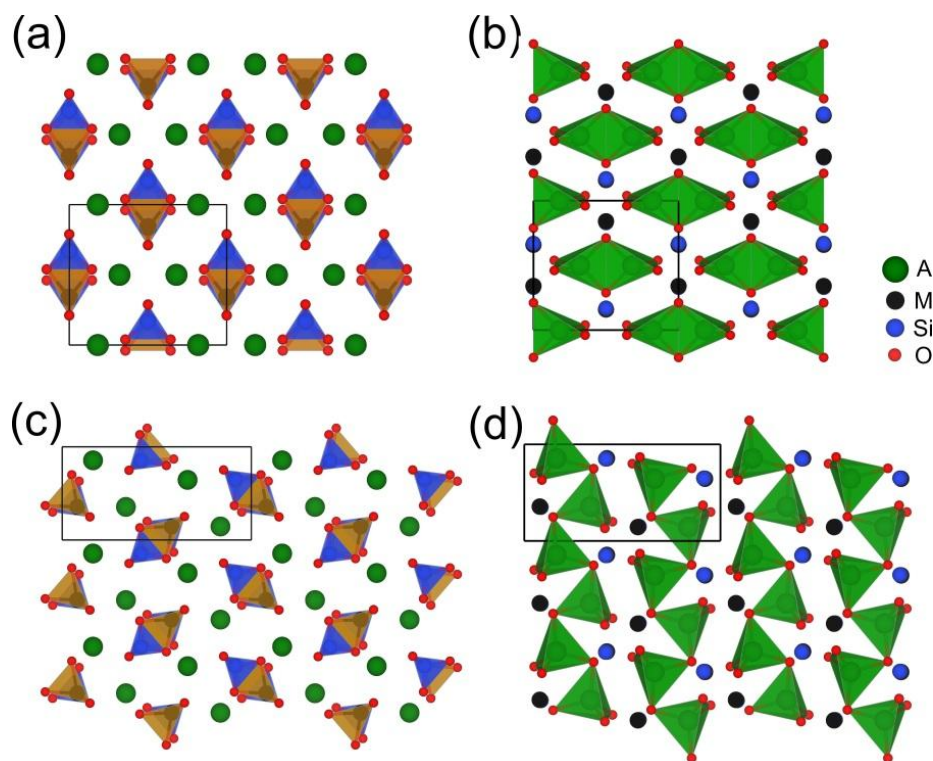
Figure 6.5   Examples of the 1D-frame structures. The structure plotted in (a) and (b) has space group *Cmcm* (#63) and the structure plotted in (c) and (d) has space group *Pnma* (# 62). In (a) and (c), the M-centered and Si-centered tetrahedrons are plotted; in (b) and (d), the A-centered tetrahedrons are plotted. Black boxes indicate the unit cells of each structure.

Both the 2D- and 3D-frame structures have been observed in experiments for Li_2MSiO_4 and extensively studied in the literature. It is natural to continue the query of the existence of "1D-frame structure", where the M, Si and O atoms form disconnected rods. From our search,

such structures were observed as shown in Fig. 6.5. In both structures plotted in Fig. 6.5, the M-centered and Si-centered tetrahedrons are edge-sharing with each other and extend in one direction to form the M-Si-O rod. However, the orientations of the M-Si-O rod are different between them, which can be seen by comparing Fig. 6.5(a) and (c). From the view of the Na-centered tetrahedrons, we see that in the *Cmcm* structure [Fig. 6.5(b)], A and O atoms also form separated rods which align perpendicularly to the M-Si-O rods, while in the *Pnma* structure [Fig. 6.5(d)], A and O atoms forms 2D layers. In fact, the *Pnma* structure plotted in Fig. 6.5(c) and (d) can be obtained from the structure plotted in Fig. 6.4(a) by switching all the alkali metal atoms with M and Si atoms and arranging M and Si in an orderly manner.

Under above classification, different symbols are used in Fig. 6.2(a) to represent the types of those low-energy structures obtained in this work. It can be seen that within the energy window plotted in Fig. 6.2(a), i.e. 0.1 eV/f.u. for Li systems and 0.2 eV/f.u. for Na systems, more 2D-frame structures are found for the Li systems and more 3D-frame structures are found for the Na systems. 1D-frame structures are not showing in Fig. 6.2(a) due to their relatively higher energies (0.1~0.2 eV/f.u. for Li-systems and 0.2~0.4 eV/f.u. for Na-systems). In Fig. 6.2(b), we plotted the relative energies of the most stable 3D-, 2D-, and 1D-frame structures for each system, from which the stabilities of each type can be compared. The preference of different structure types for different systems will be discussed next.

6.4.4   Structure preference and analyses

In Table 6.1, we listed the lowest-energy structures for each system in three different types. We note that 2D-frame structures are the ground state for Li_2MnSiO_4 and Li_2FeSiO_4 while 3D-frame structures are more favored by Li_2CoSiO_4. For the Na-system, all three favor the 3D-frame structures. The trend can also be seen clearly from Fig. 6.2(b). This could be related to the

atomic size of the cations. By comparing the atomic radius r of A and M atoms [r(Na) > r(Li) > r(Mn) > r(Fe) > r(Co)], we see that with r(A)/r(M) getting closer to 1, layered structures are more favored. When the atomic size difference between A and M is too big, layered structures will introduce large strain, thus becoming less favored.

On the other hand, it can be seen from Fig. 6.6(a) that when the A-O bond length is smaller than the M-O bond length, 2D-frame structures are favored; otherwise, 3D-frame structures are favored. Thus the relative bond length between A-O and M-O can serve as a clearer indicator. At the same time, we see that Si-O bond length are very close for all six systems and the changes in A-O bond lengths among different transition metal systems are also small for both Li and Na. In the Na systems, the variance (standard deviation) of the bond length from the mean value is significantly larger than the Li system, i.e. larger distortions are found in the Na systems due to the larger size of the Na atom. As a result, in comparison with Li_2MSiO_4, the structures of Na_2MSiO_4 have relatively lower symmetries.

To compare the 2D- and 3D-frame structures, in Fig. 6.6(b) and (c), we plotted the statistical results of the M-O bond lengths and volumes of them. It is found that for all six systems, the M-O bond lengths in the 2D-frame structures are larger than those in the 3D-frame structures, yet the volumes of the 2D-frame structures are smaller than those of the 3D-frame structures. As for the 1D-frame type, from the information listed in Table 6.1, it can be seen that the lowest-energy 1D-frame structure for all six systems has space group *Cmcm* with much larger volume than the 2D- and 3D-frame structures.

Table 6.1 Lowest-energy structures of A_2MSiO_4 in three different types obtained in current study. r represents the atomic radius; E is the total energy in eV/f.u.; V is the volume of the structure in $Å^3$/f.u.; a, b, and c are the lattice parameters in Å.

		Li_2MnSiO_4	Li_2FeSiO_4	Li_2CoSiO_4	Na_2MnSiO_4	Na_2FeSiO_4	Na_2CoSiO_4
r(A)/r(M)		1.04	1.07	1.10	1.18	1.22	1.25
1D-frame type	E	-54.891	-53.174	-51.070	-52.212	-50.497	-48.398
	Space group	*Cmcm* (#63)	*Cmcm* (#63)	*Cmcm* (#63)	*Cmcm* (#63)	*Cmcm* (#63)	*Cmcm* (#63)
	Lattice	a=7.40, b=7.56, c=6.42	a=7.47, b=7.49, c=6.30	a=7.54, b=7.52, c=6.18	a=8.89, b=8.09, c=6.39	a=8.95, b=7.96, c=6.31	a=8.96, b=7.98, c=6.22
	V	89.80	88.12	87.61	114.89	112.38	111.18
	plot	Fig. 6.5(a)	Fig. 6.5(a)	Fig. 6.5(a)	Fig. 6.5(a)	Fig. 6.5(a)	Fig. 6.5(a)
2D-frame type	E	**-55.061**	**-53.290**	-51.296	-52.484	-50.746	-48.754
	Space group	*Pmna* (#62)	*Pmna* (#62)	$Pmn2_1$ (#31)	*P*-1 (#2)	*P*-1 (#2)	*P*-1 (#2)
	Lattice	a=10.91, b=6.38, c=5.10	a=10.80, b=6.33, c=5.05	a=6.20, b=5.46, c=5.00	a=5.61, b=6.11, c=6.27, $α$=77.64°, $β$=89.96°, $γ$=89.87°	a=5.73, b=6.05, c=6.12, $α$=75.43°, $β$=87.99°, $γ$=89.17°	a=5.53, b=6.01, c=6.20, $α$=103.40°, $β$=90.27°, $γ$=90.25°
	V	88.66	86.33	84.60	105.00	102.76	100.36
	plot	Fig. 6.4(a)	Fig. 6.4(a)	Fig. 6.4(d)	Fig. 6.7	Fig. 6.7	Fig. 6.7
3D-frame type	E	-55.012	-53.263	**-51.330**	**-52.662**	**-50.879**	**-48.934**
	Space group	$Pna2_1$ (#33)	$P2_12_12_1$ (#19)	*Pn* (#7)	*Pn* (#7)	*Pn* (#7)	*Pn* (#7)
	Lattice	a=11.05, b=6.39, c=5.07	a=11.02, b=6.29, c=5.07	a=5.01, b=16.20, c=8.07, $β$=128.33°	a=5.42, b=5.72, c=8.87, $β$=127.39°	a=5.41, b=5.71, c=8.74, $β$=127.67°	a=5.34, b=5.58, c=8.82, $β$=127.06°
	V	89.48	87.72	85.59	109.33	106.71	104.78
	plot	Fig. 6.3(d)	Fig. 6.3(e)	Fig. 6.3(f)	Fig. 6.3(a)	Fig. 6.3(a)	Fig. 6.3(a)
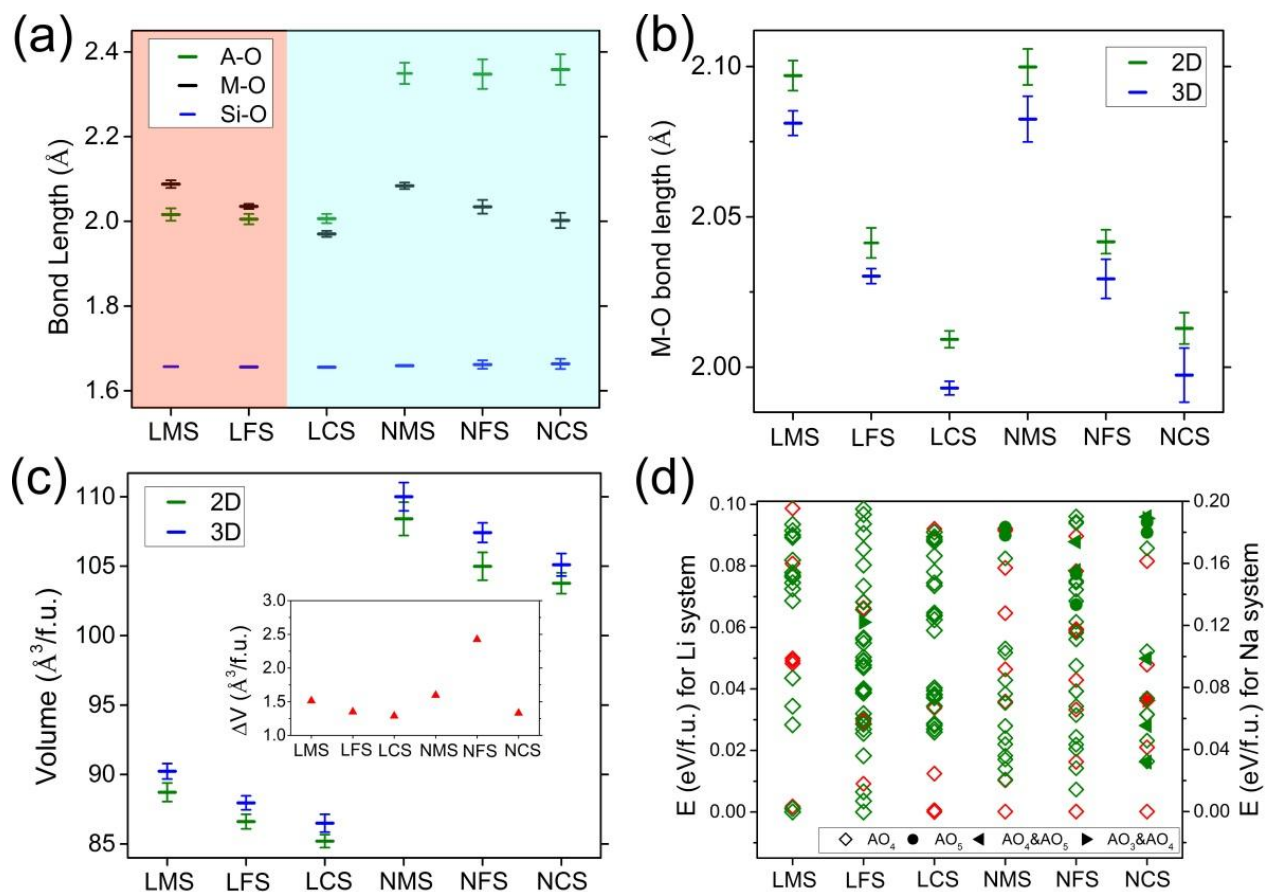
Figure 6.6 Structure analyses. (a) Average cation-oxygen bond lengths in different systems. The average is calculated over 30 lowest-energy structures for each system. The red-shaded area represents systems favoring the 2D-frame structures and the blue-shaded area represents systems favoring the 3D-frame structures. (b) Average M-O bond lengths in the 2D-frame and 3D-frame structures for different systems. (c) Average volumes of the 2D-frame and 3D-frame structures for different systems. The average volume difference is plotted as the inset. (d) Local environment of the alkali metal atoms and the connections between the cation-centered tetrahedrons in all the structures plotted in Fig. 6.2(a). Green color indicates structures that have edge-sharing tetrahedrons; red color indicates structures with only vertex-sharing tetrahedrons. Different symbol types represent different local environment of the A (= Li, Na) atoms, i.e. how many oxygen atoms are neighbored by the A atoms. Error bars in plots (a), (b) and (c) represent one standard deviation of the samples.

In Fig. 6.6(d), we plotted the local environment of the alkali metal atoms and also the connections between the cation-centered tetrahedrons for all the structures in Fig. 6.2(a). To determine whether an oxygen atom is counted as a nearest neighbor of the cation atom, we first sorted all the cation's neighbors according to distance and allowed 10% of increase in the bond length relative to the average of those which have been counted. The results show that for most Li_2MSiO_4 structures, the Li atoms bond with 4 oxygen atoms; while for Na_2MSiO_4, Na atoms in some structures have different coordination numbers. As shown in Fig. 6.6(d), Na atoms can have coordination numbers of 3 or 5.

Among all the low-energy structures, we also find that most of them contain edge-sharing tetrahedrons which are shown in the green color in Fig. 6.6(d). Structures with only vertex-sharing tetrahedrons, as shown in the red color, are more common in the Na systems, but overall, there is no clear indication on how the connection of tetrahedrons affects the stability of the structures.

6.4.5   What can be expected for the Na systems?

Since the Na-intercalation chemistry of the Na-based systems has been considerably less explored, there may be opportunity to find novel electrode materials for sodium-ion battery [Kim *et al.*, 2012]. Experimental studies on the orthosilicates as Na host matrix have just begun.
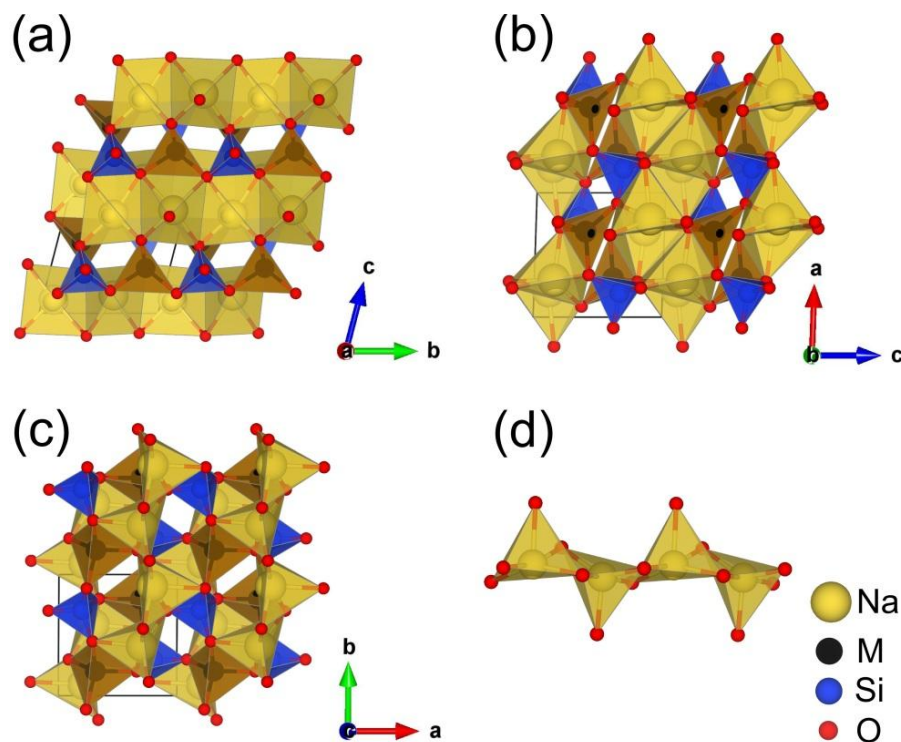
Figure 6.7 The lowest-energy 2D-frame structure for the Na systems with space group *P*-1 (#2). (a-c), Views of the *P*-1 structure along different lattice vectors. (d) Na-O pyramids extracted from this structure, where every Na atom bonds with 5 O atoms.

In this work, we found that Na systems prefer 3D-frame structures and have relatively low symmetries. As shown in Table 6.1, the lowest-energy structure for all the Na systems has space group *Pn* and similar lattice parameters. The *Pn* structure, which is plotted as Fig. 6.3(a), has been reported for Na_2MnSiO_4 experimentally [Chen *et al.*, 2014]. Among the 2D-frame structures obtained in current study, the lowest-energy one for all three Na systems has space group *P*-1. This *P*-1 structure is plotted in detail in Fig. 6.7. Comparing with those plotted in Fig. 6.4, the lowest-energy 2D-frame structure for Na system is much more distorted under DFT relaxation and the coordination number of all Na atoms is 5. In Fig. 6.7(d), the Na-O pyramids were plotted. We can see that the center Na atom sits very close to the base plane and four of the

five Na neighbors are almost located on the same plane, i.e. such NaO_5 pyramid can be considered as half of an octahedron.

The much larger distortions observed in the Na systems indicates that structures with brand new motifs and more competitive energies could exist for the Na compounds, which cannot be fully covered using the method presented in this work. The search space starting from tetrahedral networks has been limited and further studies using more general search schemes should be carried out in order to get a more comprehensive picture of the Na_2MSiO_4 structures.

6.5 Conclusions

In conclusion, by taking advantage of known structural features, we developed a fast motif-network scheme to study the complex crystal structures of the silicate cathode systems for Li-ion/Na-ion batteries. Using the tetrahedral networks generated from silicon, we found that the structures of A_2MSiO_4 for both Li and Na systems are highly degenerate in energy. All the structures of Li_2FeSiO_4, Li_2MnSiO_4, Li_2CoSiO_4 and Na_2MnSiO_4 that have been reported in the literature were successfully found in our search. Many structures with comparable or even lower energies were revealed, and classified into different types based on the M-Si-O frames.

Through statistical analysis, we showed that structure preference can be related to the relative atomic radius of A and M atoms and the relative bond length of A-O and M-O bonds. Based on these factors, the structures of A_2MSiO_4 systems may be controlled through alloying, e.g. doping atoms with different sizes. In addition, existence of brand new motif/structure can be expected in such systems, especially for the Na compounds. The scheme proposed here can be easily extended to other similar systems and serve as a novel approach for extensive exploration of complex crystal structures.

CHAPTER 7.   ONGOING WORK AND CONCLUSIONS

As discussed in the introduction, building the structure-property correlation is essential to materials discovery and design. DFT and post-processing tools based on DFT results have achieved great success in comprehensive descriptions of materials, such as the mechanical properties [LePage and Saxe, 2001; Černý *et al.*, 2003], magnetic properties [Hobbs *et al.*, 2000], spectroscopy and dielectric properties [Hofer *et al.*, 2003; Vanderbilt, 2004; Gajdos *et al.*, 2006], electronic transport [Kudrnovský *et al.*, 2000; Stokbro *et al.*, 2003], liquids and glasses [Sheng *et al.*, 2006], etc. Nonetheless, DFT is not accurate for all problems, even with the continuous effort to construct exchange-correlation functionals. In particular, the predictive capability of DFT with LDA/GGA becomes limited or completely fails for systems with significant electronic correlation effects, such as materials containing transition metal or rare earth element with f-electron.

Several methods have been proposed and intensively studied in the last two decades to go beyond LDA/GGA, such as LDA+U [Anisimov *et al.*, 1991] and LDA plus Dynamical Mean Field Theory (LDA+DMFT) [Savrasov *et al.*, 2001; Kotliar *et al.*, 2004, 2006]. LDA+U method takes into account the onsite Coulomb repulsion in a static mean-field way and works well for materials with strong electron correlation. But it fails for materials with intermediate correlation effect. LDA+DMFT method, on the other hand, behaves correctly from weakly correlated materials to strongly correlated materials, but suffering from the large computational load. Recently, a combination of density functional theory and the Gutzwiller approximation (LDA + GA) has also been developed to calculate the ground-state properties of correlated systems and successful applied in a few cases [Deng *et al.*, 2009; Wang *et al.*, 2010; Lanata *et al.*, 2013]. It

should be pointed out that the methods mentioned above all have an adjustable parameter U, which is manually added in an *ad hoc* manner and limits their predictive power.

Different from those hybrid approaches which require prior determination of the screened Coulomb repulsion U, a Gutzwiller density functional theory has been proposed as an *ab initio* approach which directly takes the Coulomb integrals of the local orbitals and incorporates the screening process explicitly through a self-consistent solution of the many-electron wave function [Ho *et al.*, 2008; Yao *et al.*, 2011]. Later, the correlation matrix renormalization approximation (CMR) was introduced to calculate the expectation value of the many-electron Hamiltonian with a variational many-electron wave function of the Gutzwiller form with reduced computational complexity [Yao *et al.*, 2014].

Based on the recent development of the parameter-free theory in our group, I am currently working on the Gutzwiller density functional theory for studying the strongly correlated electron systems, to be more specific, investigating the effect brought by including the many-body screening processes into the self-consistent calculations (see Appendix A for more details).

To conclude, the thesis discussed our work on studying the structures and properties of materials to assist experiment accelerating the pace of materials discovery and design. We developed a fast and efficient algorithm, i.e. AGA, for predicting crystal structures and also extended it to tackle interface/surface problems. Using AGA, we were able to solve the complicated atomistic structures of the "$Co_{11}Zr_2$" polymorphs, thus identifying the hard magnetic phase in this system to be the high-temperature rhombohedral phase. The advantage of the AGA method in speed also allowed us to quickly scan multiple compositions of the ternary Co-Zr-B system. With the obtained structure information, we built the contour map of the energetics and

magnetic properties in the Co-Zr-B system and found that proper boron-doping could greatly improve the magnetic anisotropy of the Co-Zr alloys, pointing out a way to optimize their magnetic performance through chemical doping. One example of predicting new thermodynamically and dynamically stable compounds was also discussed in this thesis, where several stable Re-B structures were predicted and shown to be ultra-hard.

In the viewpoint of method development, we also studied various computational methods for multi-scale simulations of material behavior, e.g. Monte Carlo method as discussed in study of alnico magnets. In addition, the motif-network scheme was introduced as a special case of the topological modeling methods to investigate the complex structures of silicate cathode materials. The results provided us a more comprehensive picture of the crystal structures of A_2MSiO_4 (A = Li, Na; M = Mn, Fe, Co) and offered more polymorphs of them which could be stable during the delithiated/desodiated process.

With the continuous effort of the computational community and more and more powerful computing capabilities, we believe computational modeling and simulations will play more and more important roles in modern materials discovery and design.

APPENDIX A.   INCLUDING MANY-BODY SCREENING INTO SELF-CONSISTENT CALCULATIONS

In the case of γ-phase Ce, the electron Hamiltonian can be written in terms of the local natural basis-set orbitals:

$$\mathcal{H} = \sum_{(i\alpha) \neq (j\beta), \sigma} t_{i\alpha j\beta} c^{\dagger}_{i\alpha\sigma} c_{j\beta\sigma} + \sum_{i,\alpha,\sigma} \varepsilon_{i\alpha} c^{\dagger}_{i\alpha\sigma} c_{j\alpha\sigma} \\ + \frac{1}{2} \sum_{i,(\gamma\sigma) \neq (\gamma'\sigma)} U^{i}{}_{\gamma\gamma'} c^{\dagger}_{i\gamma\sigma} c_{i\gamma\sigma} c^{\dagger}_{i\gamma'\sigma'} c_{i\gamma'\sigma'}$$

(A.1)

where α, β, γ run over the local correlated orbitals. $t_{i\alpha j\beta}$ is the electron hopping element between orbital α at site i and orbital β at site j. $\varepsilon_{i\alpha}$ is the orbital level. $c^{\dagger}(c)$ is the electron creation (annihilation) operator. σ is the spin index.

We introduce a Gutzwiller operator in the following form [Yao *et al.*, 2011]:

$$\hat{G} = e^{-\sum_{i\mathcal{F}} g_{i\mathcal{F}} |\mathcal{F}_{\mathrm{i}}\rangle\langle\mathcal{F}_{\mathrm{i}}|}$$

(A.2)

where $|\mathcal{F}_{\mathrm{i}}\rangle$ is the Fock state generated by a set of $\{c^{\dagger}_{i\gamma\sigma}\}$: $|\mathcal{F}_{\mathrm{i}}\rangle = \prod_{\gamma\sigma} (c^{\dagger}_{i\gamma\sigma})^{n^{\mathcal{F}}_{i\gamma\sigma}} |0\rangle$ with $n^{\mathcal{F}}_{i\gamma\sigma} = \langle\mathcal{F}_{\mathrm{i}}|n_{i\gamma\sigma}|\mathcal{F}_{\mathrm{i}}\rangle$ which identifies whether there is an electron with spin σ occupied in orbital γ. By using a variational wave function of the Gutzwiller form,

$$|\Psi_G\rangle = \frac{\hat{G}|\Psi_0\rangle}{\sqrt{\langle\Psi_0|\hat{G}^2|\Psi_0\rangle}}$$

(A.3)

the expectation value of the electron Hamiltonian $\mathcal{H}$ for the γ-phase Ce (the site indices are dropped since there is only one atom in the primitive unit cell.) can be expressed as [Bunemann *et al.*, 1998, 2007; Yao *et al.*, 2011]:

$$\langle \mathcal{H} \rangle_G = \sum_{\alpha,\beta,\sigma} \left(z_{\alpha\sigma} z_{\beta\sigma} \tilde{t}_{\alpha\beta} + \tilde{\varepsilon}_\alpha \delta_{\alpha\beta} \right) \langle h^\dagger_{k\alpha\sigma} h_{k\beta\sigma} \rangle_0 - \sum_{\gamma,\sigma} \tilde{\varepsilon}_\gamma n^0_{\gamma\sigma} + \sum_{\mathcal{F}} E_{\mathcal{F}} p_{\mathcal{F}} \tag{A.4}$$

with,

$$z = \frac{1}{\sqrt{n^0_{\gamma\sigma}(1 - n^0_{\gamma\sigma})}} \sum_{\mathcal{F},\mathcal{F}'} \sqrt{p_{\mathcal{F}} p_{\mathcal{F}'}} \left| \langle \mathcal{F} | h^\dagger_{\gamma\sigma} | \mathcal{F}' \rangle \right|^2 \tag{A.5}$$

$$E_{\mathcal{F}} = \left\langle \mathcal{F} \left| \sum_{\gamma\sigma} \tilde{\varepsilon}_\gamma h^\dagger_{\gamma\sigma} h_{\gamma\sigma} + \frac{1}{2} \sum_{(\gamma\sigma) \neq (\gamma'\sigma)} \tilde{U}_{\gamma\gamma'} h^\dagger_{\gamma\sigma} h_{\gamma\sigma} h^\dagger_{\gamma'\sigma'} h_{\gamma'\sigma'} \right| \mathcal{F} \right\rangle \tag{A.6}$$

Here $p_{\mathcal{F}}$ is the occupation probability of configuration $|\mathcal{F}\rangle$, which satisfies the following constraints:

$$\sum_{\mathcal{F}} p_{\mathcal{F}} = 1 \tag{A.7}$$

$$\sum_{\mathcal{F}} p_{\mathcal{F}} n^{\mathcal{F}}_{\alpha\sigma} = n^0_{\alpha\sigma} \tag{A.8}$$

Next we take a different notation to express the occupation probability $p_{\mathcal{F}}$ in the matrix form:

$$\boldsymbol{P} = \boldsymbol{\varphi}^\dagger \boldsymbol{\varphi} = \sum_{i,j} c_i^* \varphi_i^{B*} c_j \varphi_j^B , with \; \boldsymbol{\varphi} = \sum_i c_i \varphi_i^B \tag{A.9}$$

The superscript B denotes the basis matrices, which satisfy $Tr[\varphi_i^B \varphi_j^B] = \delta_{ij}$. Thereafter, degeneracy can be introduced to the system by controlling the number of the basis φ_i^B and the computational load can be reduced by decreasing the number of variational parameters $\{c_i\}$.

Under the new notation, the constraints (Eq. A.7 and Eq. A.8) become

$$\sum_i c_i^* c_i = 1 \tag{A.10}$$

$$\sum_{i,j} c_i^* c_j T_{\alpha\sigma}^{ij} = n_{\alpha\sigma}^0 \tag{A.11}$$

with $T_{\alpha\sigma}^{ij} \equiv Tr[\boldsymbol{\varphi}_i^{B*} \boldsymbol{\varphi}_j^B \boldsymbol{n}_{\alpha\sigma}]$. Meanwhile, we get

$$z = \frac{1}{\sqrt{n_{\gamma\sigma}^0(1 - n_{\gamma\sigma}^0)}} \sum_{i,j} c_i^* c_j \cdot Th_{\gamma\sigma}^{ij} \tag{A.12}$$

with $Th_{\gamma\sigma}^{ij} \equiv Tr[\boldsymbol{\varphi}_i^{B*} \boldsymbol{h}_{\gamma\sigma}^\dagger \boldsymbol{\varphi}_j^B \boldsymbol{h}_{\gamma\sigma}]$ and

$$\sum_{\mathcal{F}} E_{\mathcal{F}} p_{\mathcal{F}} = \sum_{i,j} c_i^* c_j T E^{ij} \tag{A.13}$$

with $TE^{ij} \equiv Tr[\boldsymbol{E} \cdot \boldsymbol{\varphi}_i^{B*} \boldsymbol{\varphi}_j^B]$.

By following the same treatment in LDA + U calculations and choosing the double-counting (DC) term to be Eq. A. 14, the total energy per unit cell of the system can be expressed as $E_T = \langle \mathcal{H} \rangle_G - E_{DC}$.

$$E_{DC} = \frac{1}{2} U_{ff} N_f (N_f - 1) + U_{fd} N_f N_d \tag{A.14}$$

Minimization of the total energy with respect to the band wave function and the local configuration occupation probability under the set of constraints given by Eq. A.10 and A.11 yields the following equations to be solved self-consistently,

$$\mathcal{H}_{eff}^{k\sigma} |\psi_{nk\sigma}\rangle = \epsilon_{nk\sigma} |\psi_{nk\sigma}\rangle \tag{A.15}$$

$$\sum_j \mathcal{M}_{ij} c_j = \mu_0 c_i \tag{A.16}$$

where

$$\mathcal{H}_{eff}^{k\sigma} = \sum_{\alpha,\beta,\sigma} \left(z_{\alpha\sigma} z_{\beta\sigma} \tilde{t}_{\alpha\beta}^k + \tilde{\varepsilon}_\alpha \delta_{\alpha\beta} \right) h_{k\alpha\sigma}^\dagger h_{k\beta\sigma} + \sum_{\gamma,\sigma} \eta_{\gamma\sigma} h_{k\gamma\sigma}^\dagger h_{k\gamma\sigma} \tag{A.17}$$

$$\mathcal{M}_{ij} = \sum_{\gamma,\sigma} \frac{e_{\gamma\sigma}}{\sqrt{n_{\gamma\sigma}^0(1-n_{\gamma\sigma}^0)}} Th_{\gamma\sigma}^{ij} + TE^{ij} - \sum_{\alpha\sigma} \mu_{\alpha\sigma} T_{\alpha\sigma}^{ij} \qquad \text{(A.18)}$$

with

$$\eta_{\gamma\sigma} = -\varepsilon_\gamma + \frac{\partial z_{\gamma\sigma}}{\partial n_{\gamma\sigma}^0} e_{\gamma\sigma} + \mu_{\gamma\sigma}$$

$$- \left(\left[U_{ff}\left(N_f - \frac{1}{2}\right) + U_{fd}N_d \right] I_{[\gamma\in\{4f\}]} - U_{fd}N_f I_{[\gamma\in\{5d\}]} \right) \qquad \text{(A.19)}$$

and

$$e_{\gamma\sigma} = \sum_{k,\beta} \left(z_{\beta\sigma} \tilde{t}_{\gamma\beta}^k \langle h_{k\gamma\sigma}^\dagger h_{k\beta\sigma} \rangle_0 + c.c. \right) \qquad \text{(A.20)}$$

μ_0 and $\mu_{\alpha\sigma}$ are the Lagrange multipliers associated with the constraints (Eq. A.10 and A.11).

Both Eq. A.15 and A.16 can be viewed as eigenvalue problems. The dimension of Eq. A.15 is usually rather small in the tight-binding representation, while it can be very large for Eq. A.16. Additional complexity for Eq. A.16 is that it has to be solved with the constraints. To more efficiently solve Eq. A.16, we convert the eigenvalue problem into a direct minimization problem. One can rewrite Eq. A.16 as

$$\sum_j \bar{\mathcal{M}}_{ij} c_j - \left(\mu_0 + \sum_{\alpha\sigma} \mu_{\alpha\sigma} T_{\alpha\sigma}^{ij} \right) c_i = 0 \qquad \text{(A.21)}$$

with

$$\bar{\mathcal{M}}_{ij} = \sum_{\gamma,\sigma} \frac{e_{\gamma\sigma}}{\sqrt{n_{\gamma\sigma}^0(1-n_{\gamma\sigma}^0)}} Th_{\gamma\sigma}^{ij} + TE^{ij} \qquad \text{(A.22)}$$

The left hand side of Eq. A.21 is actually the force acting on the array $\{c_i\}$, thus force-based minimization scheme, such as steepest-decent approach, can be applied to solve it.

We start from some initial $\{c_i^{(0)}\}$, and update the $(n+1)^{\text{th}}$ iteration by

$$c_i^{(n+1)} = c_i^{(n)} + \alpha \left(\sum_j \bar{M}_{ij} c_j^{(n)} - \left(\mu_0^{(n)} c_i^{(n)} + \sum_{\alpha\sigma} \mu_{\alpha\sigma}^{(n)} \sum_j T_{\alpha\sigma}^{ij} c_j^{(n)} \right) \right) \qquad (A.23)$$

where α is a chosen scale factor. We find $\alpha = 0.01$ is generally well-behaved. $\left\{ \mu_0^{(n)}, \mu_{\alpha\sigma}^{(n)} \right\}$ are

determined by requiring the $\left\{ c_i^{(n+1)} \right\}$ to satisfy the constraints Eq. A.10 and A.11, which are a set

of linear equations by neglecting the high order terms of α:

$$\mu_0^{(n)} \cdot 2\alpha \sum_i \left(c_i^{(n)} \right)^2 + 2\alpha \sum_{\alpha\sigma} \mu_{\alpha\sigma}^{(n)} \sum_{ij} c_i^{(n)} c_j^{(n)} T_{\alpha\sigma}^{ij}$$

$$= \sum_i \left[\left(c_i^{(n)} \right)^2 + 2\alpha c_i^{(n)} \sum_j \bar{M}_{ij} c_j^{(n)} \right] - 1 \qquad (A.24)$$

$$\mu_0^{(n)} \cdot 2\alpha \sum_i \left(c_i^{(n)} \right)^2 T_{\alpha\sigma}^{ii} + 2\alpha \sum_{\alpha'\sigma'} \mu_{\alpha'\sigma'}^{(n)} \sum_i \left(c_i^{(n)} \right)^2 T_{\alpha'\sigma'}^{ii} \cdot T_{\alpha\sigma}^{ii}$$

$$= \sum_i \left[\left(c_i^{(n)} \right)^2 + 2\alpha c_i^{(n)} \sum_k \bar{M}_{ik} c_k^{(n)} \right] \cdot T_{\alpha\sigma}^{ii} - n_{\alpha\sigma}^0 \qquad (A.25)$$

BIBLIOGRAPHY

Anisimov, V. I. and Gunnarsson, O. (1991). Density-functional calculation of effective Coulomb interactions in metals. *Phys. Rev. B*, **43**, 7570–7574; Anisimov, V. I., Zaanen, J., and Anderson O. K. (1991). Band theory and Mott insulators: Hubbard U instead of Stoner I. *Phys. Rev. B*, **43**, 943–954; Anisimov, V. I., Solovyev, I. V., and Korotin, M. A. (1993). Density-functional theory and NiO photoemission spectra. *Phys. Rev. B*, **48**, 16929–16934.

Antropov, V., Ke, L., and Aberg, D. (2014). Constituents of magnetic anisotropy and a screening of spin–orbit coupling in solids. *Solid State Commun.*, **194**, 35-38.

Armstrong, A. R., Lyness, C., Menetrier, M., and Bruce, P. G. (2010). Structural Polymorphism in Li_2CoSiO_4 Intercalation Electrodes: A Combined Diffraction and NMR Study. *Chem. Mater.*, **22**, 1892-1900.

Armstrong, A. R., Kuganathan, N., Islam, M. S., and Bruce, P. G. (2011). Structure and Lithium Transport Pathways in Li_2FeSiO_4 Cathodes for Lithium Batteries. *J. Am. Chem. Soc.*, **133**, 13031-13035.

Ashcroft, N. W. and Mermin, N. D. (1976). *Solid State Physics*. Saunders College, Philadelphia.

Balasubramanian, B., Das, B., Skomski, R., Zhang, W. Y., and Sellmyer, D. J. (2013). Novel Nanostructured Rare-Earth-Free Magnetic Materials with High Energy Products. *Adv. Mater.*, **25**, 6090.

Balasubramanian, B., Das, B., Zhang, W. Y., Skomski, R., and Sellmyer, D. J. (2014). Hf–Co and Zr–Co alloys for rare-earth-free permanent magnets. *J. Phys.: Condens. Matter*, **26**, 264204.

Banerjea, A. and Smith, J. R. (1998). Origins of the Universal Binding Energy Relation. *Phys. Rev. B*, **37**, 6632.

Benedek, N., Chua, A., Elsasser, C., Sutton, A., and Finnis, M. (2008). Interatomic Potentials for Strontium Titanate: an Assessment of Their Transferability and Comparison with Density Functional Theory. *Phys. Rev. B*, **78**, 064110.

Blochl, P. E. (1994). Projector augmented-wave method. *Phys. Rev. B*, **50**, 17953.

Brommer, P. and Gahler, F. (2006). Effective potentials for quasicrystals from *ab initio* data. *Phil. Mag.*, **86**, 753; Brommer, P. and Gahler, F. (2007). Potfit: effective potentials from *ab initio* data modelling. *Simul. Mater. Sci. Eng.*, **15**, 295.

Bruce, P. G. and West, A. R. (1980). Phase diagram of the LISICON, solid electrolyte system, Li_4GeO_4-Zn_2GeO_4. *Mater. Res. Bull.*, **15**, 379.

Bunemann, J., Weber, W., and Gebhard, F. (1998). Multiband Gutzwiller wave functions for general on-site interactions. *Phys. Rev. B*, **57**, 6896.

Bunemann, J. and Gebhard, F. (2007). Equivalence of Gutzwiller and slave-boson mean-field theories for multiband Hubbard models. *Phys. Rev. B*, **76**, 193104.

Černý, M., Pokluda, J., Šob, M., Friák, M., and Šandera, P. (2003). *Ab initio* calculations of elastic and magnetic properties of Fe, Co, Ni, and Cr crystals under isotropic deformation. *Phys. Rev. B*, **67**, 035116.

Chang, H. W., Tsai, C. F., Hsieh, C. C., Shih, C. W., Chang, W. C., and Shaw, C. C. (2013). Magnetic properties enhancement of melt spun CoZrB ribbons by elemental substitutions *J. Magn. Magn. Mater.*, **346**, 74–77.

Chelikowsky, J. R. and Louie, S. G. (1996). *Quantum Theory of Real Materials*. Kluwer Press.

Chen, C. Y., Matsumoto, K., Nohira, T., and Hagiwara, R. (2014). Na_2MnSiO_4 as a positive electrode material for sodium secondary batteries using an ionic liquid electrolyte. *Electrochem. Commun.*, **45**, 63-66.

Chen, L. Y., Chang, H. W., Chiu, C. H., Chang, C. W., and Chang, W. C. (2005). Magnetic properties, phase evolution, and coercivity mechanism of $Co_xZr_{98-x}B_2$ (x=74−86) nanocomposites. *J. Appl. Phys.*, **97**, 10F307.

Chua, A., Benedek, N., Nicole, A., Chen, L., Finnis, M., and Sutton, A. (2010). A Genetic Algorithm for Predicting the Structures of Interfaces in Multicomponent Systems. *Nature Mater.*, **9**, 418−422.

Chung, H. Y., Weinberger, M. B., Levine, J. B., Kavner, A., Yang, J. M., Tolbert, S. H., and Kaner, R. B. (2007). Synthesis of Ultra-Incompressible Superhard Rhenium Diboride at Ambient Pressure. *Science*, **316**, 436.

Critical Materials Strategy, 379, U.S. DOE. (2011).

http://energy.gov/sites/prod/files/DOE_CMS2011_FINAL_Full.pdf

Cromer, D. T. and Herrington, K. (1955). The structures of anatase and rutile. *J. Am. Chem. Soc.*, **77**, 4708.

Curtarolo, S., Hart, G. L. W., Nardelli, M. B., Mingo, N., Sanvito, S., and Levy, O. (2013). The high-throughput highway to computational materials design. *Nature Mater.*, **12**, 191.

Daw, M. S. and Baskes, M. I. (1984). Embedded-atom method: Derivation and application to impurities, surfaces, and other defects in metals. *Phys. Rev. B*, **29**, 6443.

Deaven, D. M. and Ho, K. M. (1995). Molecular geometry optimization with a genetic algorithm. *Phys. Rev. Lett.*, **75**, 288.

Deem, M. W. and Newsam, J. M. (1989). Determination of 4-connected framework crystal-structures by simulated annealing. *Nature*, **342**, 260-262; Deem, M. W. and Newsam, J. M. (1992). Framework crystal-structure solution by simulated annealing: test application to known zeolite structures. *J. Am. Chem. Soc.*, **114**, 7189-7198.

Demczyk, B. G. and Cheng, S. F. (1991). Structures of Zr_2Co_{11} and $HfCo_7$ intermetallic compounds. *J. Appl. Cryst.*, **24**, 1023-1026.

Deng, X. Y., Wang, L., Dai, X., and Fang, Z. (2009). Local density approximation combined with Gutzwiller method for correlated electron systems: Formalism and applications. *Phys. Rev. B*, **79**, 075114.

Dillon, S. J., Tang, M., Carter, W. C., and Harmer, M. P. (2007). Complexion: A New Concept for Kinetic Engineering in Materials Science. *Acta Mater.*, **55**, 6208-6218.

Doll, K., Schon, J. C., and Jansen, M. (2007). Global exploration of the energy landscape of solids on the *ab initio* level. *Phys. Chem. Chem. Phys.*, **9**, 6128-6133.

Dominko, R., Bele, M., Gaberscek, M., Meden, A., Remskar, M., and Jamnik, J. (2006). Structure and electrochemical performance of Li_2MnSiO_4 and Li_2FeSiO_4 as potential Li-battery cathode materials. *Electrochem. Commun.*, **8**, 217-222.

Dubrovinskaia, N., Dubrovinsky, L., and Solozhenko, V. L. (2007). Comment on "Synthesis of Ultra-Incompressible Superhard Rhenium Diboride at Ambient Pressure". *Science*, **318**, 1550c.

Dudarev, S. L., Botton, G. A., Savrasov, S. Y., Humphreys, C. J., and Sutton, A. P. (1998). Electron-energy-loss spectra and the structural stability of nickel oxide: An LSDA+U study. *Phys. Rev. B*, **57**, 1505.

Dudeck, K. J. and Cockayne, D. J. H. (2010). Quantitative High Resolution Electron Microscopy Image Matching Applied to the Strontium Titanate $\Sigma3(112)$ Grain Boundary. *J. Phys.: Conf. Ser.*, **241**, 012033; Dudeck, K. J., Benedek, N. A., Finnis, M. W., and Cockayne, D. J. H. (2010). Atomic-scale Characterization of the SrTiO3 $\Sigma3$ (112) [$\bar{1}$ 10] Grain Boundary. *Phys. Rev. B*, **81**, 134109.

Duncan, H., Kondamreddy, A., Mercier, P. H. J., Page, Y. L., Abu-Lebdeh, Y., Couillard, M., Whitfield, P. S., and Davidson, I. J. (2011). Novel Pn Polymorph for Li_2MnSiO_4 and Its Electrochemical Activity As a Cathode Material in Li-Ion Batteries. *Chem. Mater.*, **23**, 5446-5456.

Eames, C., Armstrong, A. R., Bruce, P. G., and Islam, M. S. (2012). Insights into Changes in Voltage and Structure of Li_2FeSiO_4 Polymorphs for Lithium-Ion Batteries. *Chem. Mater.*, **24**, 2155-2161.

Ewald, P. P. (1962). *Fifty Years of X-ray Diffraction*. International Union of Crystallography, Utrecht, Chapter 2.

Feng, B., Hojo, H., Mizoguchi, T., Ohta, H., Findlay, S. D., Sato, Y., Shibata, N., Yamamoto, T., and Ikuhara, Y. (2012). Atomic Structure of a $\Sigma3[110]/(111)$ Grain Boundary in CeO_2. *Appl. Phys. Lett.*, **100**, 073109.

Foster, M. D., Simperler, A., Bell, R. G., Friedrichs, O. D., Almeida Paz, F. A., and Klinowski, J. (2004). Chemically feasible hypothetical crystalline networks. *Nature Mater.*, **3**, 234-238.

Freidrichs, O. D., Dress, A. W. M., Huson, D. H., Klinowski, J., and Mackay, A. L. (1999). Systematic enumeration of crystalline networks. *Nature*, **400**, 644-647.

Gabay, A. M., Zhang, Y., and Hadjipanayis, G. C. (2001). Cobalt-rich magnetic phases in Zr–Co alloys. *J. Magn. Magn. Mater.*, **236**, 37-41.

Gajdos, M., Hummer, K., Kresse, G., Furthmüller, J., and Bechstedt, F. (2006). Linear optical properties in the projector-augmented wave methodology. *Phys. Rev. B*, **73**, 045112.

Gao, C., Wang, H., and Hadjipanayis, G. C. (1990). High coercivity in non-rare-earth containing alloys. *J. Appl. Phys.*, **67**, 4960.

Ghemawat, A. M., Foldeski, M., Dunlap, R. A., and O'Handley, R. C. (1989). New microcrystalline hard magnets in a Co-Zr-B alloy system. *IEEE Trans. Magn.*, **25**, 3312.

Giannozzi, P., et al. (2009). QUANTUM ESPRESSO: a modular and open-source software project for quantum simulations of materials. *J. Phys.: Condens. Matter*, **21**, 395502.

Goedecker, S. (2004). Minima hopping: an efficient search method for the global minimum of the potential energy surface of complex molecular systems. *J. Chem. Phys.*, **120**, 9911.

Gou, H. Y., Wang, Z. B., Zhang, J. W., Yan, S. T., and Gao, F. M. (2009). Structural Stability and Elastic and Electronic Properties of Rhenium Borides: First Principle Investigations. *Inorg. Chem.*, **48**, 581-587.

Gummow, R. J., Sharma, N., Peterson, V. K., and He, Y. (2012). Crystal chemistry of the Pmnb polymorph of Li_2MnSiO_4. *J. Solid State Chem.*, **188**, 32-37.

Hafner, J., Wolverton, C., and Ceder. G. (2006). Toward Computational Materials Design: The Impact of Density Functional Theory on Materials Research. *MRS Bull.*, **31**, 659.

Haines, J., Le´ger, J. M., and Bocquillon, G. (2001). Synthesis and design of superhard material. *Annu Rev. Mater. Res.*, **31**, 1.

Harris, K. D. M., Johnson, R. L., and Kariuki, B. M. (1998). The genetic algorithm: foundations and applications in structure solution from powder diffraction data. *Acta Crystallogr. A*, **54**, 632.

Hellberg, C. S., Andersen, K. E., Li, H., Ryan, P. J., and Woicik, J. C. (2012). Structure of SrTiO$_3$ Films on Si. *Phys. Rev. Lett.*, **108**, 166101.

Hilgenkamp, H. and Mannhart, J. (2002). Grain Boundaries in High-Tc Superconductors. *Rev. Mod. Phys.*, **74**, 485-549.

Hill, R. (1952). The Elastic Behaviour of a Crystalline Aggregate. *Proc. Phys. Soc. A*, **65**, 349.

Ho, K. M., Shvartsburg, A., Pan, B., Lu, Z. Y., Wang, C. Z., Wacker, J. G., Fye, J. L., and Jarrold, M. F. (1998). Structures of medium-sized silicon clusters. *Nature*, **392**, 582-585.

Ho, K. M., Schmalian, J., and Wang, C. Z. (2008). Gutzwiller density functional theory for correlated electron systems. *Phys. Rev. B*, **77**, 073101.

Hobbs, D., Kresse, G., and Hafner, J. (2000). Fully unconstrained noncollinear magnetism within the projector augmented-wave method. *Phys. Rev. B*, **62**, 11556.

Hofer, W. A., Foster, A. S., and Shluger, A. L. (2003). Theories of scanning probe microscopes at the atomic scale. *Rev. Mod. Phys.*, **75**, 1287.

Hohenberg, P. and Kohn, W. (1964). Inhomogeneous Electron Gas. *Phys. Rev. B*, **136**, 864.

Ishikawa, T. and Ohmori, K. (1990). Hard magnetic phase in rapidly quenched Zr-Co-B alloys. *IEEE Trans. Magn.*, **26**, 1370.

Ivanova, G. V., Shchegoleva, N. N., and Gabay, A. M. (2007). Crystal structure of Zr$_2$Co$_{11}$ hard magnetic compound. *J. Alloys Compd.*, **432**, 135-141.

Ivanova, G. V. and Shchegoleva, N. N. (2009). The Microstructure of a Magnetically Hard Zr_2Co_{11} Alloy. *Phys. Met. Metallogr.*, **107**, 270-275.

Jacob, K. T. and Rajitha, G. (2011). Thermodynamic Properties of Strontium Titanates: Sr_2TiO_4, $Sr_3Ti_2O_7$, $Sr_4Ti_3O_{10}$, and $SrTiO_3$. *J. Chem. Thermodyn.*, **43**, 51–57.

Jain, A., et al. (2013). The materials project: a materials genome approach to accelerating materials innovation. *APL Materials*, **1**, 011002.

Ji, M., Wang, C. Z., and Ho, K. M. (2010). Comparing efficiencies of genetic and minima hopping algorithms for crystal structure prediction. *Phys. Chem. Chem. Phys.*, **12**, 11617-11623.

Juarez-Arellanoa, E. A., Winklerb, B., Friedrichb, A., Bayarjargalb, L., Morgenrothb, W., Kunzc, M., and Milmand, V. (2013). In situ study of the formation of rhenium borides from the elements at high-(p, T) conditions: Extreme incompressibility of Re_7B_3 and formation of new phases. *Solid State Sci.*, **25**, 85-92.

Kawano, A., Mizuta, Y., Takagiwa, H., Muranaka, T., and Akimitsu, J. (2003). The Superconductivity in Re–B System. *J. Phys. Soc. Jpn.*, **72**, 1724.

Ke, L., Belashchenko, K. D., van Schilfgaarde, M., Kotani, T., and Antropov, V. P. (2013). Effects of alloying and strain on the magnetic properties of $Fe_{16}N_2$. *Phys. Rev. B*, **88**, 024404.

Kim, S., Seo, D., Ma, X., Ceder, G., and Kang, K. (2012). Electrode materials for rechargeable sodium-ion batteries: potential alternatives to current lithium-ion batteries. *Adv. Energy Mater.*, **2**, 710-721.

Kirkpatrick, S., Gelatt, C. D., and Vecchi, M. P. (1983). Optimization by simulated annealing. *Science*, **220**, 671.

Kittel, C. (2005). *Introduction to Solid State Physics*. John Wiley & Sons, 8th edition.

Knacke, O., Kubaschewski, O., and Hesselmann, K. (Eds.) (1991). Thermochemical Properties of Inorganic Substances, Springer-Verlag Publishing, Heidelberg and Verlag Stahleisen mbH, Dusseldorf.

Koelling, D. D. and Harmon, B. N. (1977). A technique for relativistic spin-polarised calculations. *J. Phys. C: Solid State Phys.*, **10**, 3107.

Kohn, W. and Sham, L. J. (1965). Self-Consistent Equations Including Exchange and Correlation Effects. *Phys. Rev.*, **140**, A1133.

Kojima, A., Kojima, T., Tabuchi, M., and Sakaib, T. (2012). Crystal Structure and Electrochemical Performance of a New Lithium Trivalent Iron Silicate. *J. Electrochem. Soc.*, **159**, A725-A729.

Kokalj, A., Dominko, R., Mali, G., Meden, A., Gaberseck, M., and Jamnik, J. (2007). Beyond One-Electron Reaction in Li Cathode Materials: Designing $Li_2Mn_xFe_{1-x}SiO_4$. *Chem. Mater.*, **19**, 3633-3640.

Kotliar, G. and Vollhardt, D. (2004). Strongly Correlated Materials: Insights From Dynamical Mean-Field Theory. *Physics Today*, **57**, 53.

Kotliar, G., Savrasov, S. Y., Haule, K., Oudovenko, V. S., Parcollet, O., and Marianetti, C. A. (2006). Electronic structure calculations with dynamical mean-field theory. *Rev. Mod. Phys.*, **78**, 865–951.

Kramer, M. J., McCallum, R. W., Anderson, I. A., and Constantinides, S. (2012). Prospects for Non-Rare Earth Permanent Magnets for Traction Motors and Generators. *JOM*, **64**, 752.

Kresse, G. and Furthmuller, J. (1996). Efficient iterative schemes for *ab initio* total-energy calculations using a plane-wave basis set. *Phys. Rev. B*, **54**, 11169–11181; Kresse, G. and Furthmuller, J. (1996). Efficiency of *ab initio* total energy calculations for metals and semiconductors using a plane-wave basis set. *Comput. Mater. Sci.*, **6**, 15-50.

Kresse, G. and Joubert, J. (1999). From ultrasoft pseudopotentials to the projector augmented-wave method. *Phys. Rev. B*, **59**, 1758–1775.

Kudrnovský, J., Drchal, V., Blaas, C., Weinberger, P., Turek, I., and Bruno P. (2000). *Ab initio* theory of perpendicular magnetotransport in metallic multilayers. *Phys. Rev. B*, **62**, 15084.

Lanata, N., Yao, Y. X., Wang, C. Z., Ho, K. M., Schmalian, J., Haule, K., and Kotliar, G. (2013). γ-α Isostructural Transition in Cerium. *Phys. Rev. Lett.*, **111**, 196801; Lanata, N., Yao, Y. X., Wang, C. Z., Ho, K. M., and Kotliar, G. (2015). Phase Diagram and Electronic Structure of Praseodymium and Plutonium. *Phys. Rev. X*, **5**, 011008.

Langford, J. I. and Wilson, A. J. C. (1978). Scherrer after sixty years: A survey and some new results in the determination of crystallite size. *J. Appl. Cryst.*, **11**, 102-113.

Lee, H., Park, S. D., Moon, J., Lee, H., Cho, K., Cho, M., and Kim, S. Y. (2014). Origin of Poor Cyclability in Li_2MnSiO_4 from First-Principles Calculations: Layer Exfoliation and Unstable Cycled Structure. *Chem. Mater.*, **26**, 3896-3899.

Lennard-Jones, J. E. (1924). On the determination of molecular fields. *Proc. Roy. Soc. A*, **106**, 441-477.

LePage, Y. and Saxe, P. (2001). Symmetry-general least-squares extraction of elastic coefficients from *ab initio* total energy calculations. *Phys. Rev. B*, **63**, 174103.

Li, X. Z. (2012). Software Design for Simulation and Analysis of Electron Diffraction Patterns. *Microsc. Microanal.*, **18** (Suppl 2), 1262-1263.

Li, Y. X., Gong, Z. L., and Yang, Y. (2007). Synthesis and characterization of Li_2MnSiO_4/C nanocomposite cathode material for lithium ion batteries. *J. Power Sources*, **174**, 528-532.

Luth, H. (2010). *Solid Surfaces, Interfaces and Thin Films.* Springer, Heidelberg. 5th edition, Chapter 1, pp 1-28.

Lv. D. P., Wen, W., Huang, X. K., Bai, J. Y., Mi, J. X., Wu, S. Q., and Yang, Y. (2011). A novel Li_2FeSiO_4/C composite: Synthesis, characterization and high storage capacity. *J. Mater. Chem.*, **21**, 9506.

Lyness, C., Delobel, B., Armstrong, A. R., and Bruce, P. G. (2007). The lithium intercalation compound Li_2CoSiO_4 and its behaviour as a positive electrode for lithium batteries. *Chem. Commun.*, 4890-4892.

Maddox, J. (1988). Crystals from First Principles. *Nature*, **335**, 201.

Martin, R. M. (2004). *Electronic Structure: Basic Theory and Practical Methods*. Cambridge University Press, Cambridge, Chapter 6.

McCallum, R. W., Lewis, L. H., Skomski, R., Kramer, M. J., and Anderson, I. E. (2014). Practical Aspects of Modern and Future Permanent Magnets. *Annu. Rev. Mater. Res.*, **44**, 10.1-10.27.

Meng, Y. S. and Dompablo, M. E. A. (2009). First-principles computational materials design for energy storage materials in lithium ion batteries. *Energy Environ. Sci.*, **2**, 589-609.

Metropolis, N. and Ulam, S. (1949). The Monte Carlo Method. *J. Amer. Stat. Assoc.*, **44**, 335.

Monkhorst, H. J. and Pack, J. D. (1976). Special points for Brillouin-zone integrations. *Phys. Rev. B*, **13**, 5188.

Muraliganth, T., Stroukoff, K. R., and Manthiram, A. (2010). Microwave-Solvothermal Synthesis of Nanostructured Li_2MSiO_4/C (M = Mn and Fe) Cathodes for Lithium-Ion Batteries. *Chem. Mater.*, **22**, 5754-5761.

Nagamatsu, J., Nakagawa, N., Muranaka, T., Zenitani, Y., and Akimitsu, J. (2001). Superconductivity at 39 K in magnesium diboride. *Nature*, **410**, 63.

Nguyen, M. C., Choi, J., Zhao, X., Wang, C. Z., Zhang, Z. Y., and Ho, K. M. (2013). New layered structures of cuprous chalcogenides as thin film solar cell materials: Cu_2Te and Cu_2Se. *Phys. Rev. Lett.*, **111**, 165502.

Nguyen, M. C., Zhao, X., Wang, C. Z., and Ho, K. M. (2014). sp3-hybridized Framework Structure of Group 14 Elements Discorved by Genetic Algorithm. *Phys. Rev. B*, **89**, 184112; Nguyen, M. C., Zhao, X., Wang, Y. G., Wang, C. Z., and Ho, K. M. (2014). Genetic Algorithm Prediction of Crystal Structure of Metastable Si-IX Phase. *Solid State Commun.*, **182**, 14-16.

Nguyen, M. C., Zhao, X., Wang, C. Z., and Ho, K. M. (2015). Cluster Expansion Modeling and Monte Carlo Simulation of Alnico 5-7 Permanent Magnets. *J. Appl. Phys.*, **117**, 093905.

Norskov, J. K., Bligaard, T., Rossmeisl, J., and Christensen, C. H. (2009). Towards the computational design of solid catalysts. *Nature Chem.*, **1**, 37.

NSF overview, available at the official webpage:

http://www.nsf.gov/news/overviews/chemistry/chem_q02.jsp.

Nytén, A., Abouimrane, A., Armand, M., Gustafsson, T., and Thomas, J. O. (2005). Electrochemical performance of Li_2FeSiO_4 as a new Li-battery cathode material. *Electrochem. Commun.*, **7**, 156-160.

Oganov, A. R. and Glass, C. W. (2008). Evolutionary crystal structure prediction as a tool in materials design. *J. Phys.: Condens. Matter*, **20**, 064210.

Oganov, A. R., Chen, J., Gatti, C., Ma, Y. M., Glass, C. W., Liu, Z., Yu, T., Kurakevych, O. O., and Solozhenko, V. L. (2009). Ionic high-pressure form of elemental boron. *Nature*, **457**, 863-867.

Oganov, A. R. (2011). Modern Methods of Crystal structure Prediction. Wiley-VCH, Weinheim.

Olson, G. B. (2000). Designing a New Material World. *Science*, **288**, 933.

Page, Y. L. and Saxe, P. (2002). Symmetry-general least-squares extraction of elastic data for strained materials from *ab initio* calculations of stress. *Phys. Rev. B*, **65**, 104104.

Peacock, P. W., Xiong, K., Tse, K., and Robertson, J. (2006). Bonding and Interface States of $Si:HfO_2$ and $Si:ZrO_2$ Interfaces. *Phys. Rev. B*, **73**, 075328.

Perdew, J. P. and Zunger, A. (1981). Self-interaction Correction to Density-functional Approximations for Many-electron Systems. *Phys. Rev. B*, **23**, 5048-5079.

Perdew, J. P., Burke, K., and Ernzerhof, M. (1996). Generalized Gradient Approximation Made Simple. *Phys. Rev. Lett.*, **77**, 3865–3868.

Pickard, C. J. and Needs, R. J. (2011). *Ab initio* random structure searching. *J. Phys.: Condens. Matter*, **23**, 053201.

Plimpton, S. (1995). Fast Parallel Algorithms for Short-Range Molecular Dynamics. *J. Comput. Phys.*, **117**, 1; code available at http://lammps.sandia.gov.

Politaev, V. V., Petrenko, A. A., Nalbandyn, V. B., Medvedev, B. S., and Shvetsova, E. S. (2007). Crystal structure, phase relations and electrochemical properties of monoclinic Li_2MnSiO_4. *J. Solid State Chem.*, **180**, 1045.

Poudyal, N. and Liu, J. P. (2013). Advances in nanostructured permanent magnets research. *J. Phys. D: Appl. Phys.*, **46**, 043001.

Prodan, E. (2010). Viewpoint: Raising the temperature on density-functional theory. *Physics*, **3**, 99.

Pugh, S. F. (1954). XCII. Relations between the elastic moduli and the plastic properties of polycrystalline pure metals. *Philos. Mag.*, **45**, 823.

Qin, J., He, D., Wang, J., Fang, L., Lei, L., and Li, Y. (2008). Is Rhenium Diboride a Superhard Material? *Adv Mater.*, **20**, 4780.

Robertson, J. (2006). High Dielectric Constant Gate Oxides for Metal Oxide Si Transistors. *Rep. Prog. Phys.*, **69**, 327–396.

Saito, T. (2003a). The Origin of the Coercivity in Co–Zr System Alloys. *IEEE Trans. Magn.*, **39**, 2890.

Saito, T. (2003b). High performance Co–Zr–B melt-spun ribbons. *Appl. Phys. Lett.*, **82**, 2306.

Saito, T. and Itakura, M. (2013). Microstructures of Co–Zr–B alloys produced by melt-spinning technique. *J. Alloys Compd.*, **572**, 124.

Saracibar, A., Van der Ven, A., and Arroyo-de Dompablo, M. E. (2012). Crystal Structure, Energetics, And Electrochemistry of Li_2FeSiO_4 Polymorphs from First Principles Calculations. *Chem. Mater.*, **24**, 495-503.

Sato, K. and Katayamo-Yoshida, H. (2002). First principles materials design for semiconductor spintronics. *Semicond. Sci. Technol.*, **17**, 367-376.

Savrasov, S. Y., Kotliar, G., and Abrahams, E. (2001). Correlated electrons in δ-plutonium within a dynamical mean-field picture. *Nature*, **410**, 793.

Schobel, J. D. and Stadelmaier, H. H. (1969). Cobalt-rich phases in the cobalt-hafnium-boron and cobalt-zirconium-boron ternary systems. *Metall*, **23**, 25.

Sheng, H. W., Luo, W. K., Alamgir, F. M., Bai, J. M., and Ma, E. (2006). Atomic packing and short-to-medium-range order in metallic glasses. *Nature*, **439**, 419.

Sirisopanaporn, C., Masquelier, C., Bruce, P. G., Armstrong, A. R., and Dominko, R. (2011). Dependence of Li_2FeSiO_4 Electrochemistry on Structure. *J. Am. Chem. Soc.*, **133**, 1263-1265.

Srinivasan, S. and Baskes, M. I. (2004). On the Lennard-Jones EAM potential. *Proc. R. Soc. Lond. A*, **460**, 1649.

Stokbro, K., Taylor, J., Brandbyge, M., and Ordejón, P. (2003). TranSIESTA: A Spice for Molecular Electronics. *Ann. N.Y. Acad. Sci.*, **1006**, 212.

Stroink, G., Stadnik, Z. M., Viau, G., and Dunlap, R. A. (1990). The influence of quenching rate on the magnetic properties of microcrystalline alloys $Co_{80}Zr_{20-x}B_x$. *J. Appl. Phys.*, **67**, 4463.

Strukova, G. K., Degtyareva, V. F., Shovkun, D. V., Zverev, V. N., Kiiko, V. M., Ionov, A. M., and Chaika, A. N. (2001). Superconductivity in the Re-B system. arXiv:cond-mat/0105293.

Telegus, V. S., Kuz'ma, Y. B., and Stefanishina, T. K. (1969). The ternary chromium - Rhenium - Boron system. *Sov. Powder Metall. Met. Ceram.*, **8**, 133.

Tersoff, J. (1998). New empirical approach for the structure and energy of covalent systems. *Phys. Rev. B*, **37**, 6991.

Tilley, R. J. D. (2006). *Crystals and Crystal Structures*. John Wiley & Sons, 1st edition.

Togo, A., Oba, F., and Tanaka, I. (2008). First-principles calculations of the ferroelastic transition between rutile-type and CaCl2-type SiO2 at high pressures. *Phys. Rev. B*, **78**, 134106.

Treacy, M. M. J, Rivin, I., Balkovsky, E., Randall, K. H., and Foster, M. D. (2004). Enumeration of periodic tetrahedral frameworks II. Polynodal graphs. *Micropor. Mesopor. Mater.*, **74**, 121-132.

Vanderbilt, D. (2004). First-Principles Theory of Polarization and Electric Fields in Ferroelectrics. *Ferroelectrics*, 301, pp 9.

van Alfthan, S., Haynes, P. D., Kaski, K., and Sutton, A. P. (2006). Are the Structures of Twist Grain Boundaries in Silicon Ordered at 0K? *Phys. Rev. Lett.*, **96**, 055505.

van de Walle, A., Asta, M., and Ceder, G. (2002a). The alloy theoretic automated toolkit: A user guide. *Calphad*, **26**, 539.

van de Walle, A. and Ceder, G. (2002b). The effect of lattice vibrations on substitutional alloy thermodynamics. *Rev. Mod. Phys.*, **74**, 11.

van de Walle, A. (2009). Multicomponent multisublattice alloys, nonconfigurational entropy and other additions to the Alloy Theoretic Automated Toolkit. *Calphad*, **33**, 266.

Wang, B., Wang, D. Y., and Wang, Y. X. (2013). A new hard phase of ReB4 predicted from first principles. *J. Alloys Compd.*, **573**, 20.

Wang, G. T., Qian, Y. M., Xu, G., Dai, X., and Fang, Z. (2010). Gutzwiller Density Functional Studies of FeAs-Based Superconductors: Structure Optimization and Evidence for a Three-Dimensional Fermi Surface. *Phys. Rev. Lett.*, **104**, 047002.

Wang, Y., Lv, J., Zhu, L., and Ma, Y. (2010). Crystal structure prediction via particle-swarm optimization. *Phys. Rev. B*, **82**, 094116.

West, A. R. and Glasser, F. P. (1972). Preparation and crystal chemistry of some tetrahedral Li$_3$PO$_4$-type compounds. *J. Solid State Chem.*, **4**, 20.

Will, G. and Kiefer, B. Z. (2001). Electron Deformation Density in Rhombohedral α-Boron. *Anorg. Allg. Chem.,* **627**, 2100.

Woodley, S. M., Battle, P. D., Gale, J. D., and Catlow, C. R. A. (1999). The prediction of inorganic crystal structures using a genetic algorithm and energy minimization. *Phys. Chem. Chem. Phys.*, **1**, 2535.

Woodley, S. M. and Catlow, R. (2008). Crystal structure prediction from first principles. *Nature Mater.*, **7**, 937.

Wu, S. Q., Zhang, J. H., Zhu, Z. Z., and Yang, Y. (2007). Structural and electronic properties of the Li-ion battery cathode material Li$_x$CoSiO$_4$. *Curr. Appl. Phys.*, **7**, 611-616.

Wu, S. Q., Zhu, Z. Z., Yang, Y., and Hou, Z. F. (2009). Structural stabilities, electronic structures and lithium deintercalation in Li$_x$MSiO$_4$(M = Mn, Fe, Co, Ni): A GGA and GGA +U study. *Comput. Mater. Sci.*, **44**, 1243-1251.

Wu, S. Q., Ji, M., Wang, C. Z., Nguyen, M. C., Zhao, X., Umenoto, K., Wentzcovitch, R. M., and Ho, K. M. (2014). An adaptive genetic algorithm for crystal structure prediction. *J. Phys.: Condens. Matter*, **26**, 035402.

Wu, X., Vanderbilt, D., and Hamann, D. R. (2005). Systematic treatment of displacements, strains, and electric fields in density-functional perturbation theory. *Phys. Rev. B*, **72**, 035105.

Wu, Z. J., Zhao, E. J., Xiang, H. P., Hao, X. F., Liu, X. J., and Meng, J. (2007). Crystal structures and elastic properties of superhard IrN2 and IrN3 from first principles. *Phys. Rev. B*, **76**, 054115.

Xiang, H. J., Silva, J. L. F., Branz, H. M., and Wei, S. H. (2009). Understanding the Clean Interface between Covalent Si and Ionic Al_2O_3. *Phys. Rev. Lett.*, **103**, 116101.

Xing, Q., Miller, M. K., Zhou, L., Dillon, H. M., McCallum, R. W., Anderson, I. E., Constantinides, S., and Kramer, M. J. (2013). Phase and Elemental Distributions in Alnico Magnetic Materials. *IEEE Trans. Magn.*, **49**, 3314.

Yao, Y. X., Wang, C. Z., and Ho, K. M. (2011). Including many-body screening into self-consistent calculations: Tight-binding model studies with the Gutzwiller approximation. *Phys. Rev. B*, **83**, 245139.

Yao, Y. X., Liu, J., Wang, C. Z., and Ho, K. M. (2014). Correlation matrix renormalization approximation for total-energy calculations of correlated electron systems. *Phys. Rev. B*, **89**, 045131.

Yuan, Z. Z., Chen, J. M., Lu, Y., and Chen, X. D. (2008). Preparation and magnetic properties of amorphous Co–Zr–B alloy nano-powders. *J. Alloys Compd.*, **450**, 245.

Zang, C. P., Sun, H., Tse, J. S., and Chen, C. F. (2012). Indentation strength of ultraincompressible rhenium boride, carbide, and nitride from first-principles calculations. *Phys. Rev. B*, **86**, 014108.

Zhang, J., Wang, C. Z., and Ho, K. M. (2009) Finding the Low-Energy Structures of Si[001] Symmetric Tilted Grain Boundaries with a Genetic Algorithm. *Phys. Rev. B*, **80**, 174102.

Zhang, M. Y., Zhang, J. B., Wu, C. J., Wang, W. Q., and Su, F. (2010). Hard magnetic properties in melt-spun $Co_{80}Zr_{18-x}Mo_xB_2$ alloys. *Physica B*, **405**, 1725.

Zhang, P., Hu, C. H., Wu, S. Q., Zhu, Z. Z., and Yang, Y. (2012). Structural properties and energetics of Li_2FeSiO_4 polymorphs and their delithiated products from first-principles. *Phys. Chem. Chem. Phys.*, **14**, 7346-7351.

Zhang, W. Y., Li, X. Z., Valloppilly, S., Skomski, R., Shield, J. E., and Sellmyer, D. J. (2013). Magnetism of rapidly quenched rhombohedral Zr_2Co_{11}-based nanocomposites. *J. Phys. D: Appl. Phys.*, **46**, 135004.

Zhang, W. Y., Li, X. Z., Valloppilly, S. R., Skomski, R., and Sellmyer, D. J. (2014). Effect of annealing on nanostructure and magnetic properties of Zr_2Co_{11} material. *Mater. Sci. Eng. B*, **186**, 64-67.

Zhang, Z. L., Sigle, W., Phillipp, F., and Ruhle, M. (2003). Direct Atom-Resolved Imaging of Oxides and Their Grain Boundaries. *Science*, **302**, 846-849.

Zhao, E. J., Wang, J. P., Meng, J., and Wu, Z. J. (2010). Phase stability and mechanical properties of rhenium borides by first-principles calculations. *J. Comput. Chem.*, **31**, 1904.

Zhao, X., Nguyen, M. C., Wang, C. Z., and Ho, K. M. (2013). Structures and stability of alkaline earth metal peroxides XO_2 (X = Ca, Be, Mg) studied by a genetic algorithm. *RSC Adv.*, **3**, 22135.

Zhao, X., Nguyen, M. C., Zhang, W., Wang, C. Z., Kramer, M. J., Sellmyer, D. J., Li, X. Z., Zhang, F., Ke, L., Antropov, V. P., and Ho, K. M. (2014a). Exploring the Structural Complexity of Intermetallic Compounds by an Adaptive Genetic Algorithm. *Phys. Rev. Lett.*, **112**, 045502.

Zhao, X., Shu, Q., Nguyen, M. C., Wang, Y., Ji, M., Xiang, H., Ho, K. M., Gong, X. G., and Wang, C. Z. (2014b). Interface Structure Prediction from First-Principles. *J. Phys. Chem. C*, **118**, 9524.

Zhao, X., Nguyen, M. C., Wang, C. Z., and Ho, K. M. (2014c). New stable Re-B phases for ultra-hard materials. *J. Phys.: Condens. Matter*, **26**, 455401.

Zhao, X., Ke, L. Q., Nguyen, M. C., Wang, C. Z., and Ho, K. M. (2015a). Structures and magnetic properties of Co-Zr-B magnets studied by first-principles calculations. arXiv:1504.05829.

Zhao, X., Wu, S. Q., Lv, X. B., Nguyen, M. C., Wang, C. Z., Lin, Z. J., Zhu, Z. Z., and Ho, K. M. (2015). Fast motif-network scheme for extensive exploration of complex crystal structures in silicate cathodes. arXiv:1504.02070.

Zhou, L., Miller, M. K., Lu, P., Ke, L., Skomski, R., Dillon, H., Xing, Q., Palasyuk, A., McCartney, M. R., Smith, D. J., Constantinides, S., McCallum, R. W., Anderson, I. E., Antropov, V., and Kramer, M. J. (2014). Architecture and magnetism of alnico. *Acta Mater.*, **74**, 224.

Zhou, X. W., Johnson, R. A., and Wadley, H. N. G. (2004). Misfit-energy-increasing dislocations in vapor-deposited CoFe/NiFe multilayers. *Phys. Rev. B*, **69**, 144113.

Zhu, J. H. (2006). Co-Zr Phase Diagram, ASM Alloy Phase Diagrams Center, Villars, P. editor-in-chief; Okamoto, H. & Cenzual, K. section editors, ASM International, Materials Park, OH.